공학박사 학위논문

Preparation of Spherical- and Bowl-Shaped Mesoporous TiO_2 Clusters as Light Scatterers and Their Application to Solar Cell and Photocatalysis

구형과 보울형 미세다공성 이산화티탄 광산란체의 제조 및 이들의 태양전지와 광촉매 응용

2017년 8월

서울대학교 대학원

재료공학부

김 현 중

Abstract

Preparation of Spherical- and Bowl-Shaped Mesoporous TiO_2 Clusters as Light Scatterers and Their Application to Solar Cell and Photocatalysis

Hyun-Joong Kim
Department of Materials Science and Engineering
The Graduate School
Seoul National University

Light can be scattered and redirected in many directions. Particularly, when the size of the particles is comparable to the wavelength of the incident light, the Mie's scattering happens. In the atmosphere, the clouds appear white, attributing to the Mie's scattering effect, which can scatter all wavelength of the visible light by the various sized dusts. If we introduce the Mie's scattering phenomenon into the TiO_2 spheres, when the light collides with the TiO_2 sphere with size comparable to its wavelength, the light scatters strongly along the forward direction. Therefore, the path length of the incident light between the neighbored spheres will be increased, leading to a promoted light utilization efficiency over the spheres.

With this background and the technological and scientific value of light scatterers as motivations, the preparation of TiO_2 clusters as light scattering centers with specific characteristics is both desirable and technologically important. In this study, spherical- and bowl- shaped mesoporous TiO_2 clusters as light scattering centers were developed using aqueous and nonaqueous sol-gel process, then applied to solar cell and photocatalysis.

Size-controlled spherical mesoporous TiO_2 clusters were successfully synthesized using titanium precursor (titanium (IV) isopropoxide) and various amphiphilic triblock copolymers as soft template. The triblock copolymer is used as structure-directing and pore-forming agent and the interaction between the titanium precursor and the triblock copolymer self-assemblies in solvent leads to the assembly of TiO_2 nanoparticles into spherical aggregates with wormhole-like porous structures. The triblock copolymer micelle was composed of a core dominated by PO and a corona dominated by EO segments. The core of the micelles was believed to be free of water, while the swollen corona was hydrated. The aggregation behavior of the triblock copolymer under thermodynamic conditions may affect the TiO_2 cluster size and morphology.

Based on size-controlled synthesis, we prepared the anatase TiO_2/zinc phthalocyanine (ZnPc) hybrids in various sizes (245 − 1188 nm) and examined the visible light photocatalytic activity of TiO_2/ZnPc hybrids, in conjunction with their Mie light scattering ability. ZnPc molecules are well-incorporated

and dispersed on the surface of the TiO_2, instead of being aggregates. We confirmed the formation of spherical TiO_2/ZnPc hybrids in various sizes (245, 548, 798, 1188 nm in diameter), the large specific surface areas (up to 223.76 m^2/g), and the mesoporous structures. The mesoporous TiO_2/ZnPc hybrids showed excellent photocatalytic efficiency (up to 89.93% after 90 min) toward the degradation of methylene blue under visible light irradiation, which is about 2 times of that of simple nanoparticular P25/ZnPc. Among the mesoporous TiO_2/ZnPc hybrids, the hybrid with a size of 548 nm (P123-TiO_2/ZnPc) exhibited the highest photocatalytic activity. The highest activity observed on P123-TiO_2/ZnPc may be attributed to its efficient cascade Mie scattering effect under visible light irradiation.

Photoelectrodes composed of mesoporous TiO_2 spheres as scattering centers and TiO_2 nanoparticles as the binder were fabricated and tested with the aim of improving the energy conversion efficiency of dye-sensitized solar cells (DSSCs). These electrodes composed of TiO_2 spheres and nanoparticles enable the fabrication of high performance DSSCs, because of the light scattering of the TiO_2 spheres and the dye-loading capacity of their high surface areas. The energy conversion efficiency of composite-type photoelectrode was found to be 7.66%, which is higher than that of nanocrystal electrode (4.50%).

We prepared the spherical and bowl-shaped clusters of titania (TiO_2) nanorods using an electrospray technique and examine the photovoltaic properties of the clusters, in conjunction with their light scattering ability. The nanorods with a

diameter of about 3 nm and the length of about 25 nm formed clusters with different morphology depending on the vapor pressure of the solvent. The clusters possessed high specific surface areas of up to 113.57 m^2/g and mesoporous structures. Dye-sensitized solar cells containing the clusters as a scattering layer displayed excellent photovoltaic performance. The cell with a scattering layer of the bowl-shaped TiO_2 nanorod cluster exhibited the highest energy conversion efficiency of the cells of 9.13%. Such high efficiency was attributed to the high dye loading capacity and multiple light scattering ability of the bowl-shaped TiO_2 nanorod cluster.

Keywords: Light scatterer, Titanium dioxide, Triblock copolymer, Sol-gel chemistry, Mesorporous, Electrospray, Sphere, Bowl, Dye-Sensitized Solar Cell, Photocatalysis, Visble light, Light Scattering Layer, Mie scattering,

Student Number: 2008-30177

Contents

List of Tables

List of Figures

Chapter 1

Introduction

1.1 Light scattering by small particles

Light scattering is a common phenomenon in optics regarding the propagation of light in the presence of object. Normally, when light encounters an object, according to the laws of reflection and refraction, the radiation may either propagate in the forward direction, giving rise to refraction and absorption, or propagate in the backward direction, causing reflection, as shown in Fig. 1.1(a). However, under certain condition when the dimensions of the object are on the order of the wavelength of light, the radiation will be spread in all directions that deviate from the trajectory of the reflected or refracted light as determined by the laws of reflection and refraction, as shown in Fig. 12.(b). Such an optical phenomenon is called light scattering, and the object that causes the light scattering is known as the scatterer or scattering center [1-3].

Many theories have been developed to describe the process of light scattering. Among them, Rayleigh scattering theory and Mie scattering theory are typically applicable for spherical scatterers such as particles, droplets, and density fluctuations. These two theories are categorized according to the comparability between the light wavelengths and the feature size of the scatterers. Specifically,

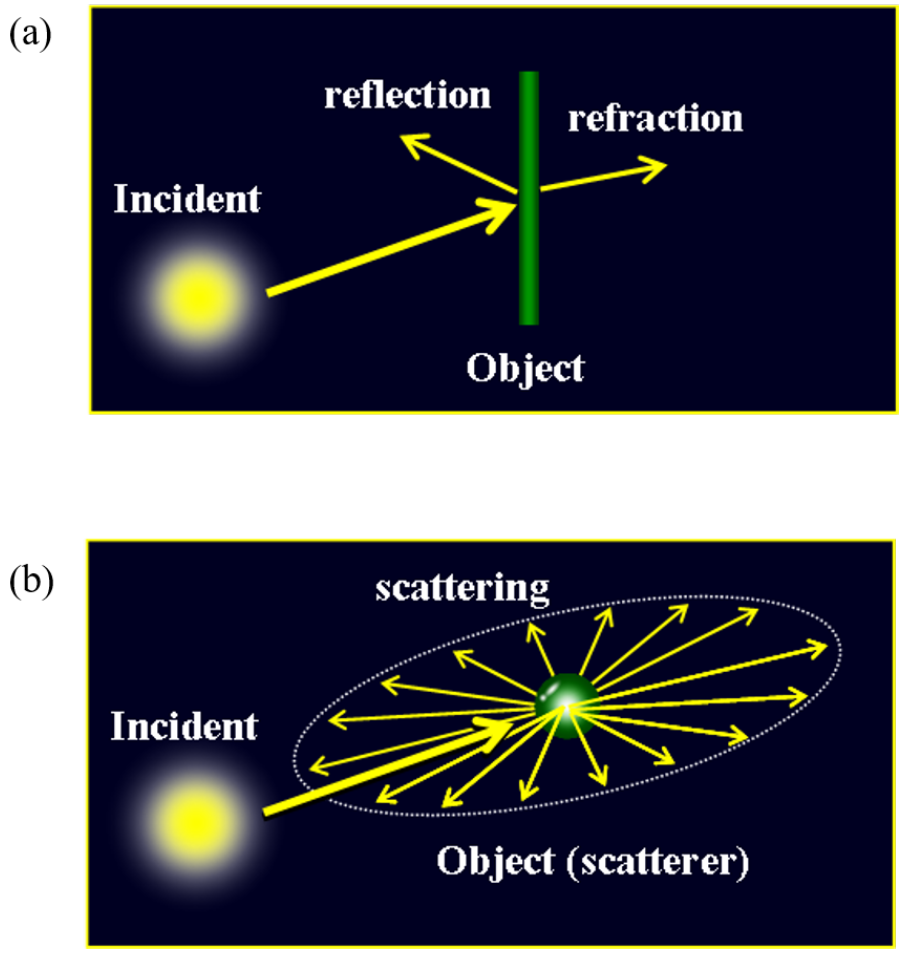

Fig. 1.1. (a) Reflection, refrection, and (b) scattering of light.

the theory of Rayleigh scattering describes dielectric (non-absorbing) scatterers with a small size. The criteria for Rayleigh scattering are a « 1 and |m|a « 1, where a = 2πr/λ, r is the scatterer radius, λ is the wavelength of the incident light, and m is the refractive index of the scatterer defined as m = n – ik (n indicates the refraction of light and the complex term, k, is related to absorption). Based on such criteria, the Rayleigh scattering theory is applicable for describing the light scattering caused by the scatterers with characteristic dimensions much smaller than the wavelength of incident light. In the region of Rayleigh scattering, the intensity of the light scattered by a single particle can be readily calculated with the following equation

$$I = I_0 \frac{1 + \cos^2\theta}{2d^2} \left(\frac{2\pi}{\lambda}\right)^4 \left|\frac{m^2 - 1}{m^2 + 2}\right|^2 r^6$$

where I_0 is the incident intensity, d is the distance to the particle, and θ is the scattering angle. By integrating over the sphere surrounding the particle, the Rayleigh scattering cross section, $\sigma_{scat,Rayleigh}$, can be given as

$$\sigma_{scat,Rayleih} = \frac{2\pi^5}{3} \frac{(2r)^6}{\lambda^4} \left|\frac{m^2 - 1}{m^2 + 2}\right|^2$$

From the above equation, it can be seen that the Rayleigh scattering cross sections are proportional to the 6th power of particle size, and inversely proportional to the 4th power of wavelength. This has been used to explain the blue color of our sky, as the air molecules (e.g. N_2 and O_2) are well within the

Rayleigh regime so that the shorter blue light of the sun can be scattered more efficiently than the longer red light.

In another case where the scattering system consists of large particles, i.e. the size of the particles is comparable to the wavelength of the incident light, Mie scattering theory is the only theoretical description is applicable. Note that the Mie scattering theory has no limitations to the particle size and can be used for scattering systems composed of spherical particles regardless of whether the particles is of a light absorbing or non-absorbing material. The cross section of Mie scattering is given by the expression

$$\sigma_{scat,Mie} = \frac{\lambda^2}{2\pi}\sum_{n=0}^{\infty}(2n+1)(|a_n|^2 + |b_a|^2)$$

where the parameters a_n and b_n are defined by the Riccati– Bessel functions ψ and ξ as

$$a_n = \frac{\psi_n(\alpha)\psi'_n(m\alpha) - m\psi_n(m\alpha)\psi'_n(\alpha)}{\xi(\alpha)\psi'_n(mx) - m\Psi_n(m\alpha)\xi'_n(\alpha)}$$

$$b_n = \frac{m\psi_n(\alpha)\psi'_n(m\alpha) - \psi_n(m\alpha)\psi'_n(\alpha)}{m\xi(\alpha)\psi'_n(m\alpha) - \psi_n(m\alpha)\xi'_n(\alpha)}$$

Accordingly, the Mie scattering efficiency, $\varrho_{scat,Mie}$, can be calculated by

$$\varrho_{scat,Mie} = \frac{\sigma_{scat,Mie}}{\pi r^2}$$

With these equations, the dependence of the Mie scattering efficiency on particle size and incident wavelength can be calculated. Shown in Fig. 2 is an

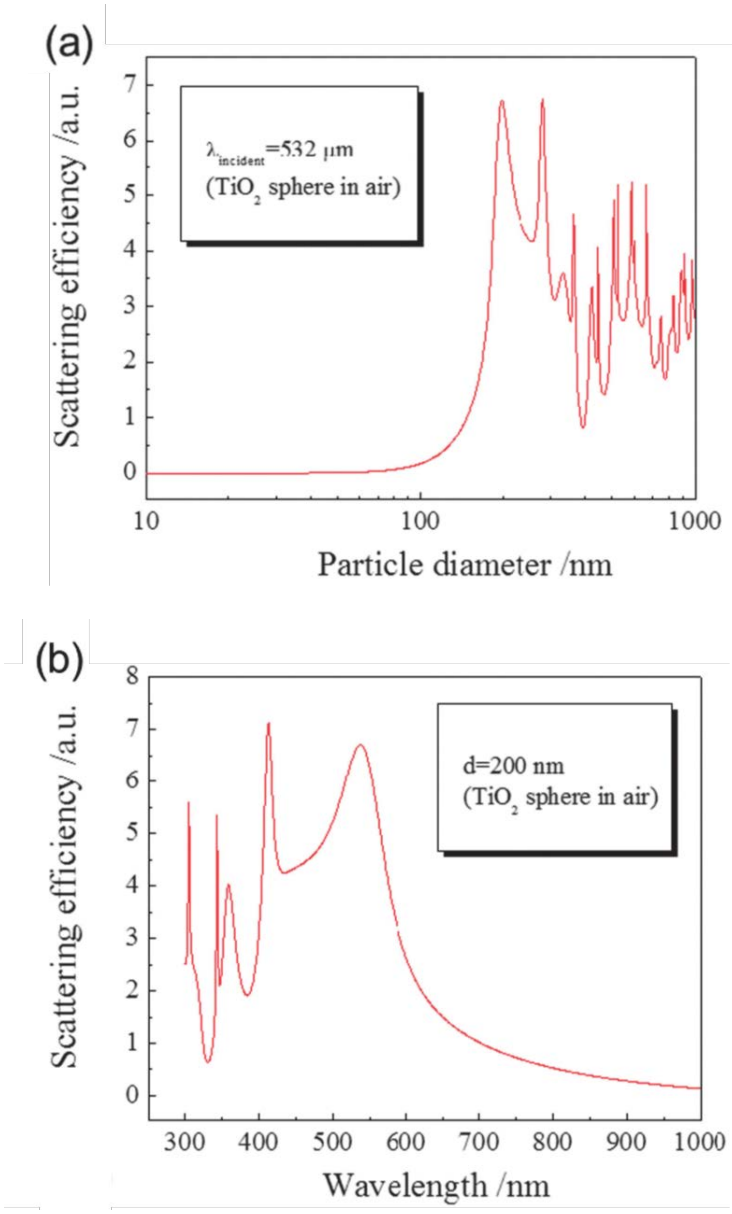

Fig. 1.2. The dependences of scattering efficiency on (a) particle size and (b) incident wavelength. (The calculation is based on a TiO_2 sphere in a surrounding medium of air)

example of calculation for scatterer being a sphere of TiO_2 material in air. From Fig. 1.2 (a) where the wavelength of incident light is set to 532 nm, it can be seen that an effective light scattering can only take place when the size of spherical scatterer is larger than 200 nm in diameter approximately half of the wavelength of incident light. The relation between the wavelength of incident light and the particle size can be further demonstrated by a calculation of the dependence of scattering efficiency on the wavelength of incident light for a spherical scatterer with fixed diameter. The result shown in Fig. 1.2 (b) is an example for 200 nm spherical scatterer, exhibiting that the light scattering mainly occurs in the wavelength range from ~400 nm to ~650 nm. One can therefore draw a rough conclusion from these calculations that, to achieve an effective light scattering, it is expected that the size of the scatterer is comparable to the wavelength of the incident light.

1.2 Titanium dioxide (TiO_2)

1.2.1. Chemical structure of TiO_2

The growth of industry worldwide has tremendously increased the generation and accumulation of waste byproducts. In general, the production of useful products has been focused on and the generation of waste byproducts has been largely ignored. This has caused severe environmental problems that have become a major concern. Researchers all over the world have been working on various approaches to address this issue. Photoinduced processes have been studied and various applications have been developed. One important technique for removing industrial waste is the use of light energy (electromagnetic radiation) and particles sensitive to this energy to mineralize waste which aids in its removal from solution. Titanium dioxide (TiO_2) is considered very close to an ideal semiconductor for photocatalysis because of its high stability, low cost and safety toward both humans and the environment.

TiO_2 belongs to the family of transition metal oxides. There are four commonly known polymorphs of TiO_2 found in nature: anatase (tetragonal), brookite (orthorhombic), rutile (tetragonal), and TiO_2 (B) (monoclinic) [4]. Besides these polymorphs, two additional high-pressure forms have been synthesized from the rutile phase. These are TiO_2 (II) [5] with a PbO_2 structure and TiO_2 (H) [6] with a hollandite structure. The crystal structures (Table 1) [7–9] and

properties of the rutile, anatase and brookite polymorphs are considered. Rutile: Rutile TiO_2 has a tetragonal structure and contains 6 atoms per unit cell (Fig. 1.3). The TiO_6 octahedron is slightly distorted. The rutile phase is stable at most temperatures and pressures up to 60 kbar, where TiO_2 (II) becomes the thermodynamically favorable phase [10]. Zhang et al. [11] found that anatase and brookite structures transformed to the rutile phase after reaching a certain particle size, with the rutile phase becoming more stable than anatase for particle sizes greater than 14 nm. Once the rutile phase formed, it grew much faster than the anatase. The activity of the rutile phase as a photocatalyst is generally very poor. However, Sclafani et al [12]. concluded that the rutile phase can be active or inactive, depending on its preparation conditions.

Anatase TiO_2 also has a tetragonal structure but the distortion of the TiO_6 octahedron is slightly larger for the anatase phase [9], as depicted in Fig. 1.3. Muscat et al. [13] found that the anatase phase is more stable than the rutile at 0 K, but the energy difference between these two phases is small (～2 to 10 kJ/mol). The anatase structure is preferred over other polymorphs for solar cell applications because of its higher electron mobility, low dielectric constant and lower density [14]. The increased photoreactivity is because of the slightly higher Fermi level, lower capacity to adsorb oxygen and higher degree of hydroxylation in the anatase phase [15]. Selloni [16] reported that the reactivity of (001) facets is greater than that of (101) facets in an anatase crystal. Yang et

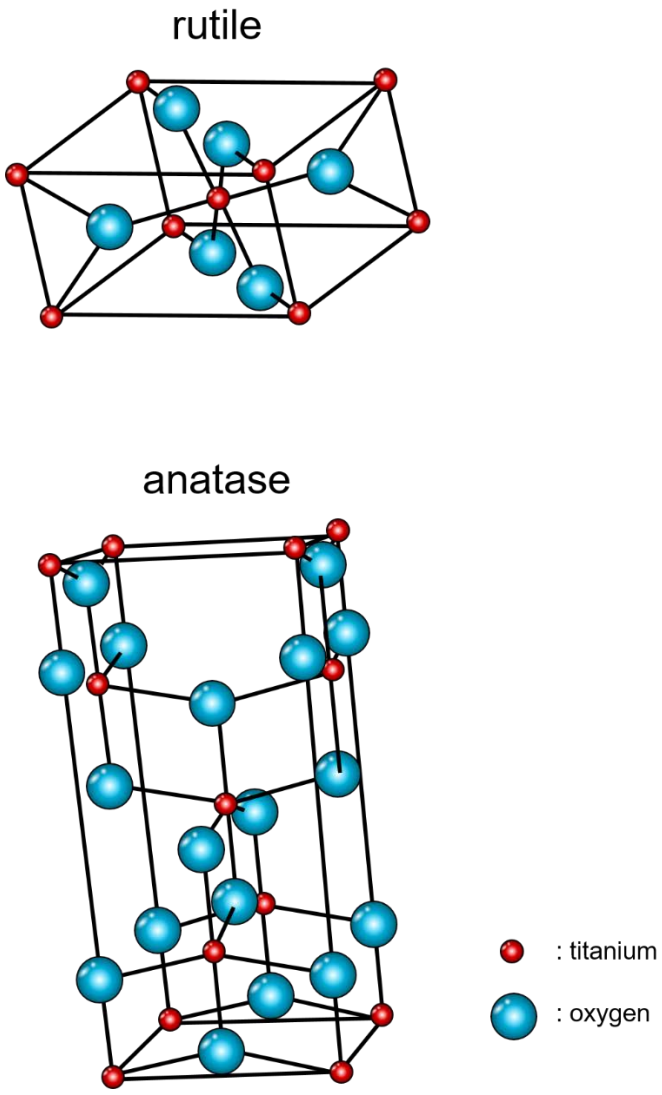

Fig. 1.3. Crystal structures of the rutile and anatase phases of TiO_2.

al. [17] synthesized uniform anatase crystals containing 47% (001) facets using hydrofluoric acid as a morphology controlling agent.

Brookite TiO_2 belongs to the orthorhombic crystal system. Its unit cell is composed of 8 formula units of TiO_2 and is formed by edge-sharing TiO_6 octahedra. It is more complicated, has a larger cell volume and is also the least dense of the 3 forms and is not often used for experimental investigations [18]. TiO_2 is a large band semiconductor, with band gaps of 3.2, 3.02, and 2.96 eV for the anatase, rutile and brookite phases, respectively [19]. The valence band of TiO_2 is composed of the 2p orbitals of oxygen hybridized with the 3d orbitals of titanium, while the conduction band is only the 3d orbitals of titanium [20]. When TiO_2 is exposed to near-UV light, electrons in the valence band are excited to the conduction band leaving behind holes (h^+), as shown in Fig. 1.4 (a). The excited electrons (e^-) in the conduction band are now in a purely 3d state and because of dissimilar parity, the transition probability of e– to the valence band decreases, leading to a reduction in the probability of e– /h+ recombination [21]. Anatase TiO_2 is considered to be the active photocatalytic component based on charge carrier dynamics, chemical properties and the activity of photocatalytic degradation of organic compounds. It has inherent surface band bending that forms spontaneously in a deeper region with a steeper potential compared with the rutile phase [22] thus surface hole trapping dominates because spatial charge separation

is achieved by the transfer of photogenerated holes towards the surface of the particle via the strong upward band bending. However, in the rutile phase, the bulk recombination of electrons and holes occurs, so only holes very close to the surface are trapped and transferred to the surface

1.2.2. TiO_2 nanoparticles

Various investigations have established that TiO_2 is much more effective as a photocatalyst in the form of nanoparticles than in bulk powder [23]. When the diameter of the crystallites of a semiconductor particle falls below a critical radius of about 10 nm, each charge carrier appears to behave quantum mechanically as a simple particle in a box (Fig. 1.4 (b)). As a result of this confinement, the band gap increases and the band edges shift to yield larger redox potentials [24]. However, the solvent reorganization free energy for charge transfer to a substrate remains unchanged. Because of the increased driving force and the unchanged solvent reorganization free energy, the rate constant of charge transfer in the normal Marcus region increases [25]. Using size-quantized semiconductor particles increases the photoefficiency of systems in which the rate-limiting step is charge transfer. Mill and Le Hunte [26] reported that because the absorption edge blue shifts with decreasing particle size, the redox potentials of the photogenerated electrons and holes in quantized semiconductor particles increased. In other words, quantized

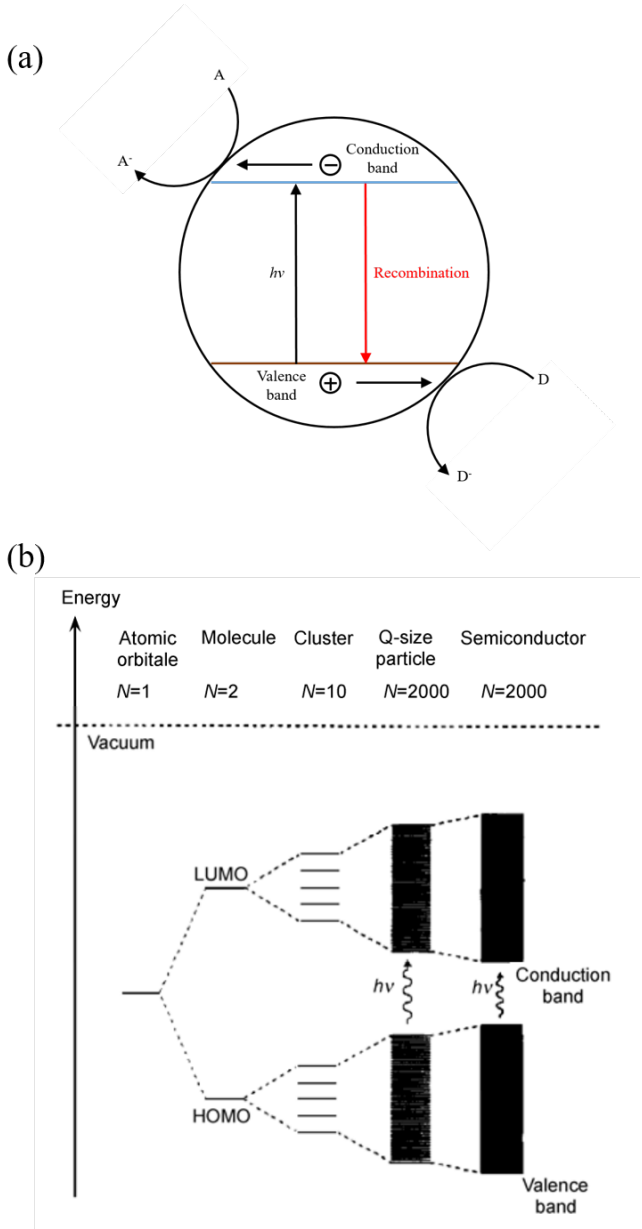

Fig. 1.4. (a) Mechanism of light absorption by TiO_2 and (b) molecular orbital model for particle growth of N monomeric units. The spacing of the energy levels varies among systems.

particles show higher photoactivity than macrocrystalline semiconductor particles. Recently, TiO_2 has been prepared in the form of powders, crystals, thin films, nanotubes and nanorods. Liquid phase processing is one of the most convenient and commonly used methods in chemical synthesis. This method provides the advantages of controlling the stoichiometry, homogeneous products and allowing the formation of complex shapes and preparation of composite materials. However, some disadvantages exist including expensive precursors, long processing times, and the presence of carbon as an impurity. Dawson et al. [27] subjected mixed phase TiO_2 powders with different compositions and particle sizes to hydrothermal reaction with NaOH. The anatase phase component of the starting material was easily converted to trititanate nanotubes at 140°C. At 170°C, the rutile phase reacted to form trititanate plates and belts. When the reaction time was increased to 7 days, all of the TiO_2 was converted to trititanate and the morphology of the resulting product was exclusively nanoplates and belts, with no nanotubes. Yana et al. [28] synthesized pure rutile nanotubes by a hydrothermal process in NaOH water-ethanol solution starting from rutile-anatase TiO_2 particles. The nanotubes were up to several micrometers in length and had diameters of less than 20 nm. The type of alcohol and the ratio to water had a great impact on the morphology and structure of the final products. The rutile nanotubes exhibited different optoelectronic properties to those of the raw TiO_2. Mozia et al. [29]

prepared modified titanate nanotubes (TNTs) via a hydrothermal method and focused on their application for the decomposition of Acid Red 18 (AR18) in water. Post-treatment calcination of the TNTs was carried out at temperatures of 400–700°C. The photocatalytic experiments revealed that the most active sample towards the decomposition of AR18 was TNTs calcined at 600°C. However, the photocatalytic activity of the calcined titanate nanotubes, was lower than that of P25 regardless of the annealing temperature. Among the products and byproducts of AR18 photodegradation, organic acids (formic, acetic and oxalic) and inorganic ions (nitrite, nitrate, ammonia and sulfate) were detected. Pradhan et al. [30] grew TiO_2 nanorods on a Tungsten carbide-Cobalt (WC–Co) substrate by metal-organic chemical vapor deposition. The diameter and length of the nanorods were about 50–100 nm and 0.5–2 mm, respectively. Nanorod growth was observed at 500°C, while most particles were deposited at 600°C and a thin coating was formed at 400°C. Limmer et al. [31] used sol electrophoretic deposition for template-based growth of TiO_2 nanorods. Uniform nanorods of approximately 45–200 nm in diameter and 10–60 μm in length were grown over large areas with almost unidirectional alignment. Attar et al. [32] fabricated aligned anatase and rutile TiO_2 nanorods and nanotubes with diameters of about 80–130 nm.

1.3 Aqueous and nonaqueous sol-gel chemistry

1.3.1. Aqueous sol-gel chemistry

The aqueous sol-gel process can shortly be defined as the conversion of a precursor solution into an inorganic solid via inorganic polymerization reactions induced by water. In general, the precursor or starting compound is either an inorganic (no carbon) metal salt (chloride, nitrate, sulfate, etc) or a metal organic compound such as an alkoxide. Metal alkoxides are the most widely used precursors, because they react readily with water and are known for many metals [33, 34]. In general, the sol-gel process consists of the following steps (Fig. 2.1) [35]: i) Preparation of a homogeneous solution either by dissolution of metal organic precursors in an organic solvent that is miscible with water, or by dissolution of inorganic salts in water; ii) conversion of the homogeneous solution into a sol by treatment with a suitable reagent (generally water with or without any acid/base); iii) aging; iv) shaping; and v) thermal treatment/sintering. The first step in a sol-gel reaction is the formation of an inorganic polymer by hydrolysis and condensation reactions, i.e., the transformation of the molecular precursor into a highly crosslinked solid. Hydrolysis leads to a sol, a dispersion of colloidal particles in a liquid, and further condensation results in a gel, an interconnected, rigid and porous inorganic network enclosing a continuous liquid phase. This transformation is

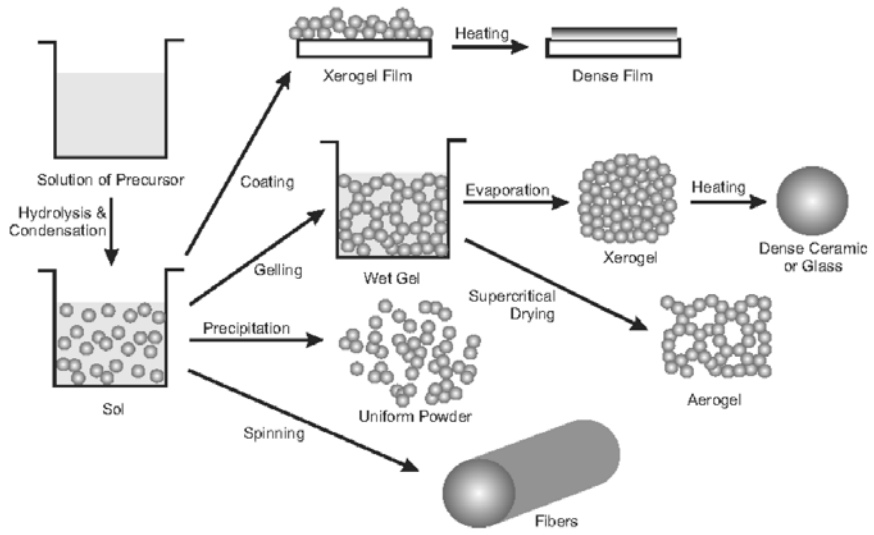

Fig. 1.5. Various steps in the sol-gel process to control the final morphology of the product.

called the sol-gel transition. There are two possibilities to dry the gels. Upon removal of the pore liquid under hypercritical conditions, the network does not collapse and aerogels are produced. When the gel is dried under ambient conditions, shrinkage of the pores occurs, yielding a xerogel. One of the highly attractive features of the sol-gel process is the possibility to shape the material into any desired form such as monoliths, films, fibers, and monosized powders, and subsequently to convert it into a ceramic material by heat treatment. As mentioned before, the sol-gel processes can be classified into two different routes depending on the nature of the precursors: a) the precursor is an aqueous solution of an inorganic salt or b) a metal organic compound. The aqueous chemistry of transition metal ions can be rather complicated because of the formation of a large number of oligomeric species, depending on the oxidation state, the pH or the concentration. The sol-gel conversion of metal alkoxides involves two main reaction types: hydrolysis and condensation (Fig. 1.6). During hydrolysis, the alkoxide groups (-OR) are replaced via the nucleophilic attack of the oxygen atom of a water molecule under release of alcohol and the formation of a metal hydroxide. Condensation reactions between two hydroxylated metal species leads to M-O-M bonds under release of water (oxolation), whereas the reaction between a hydroxide and an alkoxide leads to M-O-M bonds under release of an alcohol (alkoxolation). Chemical aspects play an important role in studying and controlling the sol-gel process. The

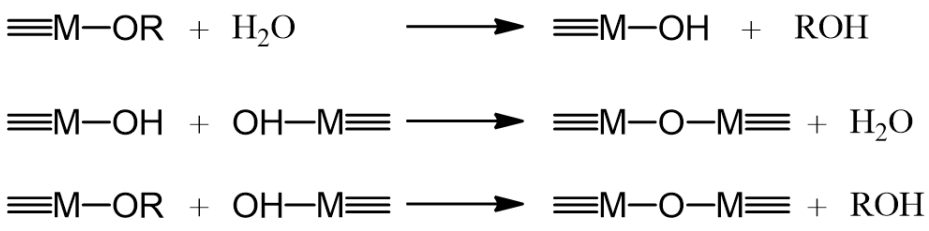

Fig. 1.6. Main reactions in the sol-gel process using metal alkoxides. Hydrolysis and condensation, involving oxolation and alkoxolation.

chemical reactivity of metal alkoxides towards hydrolysis and condensation depends mainly on the electronegativity of the metal atom, its ability to increase the coordination number, the steric hindrance of the alkoxy group, and on the molecular structure of the metal alkoxides (monomeric or oligomeric). The major problem of sol-gel methods based on the hydrolysis and condensation of molecular precursors is the control over the reaction rates. For most transition metal oxide precursors, these reactions are too fast, resulting in loss of morphological and also structural control over the final oxide material. Furthermore, the different reactivities of metal alkoxides make it difficult to control the composition and the homogeneity of complex multi-metal oxides by the sol-gel process.

1.3.2. Nonaqueous sol-gel chemistry

In nonaqueous sol-gel chemistry the transformation of the precursor takes place in an organic solvent under exclusion of water. In comparison to aqueous sol-gel chemistry, the list of potential precursors is longer and includes, in addition to inorganic metal salts and metal alkoxides, also metal acetates and metal acetylacetonates. Organometallic compounds are also frequently used, but then the process is rather based on thermal decomposition than sol-gel (remember: organometallic compounds are defined as having a direct metal-carbon bond,

whereas metal organic compounds have a metal-hetero atom (usually oxygen) bond between the metal center and the organic ligand). Nonaqueous sol-gel processes have a long history, although they never became as popular as their aqueous analogs. Two main research directions could be distinguished: One focusing on the preparation of metal oxide gels, the other on metal oxide powders. Several groups worked on the preparation of powders using metal alkoxides and alcohols [36-38] or inert organic solvents [38-40]. Especially the glycothermal method involving the reaction of metal alkoxides or acetylacetonates with 1,4-butanediol is a versatile approach to various metal oxides [41] and has recently been reviewed [42]. Nowadays, the family of metal oxide nanoparticles that are prepared by nonaqueous processes has grown immensely and ranges from simple binary metal oxides to more complex ternary, multi-metal and doped systems. In nonaqueous systems, where intrinsically no water is present, the question arises, where the oxygen for the metal oxide comes from. Analogous to the nonhydrolytic preparation of bulk metal oxide gels [38], the oxygen for nanoparticle formation is provided by the solvent (ethers, alcohols, ketones or aldehydes) or by the organic constituent of the precursor (alkoxides or acetylacetonates). It is interesting to note that in spite of the large number of methodologies reported for the nonaqueous synthesis of metal oxide nanoparticles, and independent whether surfactants are used or not, most of the known condensation steps, i.e., the formation of the

metal-oxygen-metal bond as basic structural unit, can be summarized in only five distinct pathways (Fig. 1.7) [43, 44].

Alkyl halide elimination, the condensation between metal halides and metal alkoxides (either initially added, or formed upon the reaction of metal halides with alcohols) under release of an alkyl halide, is shown in Eq. 1.1. Ether elimination (Eq. 1.2) is the result of the reaction between two metal alkoxides. The ester elimination process involves the reaction between metal carboxylates and metal alkoxides or between metal carboxylates and alcohols (Eq. 1.3). Analogous to ester eliminations are amide eliminations, e.g. reactions between metal carboxylates and amines. Alkyl halide, ether and ester eliminations are the most commonly reported routes. However, due to the excellent catalytic activity of the metal centres in the precursor species peculiar and more complex organic reactions such as C-C bond formation between alkoxy groups were also observed (Eq. 1.4). Whereas in some cases the presence of a basic species was a prerequisite for C-C bond formation, transition metals with high Lewis acidity, such as Nb, Y, and Ce, were able to directly catalyse this Guerbet-like reaction. If ketones are used as solvents, the release of oxygen usually involves aldol condensation, where two carbonyl compounds react with each other under formal elimination of water (Eq. 1.5). The water molecules act as oxygen supplying agent for the metal oxide formation.

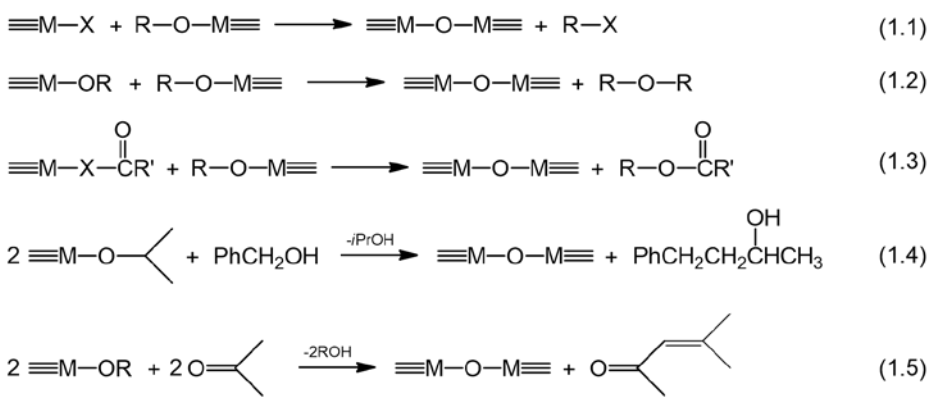

Fig. 1.7. Main condensation steps in nonaqueous sol-gel processes resulting in the formation of a metal-oxygen-metal bond. Alkyl halide elimination (Eq. 1.1), ether elimination (Eq. 1.2), ester elimination (Eq. 1.3), C-C bond formation between benzylic alcohols and alkoxides (Eq. 1.4), aldol condensation reactions (Eq. 1.5).

1.3.3. Sol-gel method for TiO_2 nanoparticles

TiO_2 nanoparticles have been synthesized with the sol-gel method from hydrolysis of a titanium precursor [45]. This process normally proceeds via an acid-catalyzed hydrolysis step of titanium(IV) alkoxide followed by condensation [45, 46]. The development of Ti-O-Ti chains is favored with low content of water, low hydrolysis rates, and excess titanium alkoxide in the reaction mixture. Three-dimensional polymeric skeletons with close packing result from the development of Ti-O-Ti chains. The formation of $Ti(OH)_4$ is favored with high hydrolysis rates for a medium amount of water. The presence of a large quantity of Ti-OH and insufficient development of three-dimensional polymeric skeletons lead to loosely packed first-order particles. Polymeric Ti-O-Ti chains are developed in the presence of a large excess of water. Closely packed first-order particles are yielded via a three-dimensionally developed gel skeleton [45-47]. From the study on the growth kinetics of TiO_2 nanoparticles in aqueous solution using titanium tetraisopropoxide (TTIP) as precursor, it is found that the rate constant for coarsening increases with temperature due to the temperature dependence of the viscosity of the solution and the equilibrium solubility of TiO_2 [46]. Secondary particles are formed by epitaxial self-assembly of primary particles at longer times and higher temperatures, and the number of primary particles per secondary particle increases with time. The average TiO_2 nanoparticle radius increases linearly with time, in agreement

with the Lifshitz-Slyozov-Wagner model for coarsening [46].

1.4. Application

1.4.1. Dye-sensitized solar cells

Dye-sensitized solar cell (DSSC) is a semiconductor photovoltaic device that directly converts solar radiation into electric current. The operational principle of DSSC is illustrated in Fig. 1.8. The system consists of the following:

(i) a transparent anode made up of a glass sheet treated with a transparent conductive oxide layer;

(ii) a mesoporous oxide layer (typically, TiO_2) deposited on the anode to activate electronic conduction;

(iii) a monolayer charge transfer dye covalently bonded to the surface of the mesoporous oxide layer to enhance light absorption;

(iv) an electrolyte containing redox mediator in an organic solvent effecting dye-regenerating; and

(v) a cathode made of a glass sheet coated with a catalyst (typically, platinum) to facilitate electron collection.

When exposed to sunlight, the dye sensitizer gets excited from which an electron is injected into the conduction band of the mesoporous oxide film. These generated electrons diffuse to the anode and are utilized at the external load before being collected by the electrolyte at cathode surface to complete the cycle. In order to enhance electrical conductivity and light transmittance, conducting

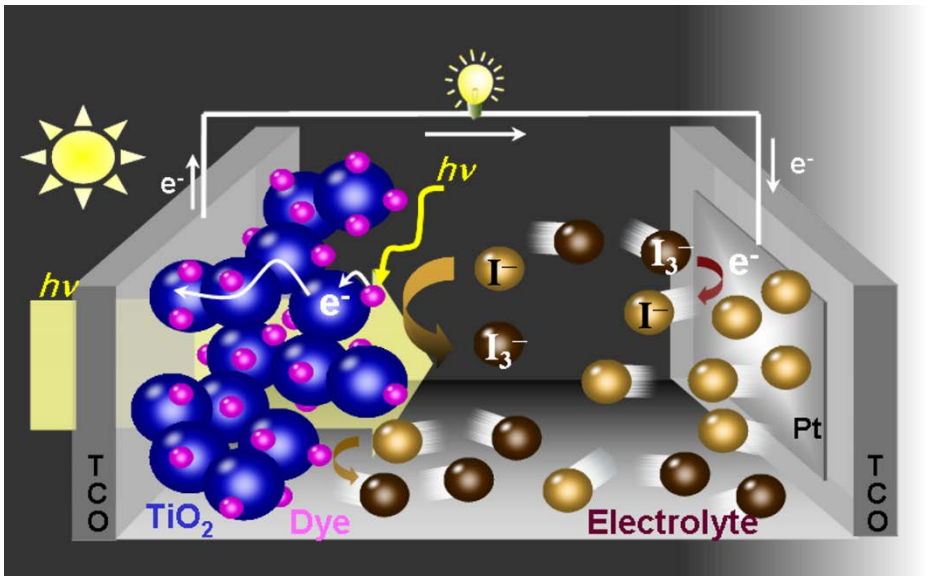

Fig. 1.8. Schematic diagram of the dye-sensitized solar cell.

glass is used as the substrate. There are mainly two types of conducting glass: indium-doped tin oxide (ITO) and fluorine-doped tin oxide (FTO). The standard to select a proper type is sometimes ambiguous because of the variety of cell configurations and materials [48]. The semiconductor electrode is usually a layer of nanocrystalline titanium dioxide (TiO_2), a thin film deposited on the conducting glass film with the thickness ca. 5–30 mm, which plays an important role in both the exciton dissertation and the electron transfer process. The porosity and morphology of the TiO_2 layer are dominant factors that determine the amount of dye molecules absorbed on its surface which can provide an enormous area of reaction sites for the monolayer dye molecules to harvest incident light. A large number of artificial dye molecules have been synthesized since the first introduction of dye-sensitized solar cells and some of them have already been successfully commercialized such as N3, N719 and Z907. Desirable dye molecules have to meet certain criteria, such as match with the solar spectrum, long-term operational stability, and firm graft on the semiconductor surface. In addition, their redox potential should be high enough to facilitate the regeneration reaction with a redox mediator [49]. As such, iodide and triiodide (I/I_3^-) redox couple is most commonly used in the liquid electrolyte, while other solid-state and quasi-solid electrolytes like organic hole-transport material and polymer gel are also applicable [50, 51]. Platinum is generally used as the cathode to catalyze the reduction of the oxidized charge mediator [52].

The overall performance of the above described solar cell can be evaluated in terms of cell efficiency (η) and fill factor (FF) expressed as

$$\mathrm{FF} = \frac{V_{max}J_{max}}{V_{oc}J_{sc}}$$

$$\eta = \frac{V_{oc}J_{sc}FF}{P_{in}} \times 100\%$$

where J_{sc} is the short-circuit current density (mA/cm^2), V_{oc} the open-circuit voltage (V), and P_{in} the incident light power. J_{max} and V_{max} correspond to current and voltage values, respectively, where the maximum power output is given in the J–V curve. In the band gap theory, the difference between the quasi-Fermi level of the TiO_2 layer and the electrolyte redox potential determines the maximum voltage generated under illumination. As shown in the above equation, the open-circuit voltage varies with the iodide concentration because the recombination reaction occurs between the electrons on the conduction band of TiO_2 and I_3^- (triiodide) [53].

$$V_{oc} = \frac{kT}{q} ln\left(\frac{\eta\phi_0}{n_0 k_{et}[I_3^-]}\right)$$

where η is the quantum yield of photogenerated electron for the given incident photoflux (Φ_0); n_0 represents the electron density on the conduction band of TiO_2 in the dark, while k_{et} reflects the recombination reaction rate for the given triiodide concentration [I_3^-]. Similarly, the precise value of J_{sc} can be calculated by integrating the product of incident photon to current efficiency (IPCE) and

incident photoflux (Φ_0) over the spectral distribution, expressed as

$$J_{sc} = \mathrm{e} \int IPCE(\lambda)\Phi_0(\lambda)\big(1 - r(\lambda)\big)d\lambda$$

where 'e' is the elementary charge and r(λ) is the incident light loss. One prominent approach to improve the circuit current density (J_{sc}) is to increase the IPCE value by utilizing panchromatic dyes which can absorb incident light at a longer wavelength.

Yet another parameter that influences the efficiency of the DSSC is the fill factor (FF) which is associated with the electron transfer process and internal resistance of dye-sensitized solar cells. A variety of equivalent circuits have been elaborated to interpret data obtained from electrochemical impedance spectroscopy [54, 55]. Based on the equivalent circuit study, it is shown that FF can be optimized by minimizing internal series resistance.

1.4.2. Photocatalysis

Photocatalysis is the acceleration of a photoreaction in the presence of a catalyst, which can absorb light quanta of appropriate wavelengths depending on the band structure [56, 57]. Among the common semiconductors, titanium dioxide (TiO_2) displays outstanding properties as a photosensitive catalyst, such as long-term chemical stability, nontoxicity, strong oxidizing activity, and good photo-stability, that make TiO_2 ideal for the treatment of organic pollutants in water and

contaminated air [58, 59]. These properties are attributed to the large band gap of 3.2 eV for the anatase form and the frequent recombination of photogenerated electron-hole pairs. To date, TiO_2 is a benchmark material for photocatalytic reactions and has been intensively investigated. Unfortunately, the wide band gap restricts the excitation of TiO_2 semiconductors to high-energy ultraviolet (UV) radiation of wavelengths less than 388 nm. UV radiation accounts for less than 5% of the entire solar spectrum, and 45% of the solar spectral energy is contained in the visible light [60, 61]. To improve the efficient utilization of solar light, visible light-responsive novel photocatalysts with narrow band gaps must be developed in which the absorption wavelength range is extended into the visible region. (see Figure I-8) Such efforts are an active research area for environmental remediation applications [62]. With the development of nanotechnology, substantial attention has been focused on architecture and composition control toward particular applications. Mesostructured and mesoporous materials are useful in applications that rely on surface or interface properties, such as a high surface-to-volume ratio, particular morphologies (including shape and multi-dimensionality), well-defined topologies, and pore diameters appropriate for particular applications (2–5 nm in size) [63, 64]. Efforts have focused on the development of techniques for producing mesoporous carbon, silica and titania-based materials to achieve superior catalytic performance and utilization efficiencies [65-67]. A previous

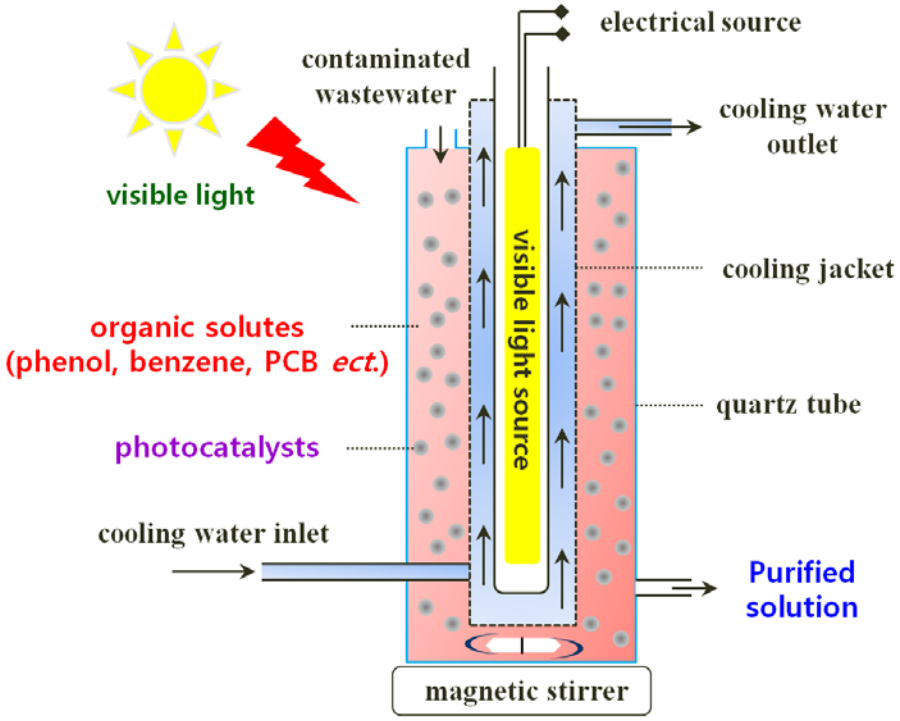

Fig. 1.9. Schematics of organic solute decomposition using visible light-active photocatalysts.

report described the preparation of well-defined highly crystalline spherical mesoporous TiO_2 with a large internal surface area and continuous pore channels using a simple sol-gel approach in aqueous solutions. The photocatalytic activity of these particles was found to be better than that of nonporous commercial TiO_2 [68].

One of the major drawbacks of pure TiO_2 is the large band gap implying that this material can only be activated using an irradiation with photons in the UV region ($\leq$ 387 nm). In order to obtain activity in the visible region, it is essential to modify the semiconductor materials by using dye sensitization, noble metal loading, transition metal addition and non-metal doping. Modification with transition metal ions was the first method reported for their visible-light activation of TiO_2 [69]. The main drawback of these catalysts is the formation of recombination sites for photogenerated charge carriers and thus lowering the quantum efficiency. Transition metals also block the active surface reaction sites. In 1986 Sato discovered that modification of TiO_2 with NH_4OH resulted in their visible light absorption [70]. Later Asahi et al. for the first time investigated the photocatalytic activity of N-doped TiO_2 [71]. Dye-sensitization is one of the widely used techniques for the utilization of visible-light in photocatalytic and photovoltaic systems [72–74]. During visible-light irradiation, excited electrons are transferred from the dyes to the conduction band of the semiconductor (Fig. 8). Some dyes are even capable of producing electrons by absorbing visible-light

in the absence of semiconductors. Dye-sensitization was identified as highly effective for the degradation of a number of pollutants under visible irradiation [75, 76].

1.5. Research Objectives

With this background and the technological and scientific value of light scatterers as motivations, the preparation of TiO_2 clusters as light scattering centers with specific characteristics is both desirable and technologically important. In this study, spherical- and bowl- shaped mesoporous TiO_2 clusters as light scattering centers were developed using aqueous and nonaqueous sol-gel process, then applied to solar cell and photocatalysis.

In chapter 2, we synthesized spherical mesoporous TiO_2 clusters in various sizes using a sing titanium precursor (titanium (IV) isopropoxide) and various amphiphilic triblock copolymers ($PEO_x - PPO_y - PEO_x$, where PEO is poly(ethylene oxide) and PPO is poly(propylene oxide)). The triblock copolymer is used as structure-directing and pore-forming agent and the interaction between the titanium precursor and the triblock copolymer self-assemblies in solvent leads to the assembly of TiO_2 nanoparticles into spherical aggregates with wormhole-like porous structures. The triblock copolymer micelle was composed of a core dominated by PO and a corona dominated by EO segments. The core of the micelles was believed to be free of water, while the swollen corona was hydrated. The aggregation behavior of the triblock copolymer under thermodynamic conditions may affect the TiO_2 cluster size

and morphology. A reasonable model for the size-controlled mechanism of these spherical cluster is proposed and discussed in more detail.

In chapter 3, we prepared the spherical TiO_2 with the mesoporous framework to increase the specific surface area and to improve the incorporation efficiency of ZnPc, which can further enhance the visible light photocatalytic activity. The mesoporous TiO_2/ZnPc hybrids were synthesized with the varied size to investigate the effect of Mie scattering on the photocatalytic activity of TiO_2/ZnPc hybrid. We showed that the scattering efficiency of the incident visible light is dependent on the diameter of ZnPc-incorporated mesoporous TiO_2 spheres. When the size of TiO_2/ZnPc hybrid was comparable to the wavelength of incident visible light, the mesoporous TiO_2/ZnPc exhibited the highest photocatalytic decomposition activity due to the cascade Mie scattering effect. The enhanced photocatalytic activity of mesoporous TiO_2/ZnPc by Mie scattering makes it tremendously attractive for applications ranging from water purification to hydrogen generation. In addition, the simplicity of the current process to produce mesoporous TiO_2/ZnPc makes it attractive for large-scale production [77].

In chapter 4, we fabricated composite-type photoelectrodes consisting of TiO_2 spheres mixed with small TiO_2 particles as the binder. In order to further

improve the connectivity between the TiO_2 spheres, we used the hot-pressing compression technique to prepare TiO_2 electrodes on fluorine doped tin oxide (FTO) substrates. This hot-press technique was found to improve the connectivity between the TiO_2 spheres, as well as the mechanical adhesion of the TiO_2 electrode to the FTO substrate. These composite-type electrodes were used as scattering layers and working electrodes in DSSC devices and their effects on the conversion efficiency of the devices were investigated [78].

In chapter 5, we were motivated to develop a novel bowl-shaped scattering layer with TiO_2 nanorod clusters as an over-layer for DSSC photoelectrodes. In the electrode we made, the cluster had mesoporous structures with a relatively larger surface area compared to the conventional one, hence this unique shape of the TiO_2 nanorods-based cluster provided a direct pathway for the electron transport as well as an enhanced aggregation-induced light scattering for the range of visible-light wavelength. The DSC based on bowl TiO_2 scattering layer exhibits remarkably enhanced photovoltaic properties compared with that based on spherical TiO_2 scattering layer. It is shown that these TiO_2 materials have a good energy conversion properties for the DSSCs due to the multi-light scattering inside. Overall, we have provided a particular method to prepare hierarchical TiO_2 nanomaterials hat can integrate morphologies of spheres and bowls with high specific surface area and high

pore volume. The enhanced light scattering ability of bowl-shaped TiO_2 cluster by multiple scattering makes it tremendously attractive for applications ranging from water purification to hydrogen generation. In addition, the simplicity of the current process to produce bowl-shaped cluster makes it attractive for large-scale production. To the best of our knowledge, this is the first demonstration of such bowl scattering layer based on TiO_2 nanorods for coordinately promoting charge-collection efficiency and light harvesting capability [79].

References

1. C. Bohren, D. Huffman, Absorption and scattering of light by small particles, John Wiley & Sons, New York, 1983.
2. H. Hulst, Light Scattering by Small Particles, Dover Publications, New York, 1981.
3. M. Kerker, The Scattering of Light and Other Electromagnetic Radiation, Academic, New York, 1969.
4. O. Carp, C. L. Huisman, A. Reller, Prog. in Solid State Chem. 32 (2004) 33–117.
5. P. Y. Simons, F. Dachille, Acta Cryst. 23 (1967) 334–336.
6. M. Latroche, L. Brohan, R. Marchand, J. Solid State Chem. 81 (1989) 78–82.
7. D. T. Cromer, K. Herrington, J. Am. Chem. Soc. 77 (1955) 4708–4709.
8. V. W. H. Baur, Acta Crystallogr. 14 (1961) 214–216.
9. S. Mo, W. Ching, Phys. Rev. B 51 (1995) 13023–13032.
10. A. Norotsky, J. C. Jamieson, O. J. Kleppa, Science 158 (1967) 338–389.
11. Q. Zhang, L. Gao, J. Guo, Appl. Catal. B Environ. 26 (2000) 207–215.
12. A. Sclafani, L. Palmisano, M. Schiavello, J. Phys. Chem. 94 (1990) 829–832.
13. J. Muscat, V. Swamy, N. M. Harrison, Phy. Rev. B 65 (2002) 1–15.
14. O. Carp, C. L. Huisman, A. Reller, Prog. in Solid State Chem. 32 (2004) 33–117.
15. K. Tanaka, M. F. V. Capule, T. Hisanaga, Chem. Phys. Lett. 187 (1991) 73–76.
16. A. Selloni, Nature Mater. 7 (2008) 613–615.
17. H. G. Yang, C. H. Sun, S. Z. Qiao, Nature 453 (2008) 638– 641.
18. T. L. Thompson, J. T. Yates Jr, Chem. Rev. 106 (2006) 4428–4453

19. W. Wunderlich, T. Oekermann, L. Miao, J. Ceram. Process Res. 5 (2004) 343–354.
20. A. T. Paxton, L. Thiên-Nga, Phys. Rev. B 57 (1998) 1579–1584.
21. S. Banerjee, J. Gopal, P. Muraleedharan, Current Sci. 90 (2006) 1378–1383.
22. G. Li, L. Chen, M. E. Graham, J, Mol. Catal. A Chem. 275 (2007) 30–35.
23. H. Han, R. Ba, Ind. Eng. Chem. Res. 48 (2009) 2891–2898.
24. M. R. Hoffmann, S. T. Martin, W. Choi, Chem. Rev. 95 (1995) 69–96.
25. R. A. Marcus, J. Phys. Chem. 94 (1990) 1050–1055.
26. A. Mills, A. J. Hunte, J. Photochem. Photobiol. A Chem. 108 (1997) 1–35.
27. G. Dawson, W. Chen, T. Zhang, Solid State Sci. 12 (2010) 2170–2176.
28. J. Yana, S. Fenga, H. Lua, Mat. Sci. Eng. B 172 (2010) 114–120.
29. S. Mozia, Catalysis Today, 156 (2010) 198–207.
30. S. K. Pradhan, P. J. Reucroft, F. Yang, J. Crystal Growth 256 (2003) 83–88.
31. S. J. Limmer, T. P. Chou, G. Z. Cao, J. Mat. Sci. 39 (2004) 895–901.
32. A. S. Attar, M. S. Ghamsari, F. Hajiesmaeilbaigi, J. Mat. Sci. 43 (2008) 5924–5929.
33. N. Y. Turova, E. P. Turevskaya, The chemistry of metal alkoxides, Kluwer Academic Publishers, Boston (2002).
34. D. C. Bradley, R. C. Mehrotra, I. P. Rothwell, A. Singh, Alkoxo and aryloxo derivatives of metals, Academic Press, London (2001).
35. R. C. Mehrotra, A. Singh, Prog. Inorg. Chem. 46 (1997) 239–454.
36. A. J. Fanelli, J. V. Burlew, J. Am. Ceram. Soc. 69 (1986) C174–C175.
37. M. Inoue, K. Kitamura, H. Tanino, H. Nakayama, T. Inui, Clays Clay

Miner. 37 (1989) 71–80.
38. M. Inoue, H. Kominami, T. Inui, Appl. Catal., A 97 (1993) L25–L30.
39. M. Inoue, H. Kominami, H. Otsu, T. Inui, Nippon Kagaku Kaishi (1991) 1364–1366.
40. M. Inoue, H. Kominami, T. Inui, J. Am. Ceram. Soc. 75 (1992) 2597–2598.
41. H. Kominami, M. Inoue, T. Inui, Catal. Today 16 (1993) 309–317.
42. M. Inoue, J. Phys. Condens. Matter 16 (2004) S1291–S1303.
43. M. Niederberger, Acc. Chem. Res. 40 (2007) 793–800.
44. M. Niederberger, G. Garnweitner, Chem. Eur. J. 12 (2006) 7282–7302.
45. Y. Bessekhouad, D. Robert, J. V. F. Weber, Photochem. Photobiol. A 157 (2003) 47.
46. G. Oskam, A. Nellore, R. L. Penn, P. C. Searson, J. Phys. Chem. B 107 (2003) 1734.
47. T. Sugimoto, Adv. Colloid Interface Sci. 28 (1987) 65.
48. C. Sima, C. Grigoriu, S. Antohe, Thin Solid Films 519 (2010) 595–597.
49. A. Hagfeldt, M. Gratzel, Acc. Chem. Res. 33 (2000) 269–277.
50. B. O'Regan, F. Lenzmann, R. Muis, J. Wienke, Chem. Mater. 14 (2002) 5023–5029.
51. T. Taguchi, X. T. Zhang, I. Sutanto, K. Tokuhiro, T. N. Rao, H. Watanabe, T. Nakamori, M. Uragami, A. Fujishima, Chem. Commun. 19 (2003) 2480–2481.
52. P. Calandra, G. Calogero, A. Sinopoli, P. G. Gucciardi, Catalyst 3 (2010) 4a.
53. Z. Lan, J. Wu, D. Wang, S. Hao, J. Lin, Y. Huang, Solar Energy 81 (2007) 117–122.
54. L. Han, N. Koide, Y. Chiba, A. Islam, T. Mitate, Appl. Phys. Lett. 84

(2004) 2433–2435.

55. Q. Wang, J. E. Moser, M. Gratzel, J. Phys. Chem. B 109 (2005) 14945–14953.
56. S. Banerjee, S.C. Pillai, P. Falaras, K.E. O'Shea, J.A. Byrne, D.D. Dionysiou, J. Phys. Chem. Lett. 5 (2014) 2543.
57. M. Pelaez, N.T. Nolan, S.C. Pillai, M.K. Seery, P. Falaras, A.G. Kontos, P.S.M. Dunlop, J.W.J. Hamilton, J.A. Byrne, K. O'Shea, M.H. Entezari, D.D. Dionysiou, Appl. Catal. B 125 (2012) 331.
58. Z. H. Zhang, Y. Yuan, G. Y. Shi, Y. J. Fang, L. H. Liang, H. C. Ding and L. T. Jin, Environ. Sci. Technol. 41 (2007) 6259.
59. S. Kohtani, M. Tomohiro, K. Tokumura and R. Nakagaki, Appl. Catal. B: Environ. 58 (2005) 265.
60. R. Asahi, T. Morikawa, T. Ohwaki and Y. Taga, Science 293 (2001) 269.
61. C. H. An, S. Peng and Y. G. Sun, Adv. Mater. 22 (2010) 2570.
62. H. Zhang, G. Chen and D. W. Bahnemann, J. Mater. Chem. 19 (2009) 5089.
63. Y. Ren, A. R. Armstrong, F. Jiao and P. G. Bruce, J. Am. Chem. Soc. 132 (2010) 996.
64. IUPAC *Manual of Symbols and Terminology*, Appendix 2, Part 1, Colloid and Surface Chemistry, Pure Appl. Chem. 31 (1972) 578.
65. J. Liu, S. Z. Qiao, Q. H. Hu and G. Q. Lu, Small 7 (2011) 425.
66. S. Araki, H. Doi, Y. Sano, S. Tanaka and Y. Miyake, J. Colloid Interf. Sci. 339 (2009) 382.
67. G. Li, E. T. Kang, K. G. Neoh and X. Yang, Langmuir 25 (2009) 4361.
68. D. S. Kim, S. J. Han and S.–Y. Kwak, J. Colloid Interface Sci. 316 (2007) 85.
69. E. Borgarello, J. Kiwi, M. Gratzel, E. Pelizzetti, M. Visca, J. Am. Chem.

Soc. 104 (1982) 2996.

70. S. Sato, Chem. Phys. Lett. 123 (1986) 126.
71. R. Asahi, T. Morikawa, T. Ohwaki, K. Aoki, Y. Taga, Science 293 (2001) 269.
72. K. Gurunathan, P. Maruthamuthu, V. Sastri, Int. J. Hydrogen Energy 22 (1997) 57.
73. K. Dhanalakshmi, S. Latha, S. Anandan, P. Maruthamuthu, Int. J. Hydrogen Energy 26 (2001) 669.
74. A. Jana, J. Photochem. Photobiol. A 132 (2000) 1.
75. P. Chowdhury, J. Moreira, H. Gomaa, A.K. Ray, Ind. Eng. Chem. Res. 51 (2012) 4523.
76. G. Qin, Z. Sun, Q. Wu, L. Lin, M. Liang, S. Xue, J. Hazard. Mater. 192 (2011) 599.
77. H. –J. Kim, J. –D. Jeon, J. W. Chung, S. –Y. Kwak, Microporous Mesoporous Mater. 227 (2016) 169.
78. H. –J. Kim, J. –D. Jeon, S. –Y. Kwak, Powder Technol. 243 (2013) 130.
79. H. –J. Kim, J. –D. Jeon, J. W. Chung, S. –Y. Kwak, Microporous Mesoporous Mater. 198 (2014) 170.

Chapter 2

Synthesis of Size-Controlled TiO_2 Spheres Using Various Surfactant

2.1 Introduction

Titanium dioxide (TiO_2) has been commonly used as white pigments from ancient times. It is inexpensive, chemically stable and harmless, and has no absorption in the visible region. For this reason, it has been widely investigated for applications in photocatalysis [1], photovoltaic cells [2], electronic devices [3], and sensors [4]. Experimental approaches have been reported to control the shape or aggregate architecture of this material toward more advanced applications. One is to reduce the dimensionality of the TiO_2 nanoparticles. Dimensionality becomes a key factor in determining the properties of nanomaterials. A one-dimensional (1-D) shape of TiO_2, for example, provides possibilities for improving the performance in applications due to their unique advantages of fast charge transport [5]. Anisotropic growth has been used as a facile method for the preparation of 1-D nanomaterial by taking advantage of the difference of growth rate on the different crystalline facets, leading to preferential growth on a certain orientation [6]. Another approach is to fabricate the porous aggregate architectures, such as spheres [7], hollow spheres [8], and

beads [9]. These porous structures have attracted widespread interests in different frontier areas of science owing to their distinctive properties such as high specific surface area, making these structures useful in surface-related applications [10–12]. These architectures also can act as light scattering center under light irradiation [13,14].

Light can be scattered and redirected in many directions. Particularly, when the size of the particles is comparable to the wavelength of the incident light, the Mie's scattering happens. In the atmosphere, the clouds appear white, attributing to the Mie's scattering effect, which can scatter all wavelength of the visible light by the various sized dusts. If we introduce the Mie's scattering phenomenon into the TiO_2 spheres, when the light collides with the TiO_2 sphere with size comparable to its wavelength, the light scatters strongly along the forward direction. This scattering produces a pattern like an antenna lobe, with a sharper and more intense forward lobe (Scheme 1a) [15]. Therefore, the path length of the incident light between the neighbored spheres will be increased [16], leading to a promoted light utilization efficiency over the TiO_2 spheres. The scattering phenomenon has been applied in the dye-sensitized solar cells (DSSC) before [17, 18].

Block copolymers are suitable and versatile templates for fabricating mesostructured and mesoporous materials. In particular, nonionic amphiphilic copolymers as surfactants can form a large variety of three-dimensional (3-D)

structures through non-covalent interactions, which can be used to direct the nanocrystals into the desired mesostructure [19]. They are also able to impart high effective surface areas, pore volumes, and size-controlled morphologies, as well as being industrially available, environmentally friendly, and easy to remove from the nanostructured framework [20]. To the best of our knowledge, there have been no reports of a simple and economical synthesis and characterization of size-controlled spherical mesoporous TiO_2 clusters with a high specific surface area, particularly using a self-assembled block copolymer as a structure-directing agent. Herein, we synthesized spherical mesoporous TiO_2 clusters in various sizes using a sing titanium precursor (titanium (IV) isopropoxide) and various amphiphilic triblock copolymers ($PEO_x - PPO_y - PEO_x$, where PEO is poly(ethylene oxide) and PPO is poly(propylene oxide)). The triblock copolymer is used as structure-directing and pore-forming agent and the interaction between the titanium precursor and the triblock copolymer self-assemblies in solvent leads to the assembly of TiO_2 nanoparticles into spherical aggregates with wormhole-like porous structures. The triblock copolymer micelle was composed of a core dominated by PO and a corona dominated by EO segments. The core of the micelles was believed to be free of water, while the swollen corona was hydrated. The aggregation behavior of the triblock copolymer under thermodynamic conditions may affect the TiO_2 cluster size and morphology. To study the chemical composition, morphology,

crystal information, and properties of the synthesized material, a variety of techniques is employed, including Fourier transform infrared spectroscopy, field-emission scanning electron microscopy, transmission electron microscopy, wide-angle X-ray diffraction, nitrogen (N_2) adsorption-desorption, dynamic light scattering, zata potential, and UV-vis spectroscopy. In addition, a reasonable model for the formation mechanism of these spherical clusters is proposed and discussed in more detail.

2.2 Experiments

2.2.1 Materials

Titanium (IV) isopropoxide (TTIP, $Ti(OPr^i)_4$), Pluronic P123 (P123, $EO_{20}PO_{70}EO_{20}$), Pluronic F127 (F127, $EO_{108}PO_{70}EO_{108}$), 2,4-pentanedione (acetylacetone, AcAc), sulfuric acid, nitric acid poly(ethylene glycol) (PEG, average MW = 10,000) and poly(ethylene oxide) (PEO, average MW = 100,000) were all purchased from Sigma-Aldrich and used as received without further purification.

2.2.2 Preparation of mesoporous TiO_2 spheres

The mesoporous TiO_2 spheres were synthesized with the sol-gel method by using triblock copolymer surfactants (P123 and F127 for sample S1 and S2, respectively) in aqueous solution. The general procedure was carried out as follows. First, 1.0 mmol of each surfactant was dissolved in 100 mL of deionized water, and the mixture was stirred vigorously at 50 °C to give a transparent solution. After the surfactant had dissolved sufficiently, 1.5 g of sulfuric acid was added to the aqueous surfactant solution. TTIP (7.84 g) was mixed with AcAc (2.76 g) in a separate beaker and dropped into the aqueous surfactant solution with vigorous stirring for 30 min at 50 °C. The resulting materials were treated hydrothermally at 90 °C for 10 h. To achieve dispersion

of the TiO_2 spheres (S1 and S2) in suspension, the TiO_2 spheres were hydrothermally treated with nitric acid (HNO_3). The procedure was carried out as follows. 4 mL of HNO_3 was added to 100 mL of the above suspension. This mixture was then vigorously stirred at 50 °C for 2 h. The suspension was transferred into an autoclave, sealed, and then maintained 200 °C. After a reaction time of 24 h the autoclave was cooled to room temperature. The HNO_3 treatment produced a milky suspension.

2.2.3 Characterization

The surface features and morphologies of the TiO_2 spheres were investigated by using field-emission scanning electron microscopy (FE-SEM, JEOL JSM-6330F) and high-resolution transmission electron microscopy (HR-TEM, JEOL JEM-2000 FX II). The crystallite structures of the TiO_2 spheres were investigated by analyzing the wide angle X-ray diffraction (XRD) patterns obtained with a MAC/Sci MXP 18XHF-22SRA diffractometer equipped with Cu Kα irradiation ($\lambda = 0.514$ nm) and a fixed power source (40 kV, 200 mA) at a step width of 0.02°. The crystallite sizes were calculated by using the Scherrer equation ($\Phi = K\lambda / \beta\cos\theta$), where Φ is the crystallite size, λ is 0.154 nm (the wavelength of the X-ray irradiation), K is usually assumed to be 0.89, β is the full width at half-maximum intensity (FWHM), and θ is the diffraction angle of the (101) peak for anatase ($2\theta = 25.3°$). Differential scanning calorimetry

(DSC) measurements were performed using a DSC200 F3 Maia system under flowing nitrogen with a heating rate of 5 °C min^{-1}. The specific surface areas and pore size distributions of the TiO_2 spheres were characterized by analyzing the N_2 adsorption and desorption isotherms obtained at 77 K with a Micrometrics ASAP 2000 equipment (Table 1). All the samples were degassed at 200 °C and 10^{-6} Torr for 10 h prior to these measurements. The surface areas were calculated with the Brunauer–Emmett–Teller (BET) equation, and pore-size distributions were determined from the adsorption and desorption branches by using the Barrett–Joyner–Halenda (BJH) formula. The average size and size distribution of the TiO_2 spheres were measured by dynamic light scattering (DLS), using a Photal DLS-7000 spectrophotometer equipped with a Photal GC-1000 digital autocorrelator (Otsuka Electronics Co., Ltd.). In this procedure, the wavelength (λ) of the argon laser was 488 nm, and the scattering angle was 90° with respect to the incident beam. Intensity-average and number-average particle size distributions were analyzed by the conventional CONTIN algorithm to estimate the diameter of the TiO_2 spheres. The zeta potential was measured by a zeta potential analyzer using ELS-8000 spectrophotometer (Otsuka Electronics Co., Ltd.) using Smoluchowski relationship. UV–visible spectroscopy was performed with a Lambda 25 instrument manufactured by Perkin Elmer.

2.3 Results and Discussion

2.3.1 Morphology and structure of mesoporous TiO_2 spheres

FE-SEM images of the mesoporous TiO_2 spheres (S1 and S2) after hydrothermal treatment with various surfactants are shown in Fig. 2.1(a) and (b) [21], respectively. The aggregates of these materials all have spherical morphologies. The spherical TiO_2 structures (S1 and S2) are highly monodispersed with sizes of ≈ 550 nm and ≈ 1000 nm, respectively. Even though a same precursor was used, the surface of TiO_2 spherical particles had a distinct toughness which is predicted to be caused by different surfactants. Both P123 and F127, consisting of a central hydrophilic PPO chain and two hydrophilic PEO tails, have been used as the structuredirecting agents for the construction of mesoporous structure for TiO_2. Both P123 and F127 are triblock copolymer and are constituted as EO–PO–EO. The two surfactants have the same length of 70 PO chains but P123's end groups have 20 while F127 have 108 EO chains. Therefore, compared to P123, F127 has a comparably hydrophilic EO chain forming a long micelle. It has been generally accepted that the nucleation takes place at the hydrophilic part of each surfactants, EO chain, when TiO_2 is formed from Ti precursor by sol-gel method. This implies that TiO_2 prepared with P123, the shorter EO-chain holder, has a coarser surface than that with F127, given that the longer EO chain, TiO_2 particles are

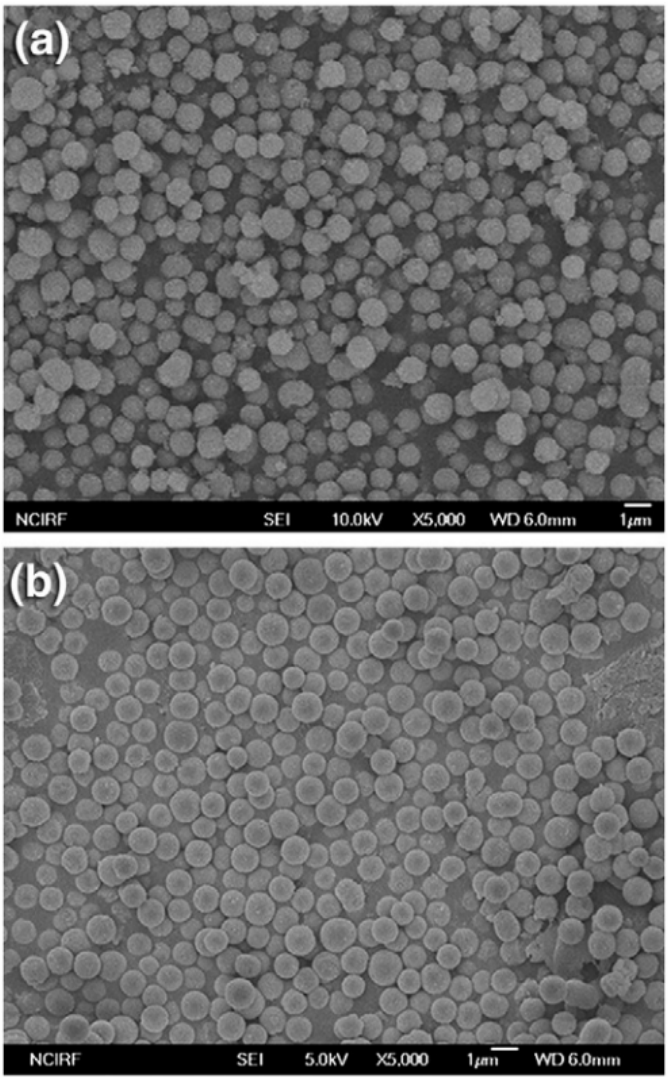

Fig. 2.1. FE-SEM images of (a) S1 and (b) S2.

easier to be agglomerated. As a result, the product particles prepared with F68 ($PEO_{75}PPO_{30}PEO_{75}$, Mw = 8,400), and F127 are smoother than those made with L121 ($PEO_5PPO_{70}PEO_5$, Mw = 4,400) and P123 which has a relatively shorter EO than the former ones. Due to this phenomenon, it can be confirmed that the surface of spherical particle in S1 was coarser that in S2 since the hydrophilic part of surfactant was influential for formation of the particle. In accordance with these results, the effect of EO on block copolymer based synthesis of spherical TiO_2 has been predicted. When symmetrical block copolymers are dissolved in water solution, a large number of spherical micelles are formed due to the interaction of the two segment types of the block copolymers. The block copolymer micelle was composed of a core dominated by PO and a corona dominated by EO segments. The core of the micelles was believed to be free of water, while the swollen corona was hydrated. The aggregation behavior of the block copolymer under thermodynamic conditions may affect the TiO_2 particle size and morphology. The TiO_2 spheres were synthesized with the sol-gel method from hydrolysis of a titanium precursor. Hydrolysis and condensation (nucleation and growth) of the titanium precursor lead to the formation of primary particles, which spontaneously aggregated to form the large spherical clusters in the solvent due to the strong surface tension. The driving force for aggregation of the primary particles is a decrease in the high surface energy of the tiny primary particles. It is known that the functional

groups of the surfactant have coordination bonds with the TiO_2 nanoparticles. In this system, surface hydroxyl groups in the surfactant coordinate with primary TiO_2 particles in the water. It is assumed that micelles surround the primary TiO_2 particles, playing an important role in the formation of TiO_2 aggregates. It appears that as the hydrophilic chain of EO becomes longer, the nucleation and growth of TiO_2 become easier and hence increase the size of TiO_2.

Typical HR-TEM images for the mesoporous TiO_2 spheres are shown in Fig. 2.2 [21] and reveal that the materials have well-defined spherical structures with primary particle sizes of ≈ 10 nm. All of the samples have mesoporous structures, and the wormhole-like mesopores form special closely interconnected nanoparticles. From these results, we conclude that the pore walls consist of aggregated TiO_2 nanoparticles. Fig. 2.3 (a) and (b) shows the XRD patterns for S1 and S2, respectively, which indicate that all of the particles possess highly crystallized anatase structures (JCPDS card no. 73-1764) without any impurity phases. The average crystallite sizes of S1 and S2, as determined from the (101) peak with an estimation based on the Scherrer formula, are 13 nm and 7 nm, respectively, which implies that the mesoporous spheres are composed of smaller nanocrystals. Fig. 2.4 (a) and (b) shows the DSC patterns of S1 and S2 before and after calcination at 500 °C, respectively. In all cases, below 200 °C, the weight loss is attributed to the loss of adsorbed

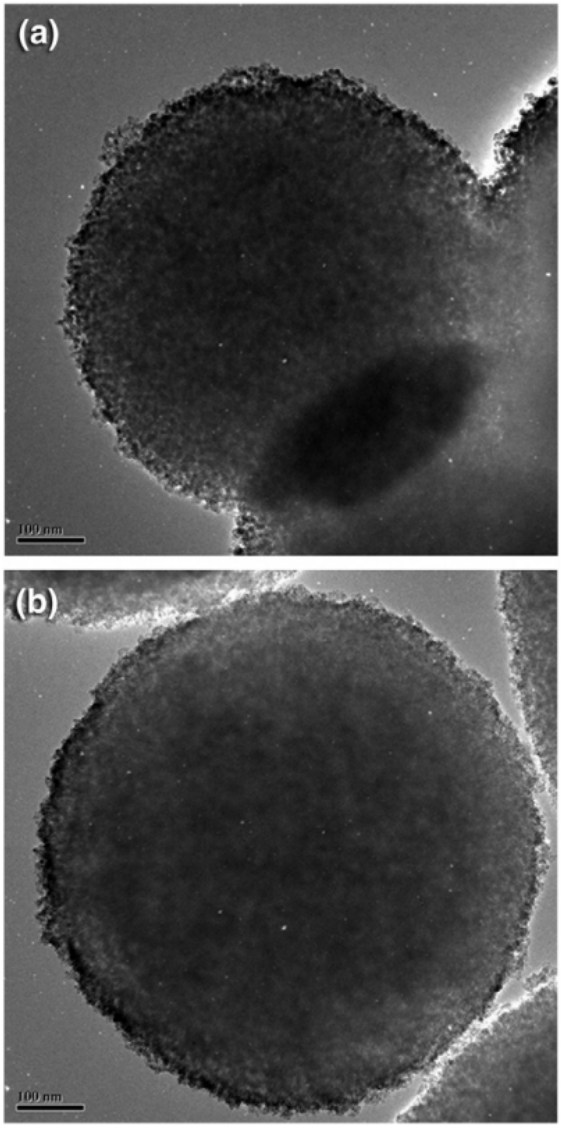

Fig. 2.2. Representative HR-TEM images of (a) S1 and (b) S2.

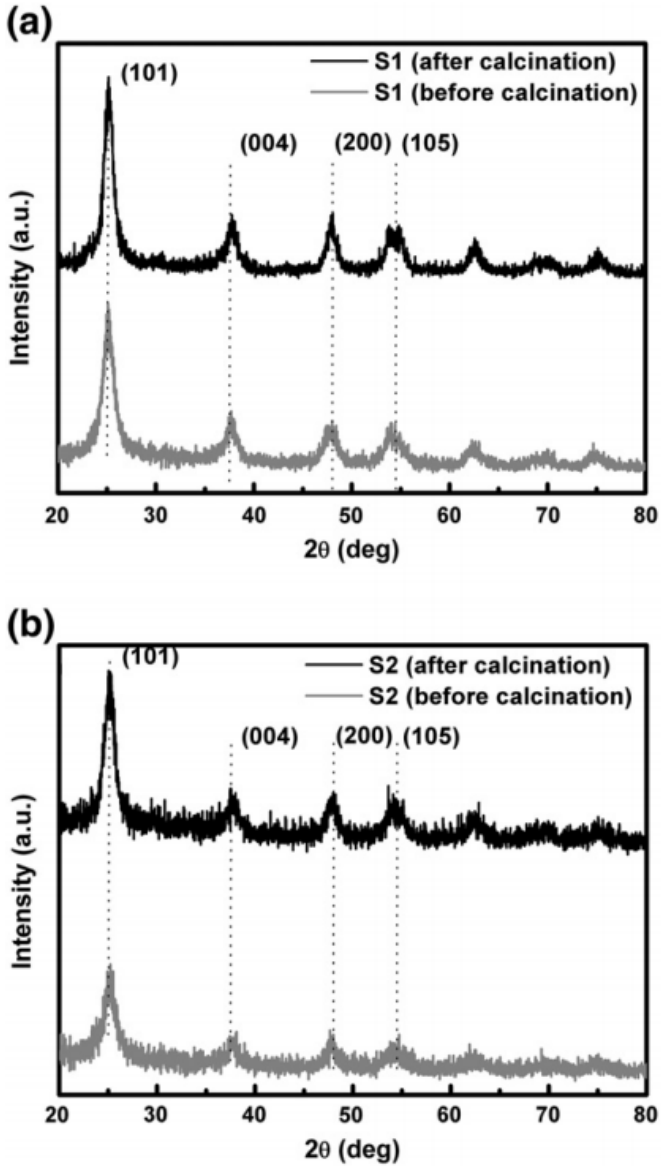

Fig. 2.3. X-ray diffraction patterns of (a) S1 and (b) S2 before and after calcination.

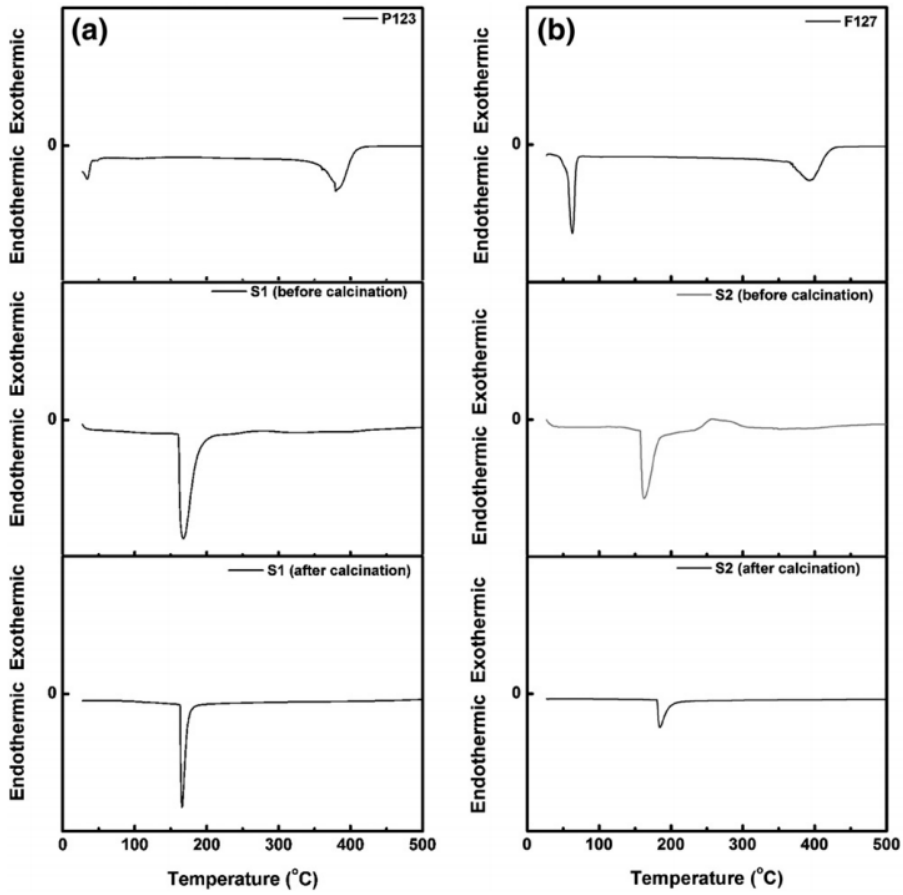

Fig. 2.4. DSC curces for (a) P123, S1 before and after calcination and (b) F127, S2 before and after calcination.

water and decomposition of organic residue on the surface of the powder. Due to the high surface area of TiO_2 sphere, even after calcination, the adsorption functions of water or residues were optimal. Therefore, the samples that have been calcinated and those that were not, showed a similar endothermic peak with regards to the loss of adsorbed water and decomposition of organic residues. For S1 (see Fig. 2.4 (a)), no characteristic exothermic peak was observed, which is attributed to the presence of TiO_2 anatase crystallites, since all the TiO_2 nanoparticles in the spheres crystallized during the hydrothermal treatment. In contrast, as shown in Fig. 2.4 (b), for S2, there is an exothermic crystallization peak at approximately 300 °C. It is known that the transformation from amorphous to anatase crystallites depends on intimate contact with OH^-. S2 contains large spheres, so there is less chance for the particles to come into contact with OH− during hydrothermal treatment, which results in a lesser degree of crystallization, as confirmed by the XRD result. It is known that the transformation from amorphous to nanocrystalline anatase is governed by interface nucleation and surface nucleation. Accordingly, the intensity of the exothermic crystallization peak of packed TiO_2 is lower than that of loose TiO_2. According to DSC analysis, the crystallization of amorphous TiO_2 to anatase crystallite usually occurs at approximately 440 °C, whereas crystallization in S2 occurs at approximately 300 °C through the self-assembling aggregation of spheres. The exothermic changes disappear from the

S2 pattern after calcination. The specific surface areas of S1, S2 and NC characterized by using nitrogen gas adsorption–desorption and are shown in Fig. 2.5 (a), (b) and (c), respectively. The physical characteristics are summarized in Table 2.1. The specific surface area of the NC is only 51.84 m^2g^{-1} and there are no obvious porous characteristic, which indicates that they are amorphous hybrid beads with a dense structure. All the isotherms of the S1 and S2 are of classical type IV with H2 hysteresis between the adsorption and desorption curves, which indicates the presence of an ink-bottle pore structure with a large cavity. The surface areas of S1 and S2 calcined at 500 °C were determined with the BET method and found to be similar, 223.76 and 192.06 m^2g^{-1}, respectively. The surface areas of S1 and S2 are 4.3 and 3.7 times respectively that of the TiO_2 nanoparticle, which clearly indicates that these spherical structures have high internal surface areas. The pore-size distributions of S1 and S2 estimated by employing the Barrett–Joyner–Halenda (BJH) method, as shown in Fig. 2.6 (a) and (b), respectively. As shown in Fig. 2.6 (a), the average pore size of S1 was 12.51 nm, a seemingly reasonable result considering the particle size. It was reported that the area occupied by the dye molecule on the TiO_2 surface was calculated to be 1.6 nm^2/molecule [22]. This result suggests that the surfaces inside the TiO_2 spheres can be readily accessed by the dye molecules. Conspicuously, two kinds of pores were observed in S1. The 12.51 nm sized pores are regarded as the internal pores, which were originated from the

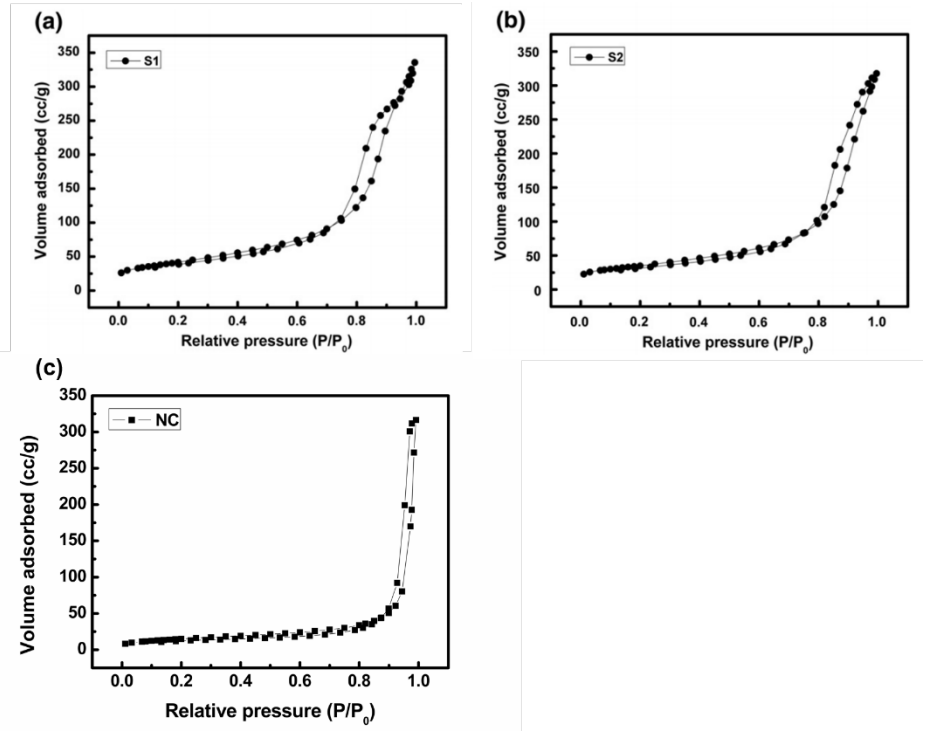

Fig. 2.5. N_2 adsorption-desorption isotherms for (a) S1, (b) S2, and (c) NC.

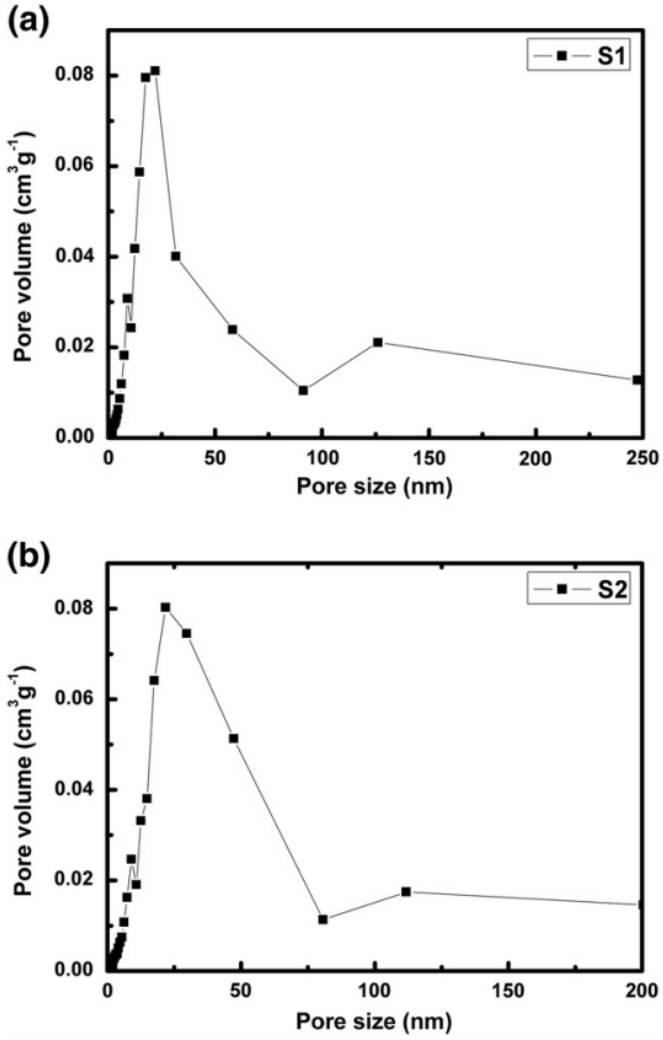

Fig. 2.6. BJH pore-size distributions for (a) S1 and (b) S2.

Table 2.1. Specific surface area and average pore size of S1 and S2.

Samples	Specific surface area (m^2/g)	Average pore size (nm)
S1	223.76	12.51
S2	192.06	16.06

surfactant, of the mesoporous TiO_2 spheres, whereas the 126.2 nm pores originated from the interstitial voids formed by packed spheres. Conversely, for S2 (Fig. 2.6 (b)), 16.06 nm and 111.8 nm sized pores were generated from S2.

2.3.2 Dispersibility of mesoporous TiO_2 spheres by acid treatment

Fig. 2.7 shows the average aggregate diameters of the mesoporous TiO_2 spheres in aqueous solution, as determined with DLS. DLS measures the Brownian motion of the particles and relates it to their size. The correlation functions were analyzed by means of the constrained regulation (CONTIN algorithm) method to determine the distribution decay rates. The average aggregate sizes of S1 and S2 are 2549.4 (average % error: 0.8) and 2149.0 nm (average % error: 2.2%), respectively. Although the FE-SEM images of these TiO_2 spheres show that they have submicrometer sizes, these spheres aggregated in aqueous solutions. Considerable aggregation was observed for both types of TiO_2 spheres, resulting in the formation of flocs. The aggregate sizes of these spheres are on the micrometer scale, presumably due to the hydrophobic nature of the TiO_2 spheres' surfaces and the electrostatic attraction of the spheres. Therefore, these TiO_2 spheres aggregate in solvents to sizes that reach even the micrometer scale. To improve TiO_2 sphere dispersion, acid treatment was tested. Acid treatment is an effective tool for dispersing TiO_2 spheres in aqueous solution without damaging their spherical structure. The aggregate sizes of S1 and S2 were

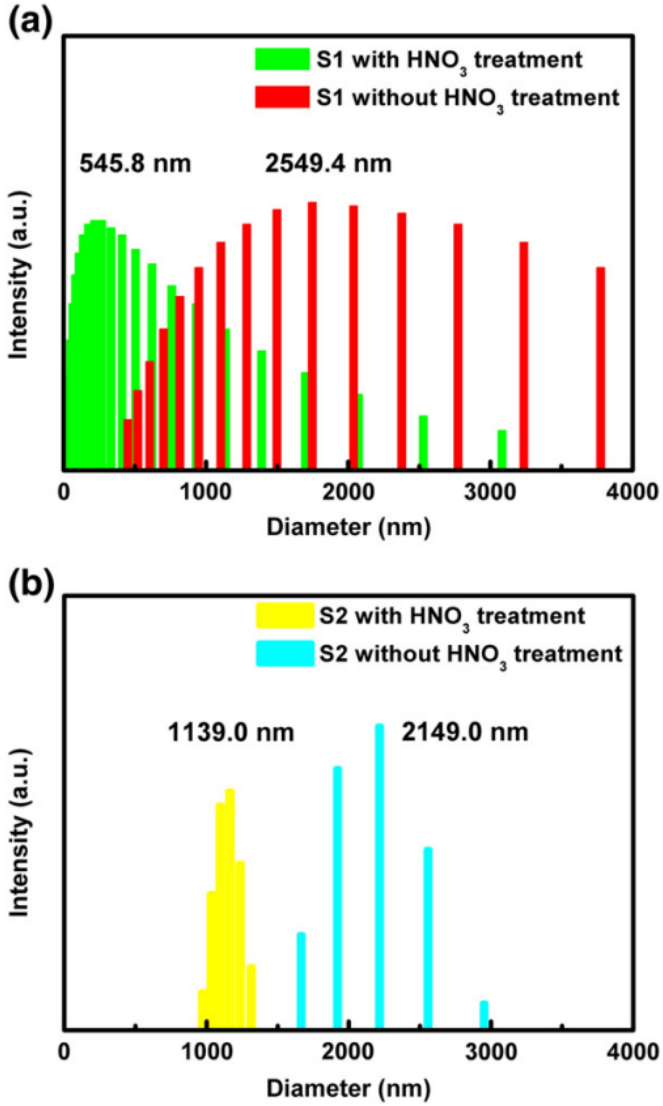

Fig. 2.7. DLS histograms showing (a) S1 and (b) S2 with and without acid treatment.

reduced by treatment with HNO_3 to 545.8 (average % error: 0.5) and 1139.0 (average % error: 0.4) nm, respectively, which is in good agreement with the FE-SEM results. Thus the spheres are well-dispersed in the suspension. The spheres maintained their morphologies after dispersion of TiO_2 in the solvent, because no physical pressure was applied during the HNO_3 treatment. So any destruction of morphology was minimized. Fig. 2.8 shows the zeta-potential values of S1 with and without acid treatment. The zeta potential (ζ) of a suspension is a function of surface charge. In a dispersion where ζ is close to zero (the isoelectric point), particles in the suspensions tend to agglomerate. At highly positive or negative ζ (|ζ| > 30 mV), particles in suspensions tend to repel each other and therefore do not agglomerate. After treating with HNO_3, when looking at the zeta potential value of TiO_2 sphere, it can be found that the HNO3 treated TiO_2 spheres had a high zetapotential value in the pH domain, which indicates that the HNO_3 treatment within the solvent of TiO_2 sphere prevents aggregation between spheres. Particularly, when the pH level is not adjusted, the TiO_2 sphere that has not been treated with HNO_3, resulted in a pH value of 4 in the water. The zeta-potential of the TiO_2 spheres before acid treatment is approximately −5 mV at pH 4, which is in the range of strong agglomeration (|ζ| b 5 mV). However, after being treated with HNO_3, the pH value of TiO_2 in water was 3, while the zeta-potential value was approximately −15 mV, which means that the acid treatment increases the steric repulsion between the TiO_2

spheres, showing that TiO_2 spheres treated with HNO_3 become moderately dispersed in water. Through this, dispersed TiO_2 spheres could be made into TiO_2 paste.

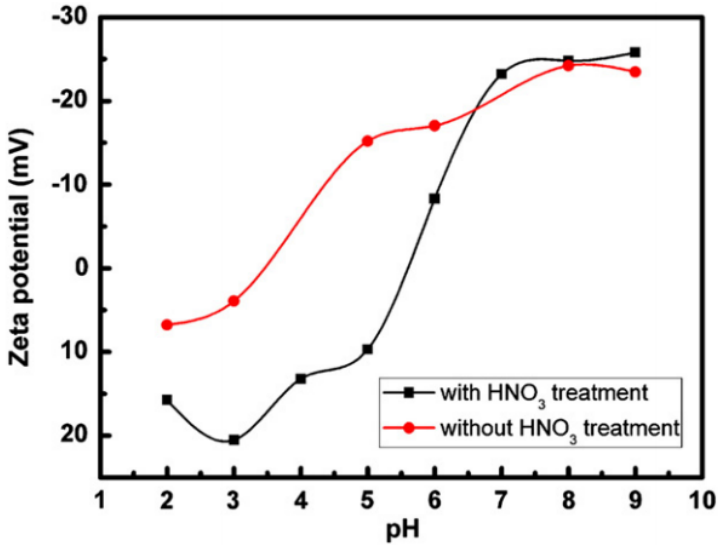

Fig. 2.8. Zeta-potential values for S1 with and without acid treatment as a function of pH.

2.4. Summary

In this study, a direct triblock-copolymer templating approach is demonstrated for the successful synthesis of size-controlled spherical mesoporous TiO_2. The triblock copolymer is the determining factor in the morphology and the size of the resulting materials, and the individual TiO_2 nanocrystals (about 5 nm in size) have a strong tendency to self-assemble during synthesis into spherical aggregates (about 500 − 1000 nm in diameter) with a disordered wormhole-like mesopore structure. This process is spontaneous. Extensive characterization of the resulting material confirmed that these particles possess a uniform 3-D spherical morphology, high specific surface area (~ 223.76 m^2g^{-1}), narrow particle-size distribution, and high dispersity.

.

References

1. A. Fujishima, K. Honda, Nature (London) 238 (1972) 37–38.
2. B. O'Regan, M. Grätzel, Nature 353 (1991) 737–740.
3. M. Wagemaker, A.P.M. Kentgens, F.M. Mulder, Nature 418 (2002) 397–399.
4. N.-L. Wu, S.-Y. Wang, L.A. Rusakova, Science 285 (1999) 1375–1377.
5. S.H. Kang, S.-H. Choi, M.-S. Kang, J.-Y. Kim, H.-S. Kim, T. Hyoen, Y.-E. Sung, Adv. Mater. 20 (2008) 54–58
6. H.-E. Wang, Z. Chen, Y.H. Leung, C. Luan, C. Liu, Y. Tang, C. Yan, W. Zhang, J.A. Zpien, L. Bello, S.-T. Lee, Appl. Phys. Lett. 96 (2010) 263104-1–263104-3.
7. H.-J. Kim, J.-D. Jeon, S.-Y. Kwak, Powder Technol. 243 (2013) 130–138.
8. H.-J. Koo, Y.J. Kim, Y.H. Lee, W.I. Lee, K. Kim, N.-G. Park, Adv. Mater. 20 (2008) 195–199.
9. J. Xi, Q. Zhang, S. Xie, S. Yodyingyong, K. Park, Y. Sun, J. Li, G. Cao, Nanosci. Nanotechnol. Lett. 3 (2011) 690–696.
10. X. He, D. Antonelli, Angew. Chem. Int. Ed. 41 (2002) 214–229.
11. M.H. Keefe, R.V. Slone, J.T. Hupp, K.F. Czaplewski, R.Q. Snurr, C.L. Stem, Langmuir 16 (2000) 3964–3970.
12. B. Zornoza, S. Irusta, C. Téllez, J. Coronas, Langmuir 25 (2009) 5903–5909.
13. D. Chen, F. Huang, Y.-B. Cheng, R.A. Caruso, Adv. Mater. 21 (2009) 2206–2210
14. F. Sauvage, D. Chen, P. Comte, F. Huang, L.-P. Heiniger, Y.-B. Cheng, R.-A. Caruso, M. Grätzel, ACS Nano 4 (2010) 4420–4425..
15. G. Mie, Ann. Phys. 330 (1908) 377−445.
16. H. J. Koo, J. Park, B. Yoo, K. Yoo, K. Kim, N. G. Park, Inorg. Chim. Acta 361 (2008) 677−683.

17. X. Wu, G. Q. Lu, L. Z. Wang, Energy Environ. Sci. 4 (2011) 3565−3572.
18. I. G. Yu, Y. J. Kim, H. J. Kim, C. Lee, W. I. Lee, J. Mater. Chem. 21 (2011) 532−538.
19. H. Wang, J.−J. Miao, J.−M. Zhu, H.-M. Ma, J.−J. Zhu and H.−Y. Chen, Langmuir 20 (2004) 11738.
20. N. Negishi, S. Matsuzawa, K. Takeuchi and P. Pichat, Chem. Mater. 19 (2007) 3808.
21. H. –J. Kim, J. –D. Jeon, S. –Y. Kwak, Powder Technol. 243 (2013) 130–138.
21. A. Hagfeldt, M. Grätzel, Pure Appl. Chem. 73 (2001) 459–467.

Chapter 3

Amplified Visible Light Photocatalytic Activity of Mesoporous TiO_2/ZnPc Hybrid by Cascade Mie Light Scattering

3.1 Introduction

Environmental pollutants in water and air pose a serious threat to the public health and safety, and much effort has been directed toward solving these problems. From the point of green technology, photosensitive semiconducting materials are promising to be environmentally friendly and economically practicable catalysts, due to their nontoxicity and low cost [1−3]. As the best known photocatalyst, TiO_2 has attracted more attention and interest of many researchers due to its exceptional properties, such as high refractive index and ultraviolet (UV) absorption, excellent incident photoelectric conversion efficiency and dielectric constant, good photocatalytic activity, photostability, chemical stability, and long-time corrosion resistance as well as nontoxicity [4–9]. Unfortunately, pure TiO_2 can only be excited under ultraviolet (UV) irradiation, owing to its wide band gap (e.g. 3.2 eV for anatase and 3.0 eV for rutile), and thereby no visible light response is obtained [10, 11]. Such a photosensitive characteristic of pure TiO_2 is quite ineffective, because UV

radiation accounts for less than 5% of all natural sunlight and c.a. 43% of solar spectral energy is contained in the visible light. To improve the utilization of solar light in practical photocatalytic applications, the development of TiO_2 photocatalysts responsive to visible light is highly desirable. Many strategies have been developed to extend the absorption spectra of TiO_2 to the visible light region, including doping with non-metal elements [12−16], loading with noble metals [17−23], dye sensitization [24−26], and combining TiO_2 with other semiconductors [27−29]. Among them, a dye photosensitization is one of the most effective ways to extend the photoresponse of TiO_2 into the visible light region [24–26]. Indeed, this type of reaction has been exploited in the dye sensitized solar cells [30−33]. Zinc phthalocyanine (ZnPc) is highly stable metal complex acting as a visible light absorption dye [34−40], and has potential application in optical switching [41], solar cell [42], and photocatalyst [35]. It is known that the incorporation of zinc phthalocyanine in a TiO_2 can effectively extend the absorption spectra of TiO_2 into the visible light region. In general, dye sensitization of TiO_2 photocatalytic cycle consists of four steps: (i) photo sensitization of TiO_2 proceeded by the initial excitation of the dye; (ii) electron injection into the TiO_2 conduction band; (iii) migration of excited electrons to the surface of TiO_2; (iv) reaction of excited electrons with the adsorbed electron acceptors. Since the first step for the photocatalysis is a light

excitation process, an efficient utilization of the incident light is an effective way to improve photocatalytic activity. Particularly, when the size of the particles is similar to the wavelength of the incident light, the Mie scattering occurs. Such a comparable size of particles can promote light scattering, resulting in the improvement of light utilization and further enhancement of photocatalytic activity [43−47]. Indeed, Mie scattering effect has been applied in the dye-sensitized solar cells previously. However, there are few studies that observed the light scattering effect on dye sensitized TiO_2 for the application of photocatalyst to solve the environmental problems. Here, we prepared the spherical TiO_2 with the mesoporous framework to increase the specific surface area and to improve the incorporation efficiency of ZnPc, which can further enhance the visible light photocatalytic activity. The mesoporous TiO_2/ZnPc hybrids were synthesized with the varied size to investigate the effect of Mie scattering on the photocatalytic activity of TiO_2/ZnPc hybrid. We showed that the scattering efficiency of the incident visible light is dependent on the diameter of ZnPc-incorporated mesoporous TiO_2 spheres. When the size of TiO_2/ZnPc hybrid was comparable to the wavelength of incident visible light, the mesoporous TiO_2/ZnPc exhibited the highest photocatalytic decomposition activity due to the cascade Mie scattering effect. The enhanced photocatalytic activity of mesoporous TiO_2/ZnPc by Mie scattering makes it tremendously attractive for applications ranging from water purification to hydrogen

generation. In addition, the simplicity of the current process to produce mesoporous TiO_2/ZnPc makes it attractive for large-scale production.

3.2 Experiments

3.2.1 Materials

Titanium (IV) isopropoxide (TTIP, $Ti(OPr^i)4$), Pluronic L121 (L121, $EO_5PO_{70}EO_5$), Pluronic P123 (P123, $EO_{20}PO_{70}EO_{20}$), Pluronic F68 (F68, $EO_{75}PO_{30}EO_{75}$), Pluronic F127 (F127, $EO_{108}PO_{70}EO_{108}$), 2,4-pentanedione (acetylacetone, AcAc), sulfuric acid, dimethyl sulfoxide, zinc phthalocyanine (ZnPc), poly(ethylene glycol) (PEG, average MW = 10,000), and poly(ethylene oxide) (PEO, average MW = 100,000) were purchased from Sigma-Aldrich. They were used in the received form without further purification. Water used in all syntheses was distilled and deionized.

3.2.2 Preparation of ZnPc incorporated TiO_2 spheres

The TiO_2 spheres were synthesized with solegel method by using triblock copolymer surfactants (L121, P123, F68, and F127 for samples L121−TiO_2, P123−TiO_2, F68−TiO_2, and F127−TiO_2, respectively) in aqueous solution. The general procedure was as follows. First, 1.0 mmol of the surfactant was dissolved in 100 mL of deionized water. The mixture (pH 7.09) was stirred vigorously at 50 ^oC to produce a transparent solution. After the surfactant was dissolved sufficiently, 1.5 g of sulfuric acid was added to the aqueous surfactant solution (pH 0.76). TTIP (7.84 g) was mixed with AcAc (2.76 g) in a separate

beaker and dropped into the aqueous surfactant solution (pH 0.89) with vigorous stirring for 1 h at 50 °C. Light yellow powders formed within several minutes. The resulting materials were treated hydrothermally at 90 °C for 12 h. The solids in the solutions were filtered out, dried in air, and ground to fine powders. To remove the organic residue including surfactants and increase crystallinity of TiO_2, the materials were calcined at 500 °C at a rate of 1 °C/min in air. ZnPc incorporated TiO_2 (TiO_2/ZnPc) was prepared according to the previous procedure [48]. To prepare TiO_2/ZnPc, ZnPc (12 mmol) was dissolved in dimethyl sulfoxide (30 mL). A TiO_2 sample (one of L121−TiO_2, P123−TiO_2, F68−TiO_2, or F127–TiO_2, 2 g) was added to this solution. The resulting suspensions were magnetically stirred at room temperature for 10 h. The catalysts were collected by removing solvent under vacuum and were dried at 60 °C for 12 h. The products were denoted L121−TiO_2/ZnPc, P123−TiO_2/ZnPc, F68−TiO_2/ZnPc, or F127−TiO_2/ZnPc, respectively.

3.2.3 Preparation of TiO_2/ZnPc films

The TiO_2/ZnPc films used for photocatalytic test were prepared via a doctor-blade method. The weight content of the TiO_2/ZnPc spheres in the water-based suspension was 40 wt%. The pastes were prepared by admixing the 10 g of suspension with 0.12 g of PEG and 0.12 g of PEO. The resulting pastes were

doctor-bladed onto glass slides. In order to further improve the connectivity among TiO_2/ZnPc spheres, the coated films were then pressed. The typical pressure was at 12 MPa with plates preheated to 120 ^oC for 10 min. Teflon plates were inserted between the films and the plate, to prevent the films from sticking to the plate. The films were then heated at 170 ^oC for 30 min in air. The thickness of the films were measured using an α-step profiler. The thicknesses of the films were in the 17.2−17.7 mm range and were uniform (the largest variation being approximately 0.2 mm for all samples).

3.2.4 Characterizations

Fourier-transform infrared (FTeIR) spectra of the samples pelletized with KBr powder were collected over the range of 4000 to 400 cm^{-1} with a spectral resolution of 4 cm^{-1} by using a Thermo Scientific Nicolet iS10 IR spectrophotometer. The X-ray diffraction patterns of the nanoparticles in the TiO_2/ZnPc spheres were collected at room temperature, by using a MAC/Sci MXP 18XHF- 22SRA diffractometer equipped with graphite-monochromatized Cu Ka radiation (λ= 1.541Å, 50 kV, and 100 mA) as the X-ray source. Data acquisition was performed over the 2θ angular range 20−80 with a scanning speed of 5^o/min. XPS was performed on a Kratos AXIS photoelectron spectrometer, with a background pressure of approximately 1 ×

109 Torr, by using Mg Kα X-rays as the excitation source (1253.6 eV). All binding energies were calibrated by assuming that the binding energy of the C 1s peak at 284.6 eV. The morphologies of the materials were examined using a JEOL JSM-6330F FE-SEM under an applied voltage of 3.0 kV. The average particle sizes of the TiO_2/ZnPc spheres were determined using a DLS method with a Photal DLS-7000 spectrophotometer equipped with a Photal GC-1000 digital autocorrelator (Otsuka Electronics Co., Ltd.). In this procedure, the wavelength (λ) of the argon laser was 488 nm. The scattering angle was 90^o with respect to the incident beam. All samples were finely ground and dispersed in deionized water. The intensity-average and number-average particle size distributions were analyzed by using the conventional CONTIN algorithm to estimate the diameters of the particles. The specific surface areas and pore size distributions of the materials were characterized by analyzing the N_2 adsorption and desorption isotherms obtained at 77 K with a Micromeritics ASAP 2000. All samples were degassed at 200 ^oC and 106 Torr for 10 h prior to measurements. The surface areas were calculated with the BrunauereEmmetteTeller (BET) equation. Pore-size distributions were determined from the adsorption and desorption branches, by using the BarretteJoynereHalenda (BJH) formula. The specific surface areas and average pore sizes of the samples were calculated with Micromeritics Density Functional Theory (DFT) Plus software package.

3.2.4 Photocatalytic performance under visible light irradiation

The photocatalytic activity of each sample was evaluated by determining its ability to decompose methylene blue (MB) (Sigma Aldrich), a model contaminant, under visible light irradiation. Experiments were conducted at ambient temperature as follows. Each sample was added into 100 mL of MB solution (20 mg/L) in a quartz vessel. Prior to illumination, the sample in the vessel was stirred for 1 h in the dark, until adsorption−desorption equilibrium was reached. The sample was then irradiated under visible light with continuous magnetic stirring. A commercial 400 W halogen spotlight (the spectrum below 400 nm was removed with a cut-off filter) was used for visible light illumination. The light source was positioned at 15 cm from the reaction solution. The degradation of the MB aqueous solution was monitored spectrophotometrically at λ_{max} = 664 nm. Average values were obtained from three separate runs. UV−visible spectroscopy was performed with a Lambda 25 UV/Vis spectrophotometer (PerkinElmer). Diffused reflectance spectra of the TiO_2 sphere was collected from a Cary 5000 UV−Vis−NIR spectrophotometer with an integrating sphere accessory (Internal DRA-2500).

3.3 Results and Discussion

3.3.1 Synthesis of TiO_2/ZnPc hybrids

The XRD patterns of the synthesized photocatalysts, L121-TiO_2/ZnPc, P123-TiO_2/ZnPc, F68-TiO_2/ZnPc, and F127-TiO_2/ZnPc, are shown in Fig. 3.1 (a)–(d). All TiO_2/ZnPc samples showed several well-defined reflection peaks corresponding to the anatase crystal phase (JCPDS card No. 73-1764). It is known that photocatalytic activity is associated with crystallinity of photocatalyst. [49, 50] Thus, we evaluated the average crystallite sizes for L121-TiO_2/ZnPc, P123-TiO_2/ZnPc, F68-TiO_2/ZnPc, and F127-TiO_2/ZnPc using Scherrer formula based on the (101) peak. The crystal sizes of all TiO_2/ZnPC samples were indistinguishable (L121-TiO_2/ZnPc = 8.19 nm, P123-TiO_2/ZnPc = 7.87 nm, F68-TiO_2/ZnPc = 7.42 nm, and F127-TiO_2/ZnPc= 7.28 nm), which indicated that they had similar crystal growth. Therefore, the effect of the crystallinity on the photocatalytic activity could be ignored.

The FT-IR spectra were used to verify the presence of ZnPc in the TiO_2. As shown in Fig. 3.2, a broad absorption band associated with the stretching modes of the amine (N–H) group of ZnPc was observed over the range of 2500–3700 cm^{-1}. N-H bending mode of ZnPc was also observed at 1644 cm^{-1}. Absorption peaks at around 1483 cm^{-1} and 730 cm^{-1} were assigned to C–H in-plane bending

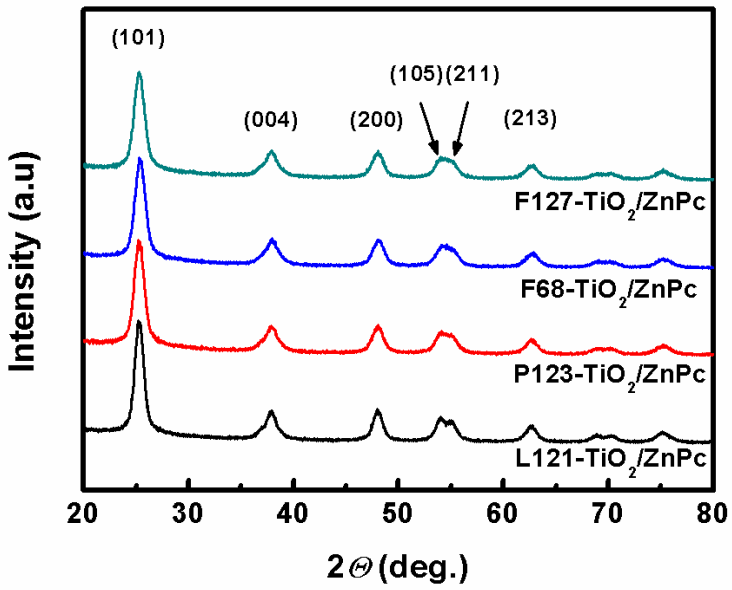

Fig. 3.1. XRD patterns of the synthesized photocatalysts, L121-TiO_2/ZnPc, P123-TiO_2/ZnPc, F68-TiO_2/ZnPc, and F127-TiO_2/ZnPc.

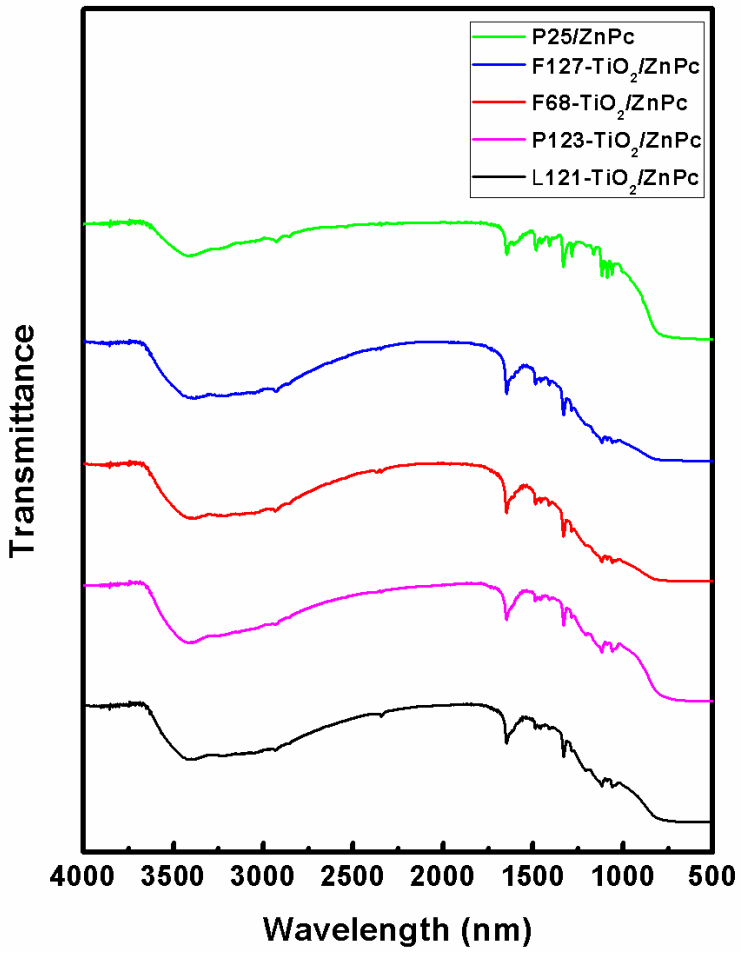

Fig. 3.2. FT-IR spectra of L121-TiO_2/ZnPc, P123-TiO_2/ZnPc, F68-TiO_2/ZnPc, and F127-TiO_2/ZnPc.

vibrations and C–H out-of-plane bending vibrations of ZnPc molecule, respectively. Furthermore, many intense and sharp bands corresponding to C–N stretch modes and C=C stretch modes of ZnPc were observed within the range of 1060–1329 cm^{-1}. The characteristic vibrations of the inorganic Ti–O–Ti network in titanium dioxide could be seen in the spectra below 950 cm^{-1}. We note that XRD peaks corresponding to ZnPc were not observed. Thus, it was thought that ZnPc molecules were well adsorbed and dispersed on the surface of the TiO_2, instead of being aggregates.

XPS was also used to confirm the introduction of ZnPc in the TiO_2. Fig. 3.3 and table 3.1 show several regions of the XPS spectra of the P123-TiO_2/ZnPc samples. The wide survey scans in Fig. 3. 3 (a) demonstrate the presence of titanium (Ti 2p), oxygen (O 1s), carbon (C 1s), nitrogen (N 1s), and zinc (Zn 2p) in the P123-TiO_2/ZnPc samples. The Ti 2p spectrum contains two peaks at 464.3 eV and 458.5 eV (with a spin energy separation of 5.8 eV due to the spin-orbit coupling), which are corresponding to $2p_{3/2}$ and $2p_{1/2}$ spin-orbital components, respectively. The oxygen 1s feature contains two peaks at 530.5 eV and 532.3 eV, which are corresponding to the oxygen in Ti-O groups and the oxygen in OH groups of ZnPc, respectively. XPS analysis of the C 1s spectrum revealed that the ZnPc molecules on the TiO_2, which peak at 284.50

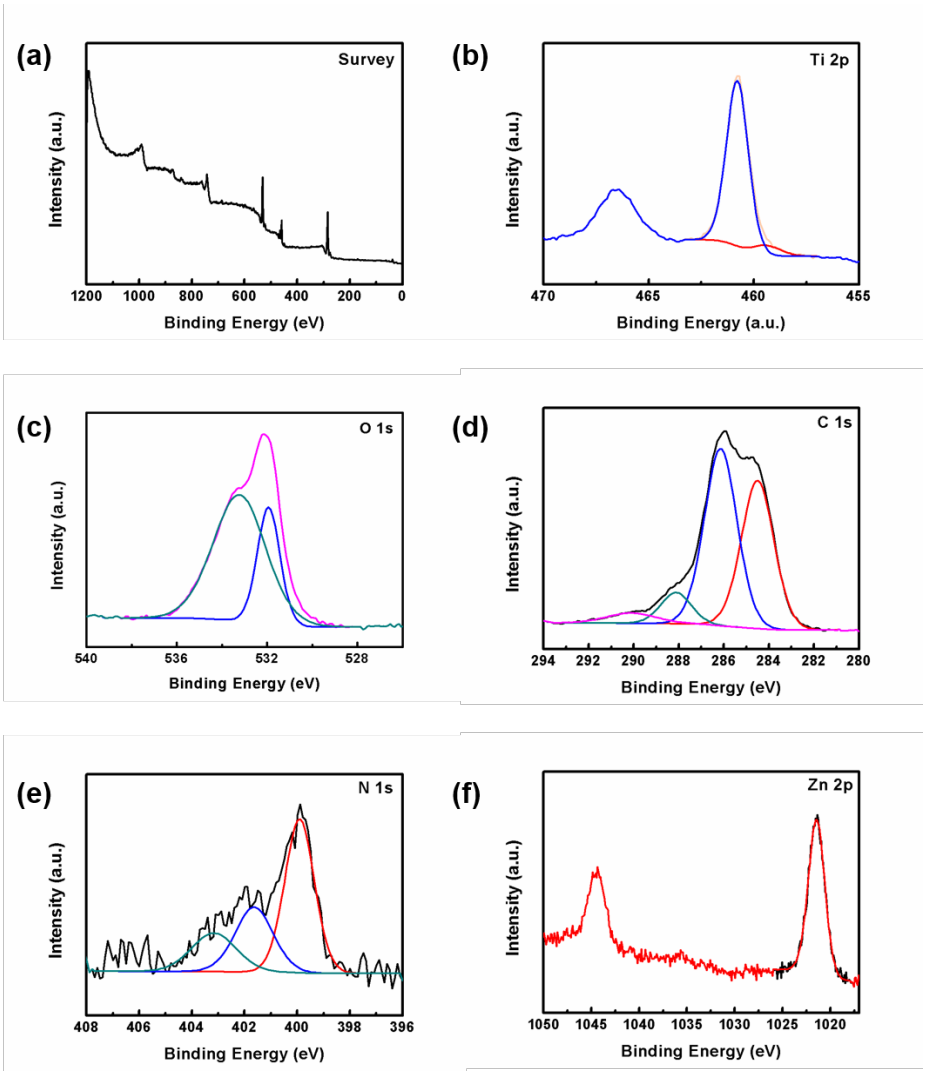

Fig. 3.3. XPS spectra of the P123-TiO_2/ZnPc samples; (a): survey, (b): Ti, (c): O, (d): C, (e): N, (f): Zn.

Table 3.1. XPS peaks for P123-TiO_2/ZnPc.

Binding energy (eV)				
Ti 2p	O 1s	C 1s	N 1s	Zn 2p
464.3	530.5	284.50	399.76	1021.43
458.5	532.3	288.12	401.47	1044.35
		290.10		

eV, 288.12 eV, and 290.10 eV, were attributed to the C=C bond with sp^2 orbital, sp^2 C-N, and sp^3 C-N, respectively. The high-resolution N 1s spectrum is shown in Fig. 3.3 (e). A broad peak between 398 eV and 404 eV could be deconvoluted into two peaks as follows: pyridinic nitrogen (C–N=C) signal appearing at 399.76 eV and another peak at 401.47 eV of the Zn–N bond. The Zn 2p spectrum has two peaks at 1021.43 eV and 1044.35 eV (with a spin energy separation of 22.92 eV due to the spin-orbit coupling), which are corresponding to $2p_{3/2}$ and $2p_{1/2}$ spin-orbital components, respectively. From these results, we also confirmed that the ZnPc molecules were successfully incorporated into the TiO_2.

3.3.2 Morphology of TiO_2/ZnPc hybrids

The size and morphology of the TiO_2/ZnPc hybrods (L121-TiO_2/ZnPc, P123-TiO_2/ZnPc, F68-TiO_2/ZnPc, and F127-TiO_2/ZnPc) can be observed by FE-SEM images (Fig. 3.4 (a)–(d) [51], respectively). FE-SEM exhibited that uniformly monodisperse spherical TiO_2/ZnPc hybrids were well produced by using a hydrothermal self-assembly process. In addition, FE-SEM showed that the TiO_2/ZnPc hybrids were formed by the agglomeration (or cluster) of the tiny primary TiO_2 particles of size within several nanometers (see insets of Fig. 3.4). Interestingly, we found that the diameters of the spherical TiO_2/ZnPc

hybrids were significantly increased as the ethylene oxide chain length of the triblock copolymer surfactant increased. When the numbers of ethylene oxide units in the surfactants were 5, 20, 75, and 108, the average diameters of the TiO_2/ZnPc hybrids were approximately 250 nm, 550 nm, 800 nm, and 1200 nm, respectively. The shape of the TiO_2/ZnPc hybrids became more spherical as the surfactant chain became longer. We quantitatively measured the particle sizes of the TiO_2/ZnPc hybrids using DLS measurement. The measured average sizes and size distributions of L121-TiO_2/ZnPc, P123-TiO_2/ZnPc, F68-TiO_2/ZnPc, and F127-TiO_2/ZnPc are shown in Figures 3.5 (a)–(d). The average particle sizes of L121-TiO_2/ZnPc, P123-TiO_2/ZnPc, F68-TiO_2/ZnPc, and F127-TiO_2/ZnPc were 245, 548, 798, and 1188 nm, respectively, which were in good agreement with the FE-SEM results.

3.3.3 Structure of TiO_2/ZnPc hybrids

The BET specific surface areas and pore-size distributions of L121-TiO_2, P123-TiO_2, F68-TiO_2, F127-TiO_2, and P25, before and after the incorporation of ZnPc (L121-TiO_2/ZnPc, P123-TiO_2/ZnPc, F68-TiO_2/ZnPc, F127-TiO_2/ZnPc, and P25/ZnPc), were evaluated from their respective nitrogen adsorption-desorption isotherms (Fig. 3.6 and table 2). In contrast to P25, L121-TiO_2, P123-TiO_2, F68-TiO_2, and F127-TiO_2 showed the specific hysteresis loops

between the adsorption and desorption isotherms over a P/P_0 range of approximately 0.5–0.8, which can be classified as a type IV isotherms with H2-type hysteresis. This revealed that these materials had a mesoporous structure. The BET specific surface areas of L121-TiO_2, P123-TiO_2, F68-TiO_2, F127-TiO_2, and P25 were 254.23 m^2/g, 236.19 m^2/g, 229.85 m^2/g, 223.83 m^2/g, and 56.42 m^2/g, respectively. All samples exhibited surface areas of at least 4 times greater than P25, although the specific surface areas of the samples decreased slightly as the sphere size increased. After incorporation of ZnPc, however, the specific surface areas of the TiO_2/ZnPc hybrids (L121-TiO_2/ZnPc, P123-TiO_2/ZnPc, F68-TiO_2/ZnPc, F127-TiO_2/ZnPc, and P25/ZnPc) decreased slightly (228.87 m^2/g, 223.76 m^2/g, 211.49 m^2/g, 192.06 m^2/g, and 49.02 m^2/g, respectively). In addition, their hysteresis loops were considerably reduced. These suggest that the ZnPc molecules were well adsorbed at the surface of the TiO_2/ZnPc hybrids. Nevertheless, the TiO_2/ZnPc hybrids showed the isotherms with a certain hysteresis loop. Thus, it was thought that the TiO_2/ZnPc hybrids still had a mesoporous structure, which can provide the hybrids with an excellent photocatalytic activity. The pore size distributions were evaluated by BJH method (Fig. 3.7, and table 3.2). The average pore sizes of the L121-TiO_2, P123-TiO_2, F68-TiO_2, and F127-TiO_2 were 4.2 nm, 5.7 nm, 5.9 nm, and 6.1 nm, respectively, with narrow pore size distribution. However, P25 did not show a clear pore structure. After incorporation of ZnPc, the average pore sizes of the

TiO_2/ZnPc hybrids (L121-TiO_2/ZnPc, P123-TiO_2/ZnPc, F68-TiO_2/ZnPc, F127-TiO_2/ZnPc, and P25/ZnPc) were slightly decreased (3.7 nm, 3.9 nm, 3.6 nm, 3.8 nm, and 4.3 nm), indicating the successful incorporation of ZnPc onto the surface of TiO_2. The mesoporous structure observed in the TiO_2/ZnPc hybrids was anticipated to create the large internal surface area that can provide a high number of active adsorption sites and act as a photocatalytic reaction center.

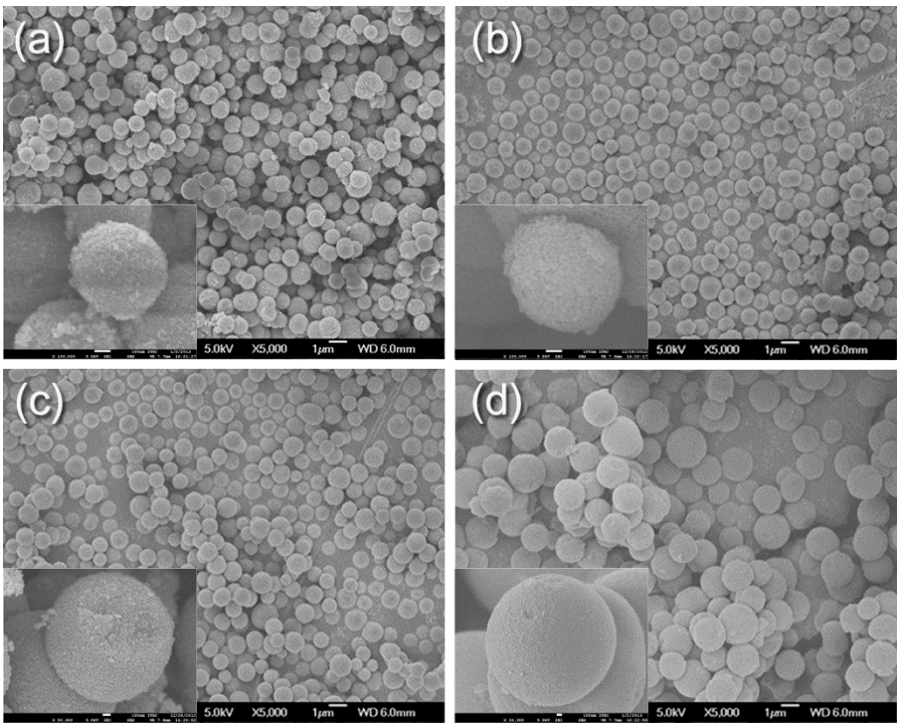

Fig. 3.4. FE-SEM images of (a) L121-TiO_2/ZnPc, (b) P123-TiO_2/ZnPc, (c) F68-TiO_2/ZnPc, and (d) F127-TiO_2/ZnPc.

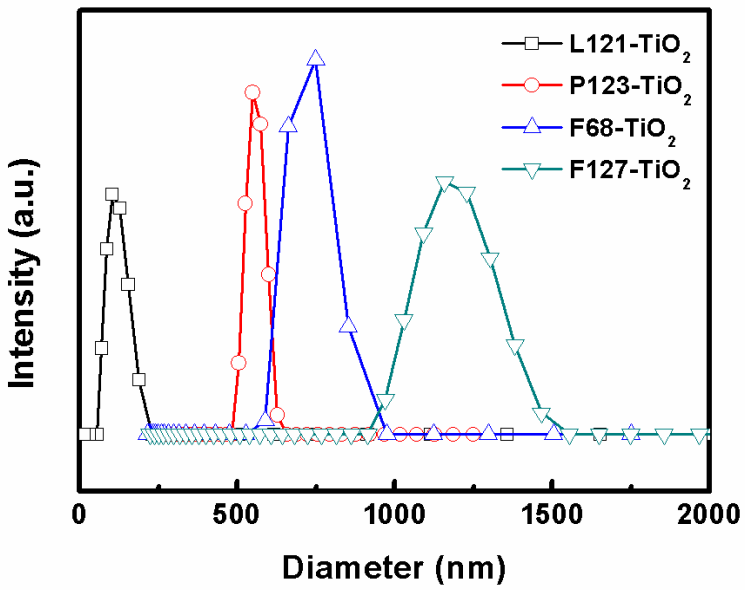

Fig. 3.5. DLS spectra of L121-TiO_2/ZnPc, P123-TiO_2/ZnPc, F68-TiO_2/ZnPc, and F127-TiO_2/ZnPc.

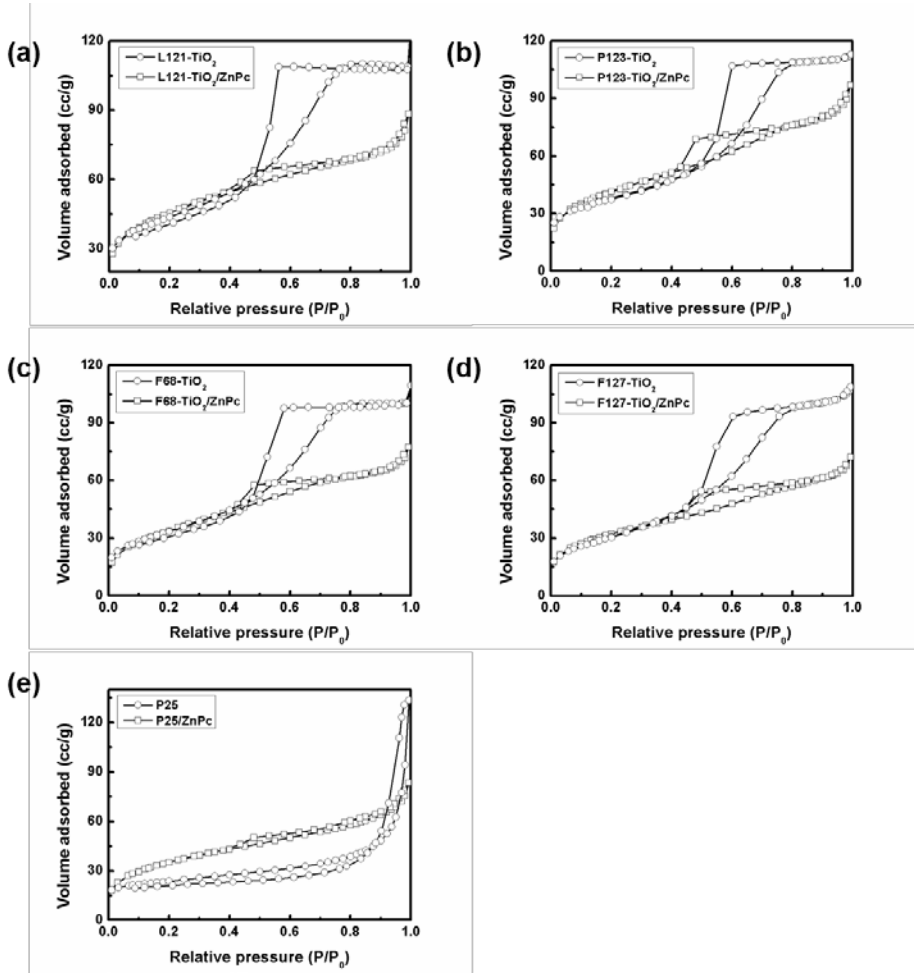

Fig. 3.6. N_2 adsorption-desorption isotherms for (a) L121-TiO_2 and L121-TiO_2/ZnPc, (b) P123-TiO_2 and P123-TiO_2/ZnPc, (c) F68-TiO_2 and F68-TiO_2/ZnPc, (d) F127-TiO_2 and F127-TiO_2/ZnPc, and (e) P25 and P25/ZnPc.

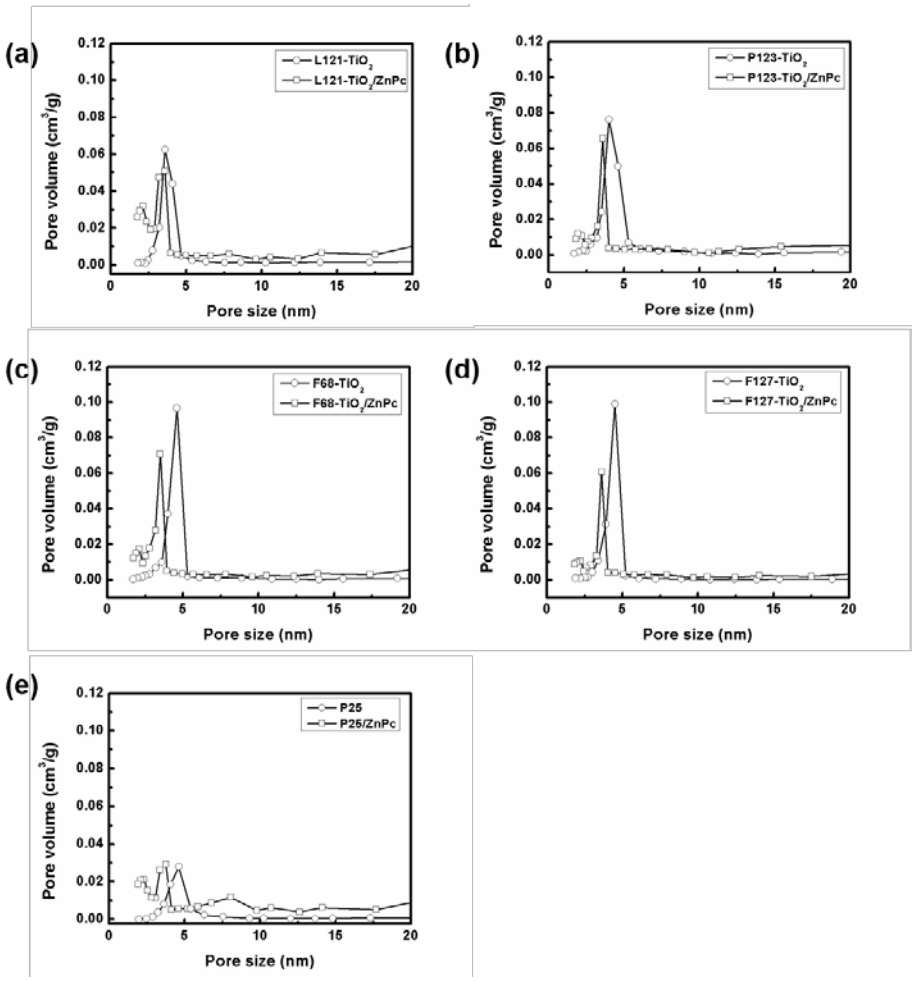

Fig. 3.7. BJH pore-size distributions for (a) L121-TiO_2 and L121-TiO_2/ZnPc, (b) P123-TiO_2 and P123-TiO_2/ZnPc, (c) F68-TiO_2 and F68-TiO_2/ZnPc, (d) F127-TiO_2 and F127-TiO_2/ZnPc, and (e) P25 and P25/ZnPc.

Table 3.2. Specific surface area and average pore size of TiO_2 and TiO_2/ZnPc hybrids.

Samples	Specific surface area (m^2/g)	Average pore size (nm)
L121-TiO_2	254.23	4.2
L121-TiO_2/ZnPc	228.87	3.7
P123-TiO_2	236.19	5.7
P123-TiO_2/ZnPc	223.76	3.9
F68-TiO_2	229.85	5.9
F68-TiO_2/ZnPc	211.49	3.6
F127-TiO_2	223.83	6.1
F127-TiO_2/ZnPc	192.06	3.8
P25	56.42	4.7
P25/ZnPc	49.02	4.3

3.3.4 Photocatalytic activity of TiO_2/ZnPc hybrids

Diffused reflectance spectroscopy (DRS) was used to characterize the electronic states of the TiO_2/ZnPc hybrids. Fig. 3.8 shows the UV-vis absorption spectra of the samples. Because the large band gap energy (3.1 eV), all TiO_2 have no significant absorbance for visible light and exhibit only fundamental absorption bands in the UV region. However, the spectra of all TiO_2/ZnPc samples display characteristic absorption bands in the range of 600−800 nm. From these results, it was confirmed that the TiO_2/ZnPc hybrids have the visible light activities.

Hence, we investigated the visible light photocatalytic performances of the TiO_2/ZnPc hybrids with respect to their ability to degrade methylene blue (MB) as a model contaminant for photocatalytic decolorization. Prior to irradiation, all samples in solution were magnetically stirred in the dark for 1 h to equilibrate the adsorption and desorption processes. The photocatalytic activities of the L121-TiO_2/ZnPc, P123-TiO_2/ZnPc, F68-TiO_2/ZnPc, F127-TiO_2/ZnPc, and P25/ZnPc under visible light condition were shown in Fig. 3.9 and table 3.3. The degradation efficiency (d_e%) was calculated with the following equation: $d_e\% = (C_0 - C_f)/C_0 \times 100$, where C_0 and C_f are the initial and final MB concentrations, respectively. The degradation rate was calculated using the pseudo-first-order equation as follows.

$$\ln \frac{C}{C_0} = -K_a t$$

where K_a is the rate constant, t is the reaction time, C_0 is the initial concentration of MB, and C is the interval concentration of MB. Under dark conditions (without visible light), no appreciable degradation of the MB solutions was observed after 90 min, in the presence of all TiO_2/ZnPc hybrids. Under visible light irradiation, the MB concentration dropped rapidly. Such reduction disappeared after 60 min of irradiation, indicating that the chromophoric structure of MB was almost decomposed. Considering that L121-TiO_2, P123-TiO_2, F68-TiO_2, F127-TiO_2, and P25 before the ZnPc incorporation did not show an appreciable degradation of the MB solution under visible light irradiation (Fig. 3.10), it was thought that the rapid decay of the MB concentration of TiO_2/ZnPc hybrids was attributed to the photosensitization of the ZnPc under visible light irradiation, followed by the photo-electron injection to the TiO_2 conduction band from lowest unoccupied molecular orbital (LUMO) of the ZnPc. The photocatalytic degradation efficiencies of the MB solution were 84.75%, 89.93%, 70.35%, 67.30%, and 42.42% for L121-TiO_2/ZnPc, P123-TiO_2/ZnPc, F68-TiO_2/ZnPc, F127-TiO_2/ZnPc, and P25/ZnPc, respectively. The photodegradation rate constants were found to be 0.013 min^{-1} (L121-TiO_2/ZnPc), 0.020 min^{-1} (P123-TiO_2/ZnPc), 0.008 min^{-1} (F68-TiO_2/ZnPc), 0.010 min^{-1} (F127-TiO_2/ZnPc), which were higher than that of

P25/ZnPc (0.005 min^{-1}). Typically, the photocatalytic activity is influenced by a specific surface area of photocatalyst. Accordingly, it was thought that the mesoporous TiO_2/ZnPc hybrids, with the high specific surface area to act as a photocatalytic reaction center, exhibited higher photocatalytic decomposition ability than simple nanoparticular P25/ZnPc. Interestingly, among the mesoporous TiO_2/ZnPc hybrids, P123-TiO_2/ZnPc showed the highest photocatalytic activity in the visible light region at about 1.06 times, 1.27 times, and 1.33 times of that of L121-TiO_2/ZnPc, F68-TiO_2/ZnPc, and F127-TiO_2/ZnPc, respectively. We note that the crystallinity and the specific surface area of the mesorporous TiO_2/ZnPc hybrids did not show the critical difference. In addition, we found that the amount of the ZnPc in the TiO_2/ZnPc hybrids were similar to inductively coupled plasma atomic emission spectroscopy (ICP–AES) (L121-TiO_2/ZnPc = 2018.76 ppm, P123-TiO_2/ZnPc = 1900.83 ppm, F68-TiO_2/ZnPc = 1943,76 ppm, F127-TiO_2/ZnPc = 1931.99 ppm). These results suggested that the different photocatalytic activities of mesoporous TiO_2/ZnPc hybrids were ascribed to other structural factor, excepting for the crystallinity, surface area, and the amount of ZnPc.

To elucidate the origin of different photocatalytic performance of TiO_2/ZnPc hybrids, we investigated the light scattering effect of TiO_2 itself, before the incorporation of ZnPc using diffused reflectance spectroscopy (DRS) that is generally accepted as an efficient tool to determine light scattering ability [52].

The DRS spectra of the mesoporous TiO_2 (L121-TiO_2, P123-TiO_2, F68-TiO_2, and F127-TiO_2) and P25 are shown in Fig. 5. All of the mesoporous TiO_2 exhibited high reflectance over all wavelength region, whereas P25 showed a small reflectance. This implies that all of the mesoporous TiO_2 had better light scattering ability in the visible light region (400–800 nm) than P25. Interestingly, among the mesoporous TiO_2, P123-TiO_2 which had 548 nm in size possessed the highest reflectance spectra in the wavelength range of 400–800 nm. It is well known that a light scattering performance is mainly dependent on the particle size and that Mie scattering particularly occurs when the size is comparable with the wavelength of incident light. Such Mie scattering can lead to an increase in the light utilization, resulting in the enhancement of photocatalytic activity of the phtocatalysis [44-48]. Thus, the P123-TiO_2/ZnPc with a size of 548 nm was thought to strongly generate the Mie scattering, and the visible light scattered by the P123-TiO_2/ZnPc would hit the P123-TiO_2/ZnPc again. As a result, P123-TiO_2/ZnPc can have an amplified photocatalytic efficiency, due to a cascade scattering of the unabsorbed visible light to the ZnPc molecules on the surface of the P123-TiO_2/ZnPc hybrid. However, the size of P25 was too small, and thereby it could not act as a scattering center under visible light irradiation, resulting in low photocatalytic degradation efficiency. In addition, the other mesoporous TiO_2/ZnPc hybrids (L121-TiO_2/ZnPc, F68-TiO_2/ZnPc, and F127-TiO_2/ZnPc), which had relatively

low Mie scattering ability ascribed to the size mismatch, also exhibited lower photocatalytic activity than P123-TiO_2/ZnPc. Consequently, the combined results from photocatalytic performance and DRS showed that the appropriate size, which could efficiently generate Mie scattering, was a crucial factor that could improve the photocatalytic performance of the mesoporous TiO_2/ZnPc hybrids.

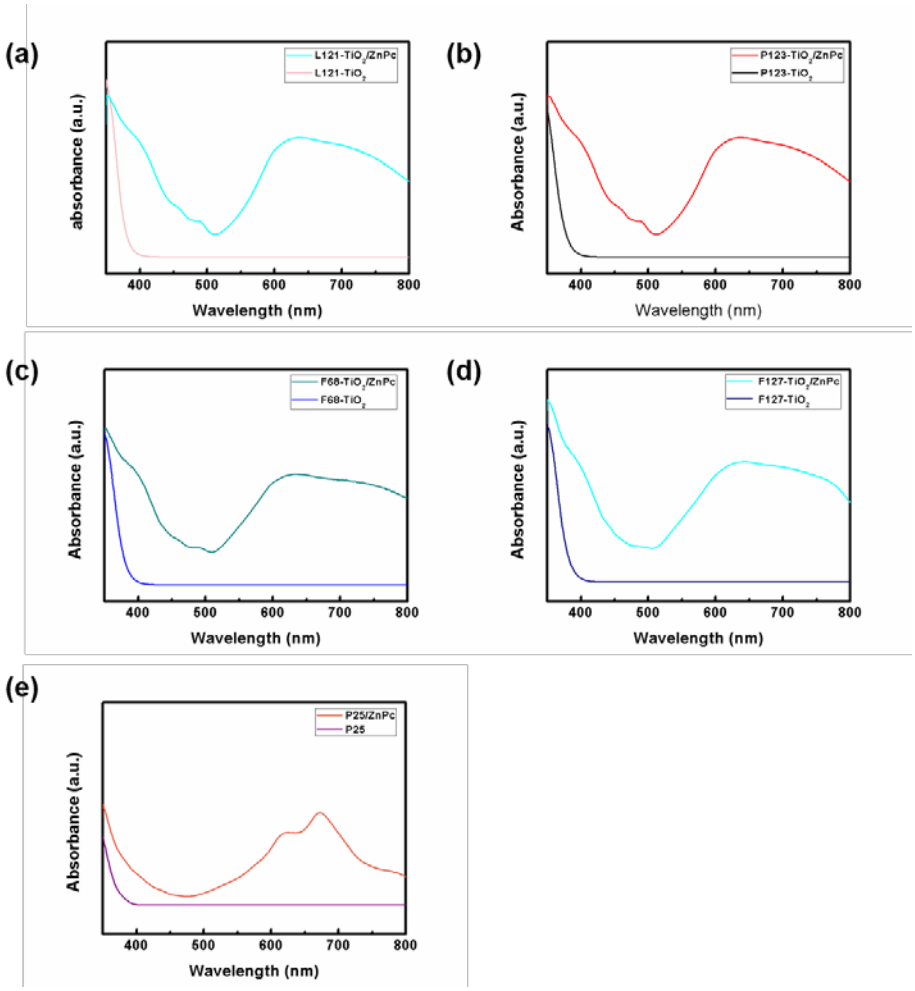

Fig. 3.8. DRS spectra of the (a) L121-TiO_2 and L121-TiO_2/ZnPc, (b) P123-TiO_2 and P123-TiO_2/ZnPc, (c) F68-TiO_2 and F68-TiO_2/ZnPc, (d) F127-TiO_2 and F127-TiO_2/ZnPc, and (e) P25 and P25/ZnPc.

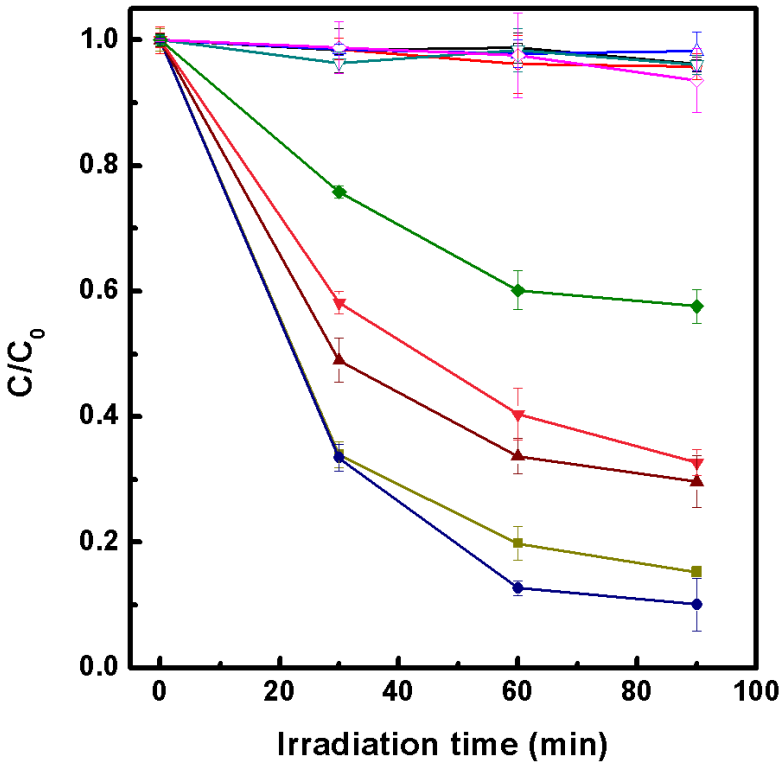

Fig. 3.9. Comparison of photocatalytic activity for MB with different catalysts: (□) L121-TiO_2/ZnPc without light, (○) P123-TiO_2/ZnPc without light, (△) F68-TiO_2/ZnPc without light, (▽) F127-TiO_2/ZnPc without light, (◇) P25/ZnPc without light, (■) L121-TiO_2/ZnPc, (●) P123-TiO_2/ZnPc, (▲) F68-TiO_2/ZnPc, (▼) F127-TiO_2/ZnPc, and (◆) P25/ZnPc.

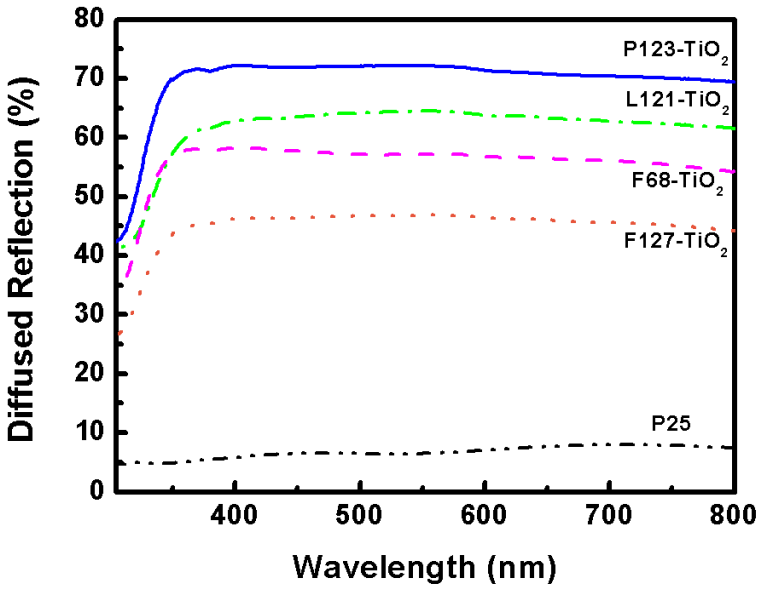

Fig. 3.10. DRS spectra of the mesoporous TiO_2 (L121-TiO_2, P123-TiO_2, F68-TiO_2, and F127-TiO_2) and P25.

Table 3.3. Physical and photocatalytic properties of the TiO_2/ZnPc hybrids.

	Crystal size (nm)	Diameter (nm)	Specific surface area (m^2/g)	Pore size (nm)	Rate constant (min^{-1})	Degradation efficiency (%)
L121-TiO_2/ZnPc	8.19	245	228.87	3.7	0.013	84.75
P123-TiO_2/ZnPc	7.87	548	223.76	3.9	0.020	89.93
F68-TiO_2/ZnPc	7.42	798	211.49	3.6	0.008	70.35
F127-TiO_2/ZnPc	7.28	1188	192.06	3.8	0.010	67.30
P25/ZnPc	–	–	49.02	4.3	0.005	42.42

3.4 Summary

In this study, we synthesized anatase mesoporous TiO_2/ZnPc hybrids in various sizes (245 nm, 548 nm, 798 nm, and 1188 nm) having similar crystallite size, specific surface area, and amount of ZnPc. It was confirmed that the incorporation of ZnPc in TiO_2 extended the absorption spectra of TiO_2, followed by the formation of visible light active photocatalyst. We found that submicron- and micron-sized mesorporous TiO_2/ZnPc hybrids exhibited high photocatalytic activity due to a cascade Mie light scattering. In particular, P123-TiO_2/ZnPc hybrid, which size is comparable with the wavelength of incident light, strongly generated the Mie scattering, followed by a considerable enhancement of the photocatalytic activity. The mesoporous TiO_2/ZnPc hybrid, described here, provides a new approach to the design of high-performance photocatalysts using cascade Mie scattering and has tremendous potential for practical use, ranging from water purification to hydrogen generation.

References

1. M. R. Hoffmann, S. T. Martin, W. Y. Choi and D. W. Bahnemann, Chem. Rev. 95 (1995) 69–96.
2. X. B. Chen and S. S. Mao, Chem. Rev. 7 (2007) 2891–2959.
3. H. Zhang, G. Chen and D. W. Bahnemann, J. Mater. Chem. 19 (2009) 5089–5121.
4. A. Hagfeldt, M. Gra¨tzel, Chem. Rev. 95 (1995) 49–68.
5. A. Imhof, D.J. Pine, Nature 389 (1997) 948–951.
6. J.E.G.J. Wijnhoven, W.L. Vos, Science 281 (1998) 802–804.
7. H. Fujii, M. Ohtaki, K. Eguchi, J. Am. Chem. Soc. 120 (1998) 6832–6833.
8. Z. H. Zhang, Y. Yuan, G. Y. Shi, Y. J. Fang, L. H. Liang, H. C. Ding and L. T. Jin, Environ. Sci. Technol. 41 (2007) 6259–6263.
9. S. Kohtani, M. Tomohiro, K. Tokumura and R. Nakagaki, Appl. Catal. B 58 (2005) 265–272.
10. H. Irie, Y. Watanabe, K. Hashimoto, Chem. Lett. 32 (2003) 772–773.
11. T. Morikawa, R. Asahi, T. Ohwaki, K. Aoki and Y. Taga, Jpn. J. Appl. Phys. 40 (2001) 561–563.
12. A. Fujishima, X. Zhang, D. A. Tryk, Surface Science Reports 63 (2008) 515–582.
13. S. Sato, Chem. Phys. Lett. 123 (1986) 126-128.
14. S. Sato, R. Nakamura, S. Abe, Appl. Catal. A: General 284 (2005) 131-137.
15. N. Serpone, J. Phys. Chem. B 110 (2006) 24287-24293.
16. S.U.M. Khan, M. Al-Shahry, W.B. Ingler, Science 297 (2002) 2243-2245.
17. E. Borgarello, J. Kiwi, M. Gratzel, E. Pelizzetti, M. Visca, J. Am. Chem. Soc. 104 (1982) 2996-3002.
18. X. Z. Li and F. B. Li, Environ. Sci. Technol. 35 (2001) 2381-2387.

19. K. Demeestre, J. Dewulf, T. Ohno, P. H. Salgado, H. V. Langenhove, Appl. Catal. B: Environ. 61, (2005) 140-149.
20. D. Dvoranova, V. Brezova, M. Mazur and M. A. Malati, Appl. Catal. B: Environ. 37 (2002) 91-105.
21. F. B. Li and X. Z. Li, Chemosphere 48 (2002) 1103-1111.
22. T. Ohno, F. Tanigawa, K. Fujihara, S. Izumi, M. Matsumara, J. Photochem. Photobiol. A 127 (1999) 107-110.
23. J. C.-S. Wu and C.-H. Chen, J. Photochem. Photobiol. A 293 (2004) 509-515.
24. T. Wu, T. Lin, J. Zhao, H. Hidaka, N. Serpone, Environ. Sci. Technol. 33 (1999) 1379–1387.
25. T. Wu, G. Liu, J. Zhao, H. Hidaka, N. Serpone, J. Phys. Chem. B 102 (1998) 5845–5851.
26. Y. Xu, C.H. Langford, Langmuir 17 (2001) 897–902.
27. N. Ghows, M.H. Entezari, Ultrason. Sonochem. 18 (2011) 629–634.
28. R. Brahimi, Y. Bessekhouad, A. Bouguelia, M. Trari, Catal. Today 122 (2007) 62–65.
29. P.V. Kamat, J. Phys. Chem. C 112 (2008) 18737–18753.
30. B. O'Regan and M. Gratzel, Nature 353 (1991) 737-739.
31. K. Vinodgopal, U. Stafford, K.A. Gray, P.V. Kamat, J. Phys. Chem. 98 (1994) 6797–6803.
32. K. Vinodgopal, I. Bedja, P.V. Kamat, Chem. Mater. 8 (1996) 2180–2187.
33. J. B. Asbury, E. Hao, Y. Wang, H.N. Ghosh, T. Lian, J. Phys. Chem. B 105 (2001) 4545–4557.
34. F. H. Moster, A. L. Thomas, J. Chem. Educ. 41 (1964) 245–245.
35. P. Borker, A. V. Salker, Indian J. Chem. Technol. 13 (2006) 341–346.
36. G. R. Rao, H. R. Sahu, Proc. Indian. Acad. Sci. 113 (2001) 651–658.

37. R. Slota, G. Dyrda, K. Szczegot, G. Mele, I. Pio, Photochem. Photobiol. Sci. 10 (2011) 361–366.
38. G. Marcì, E. Garcí-López, G. Mele, L. Palmisano, G. Dyrda, R. Slota, Catal. Today 143 (2009) 203–210.
39. C. Wang, G. Yang, J. Li, G. Mele, R. Slota, M. A. Broda, M. Duan, G. Vasapollo, X. Zhang, F. X. Zhang, Dyes Pigm. 80 (2009) 321-328.
40. R. Slota, G. Dyrda, Z. Hnatejko, J. Karolczak, Z. Stryla, J. Porphyrins Phothalocyanines 10 (2006) 43-54.
41. G. de la Torre, P. Vazquez, F. Agullo-Lopez, T. Torees, Chem. Rev. 104 (2004) 3723–3750.
42. M. G. Walter, A. B. Rudine, C. C. Wamser, J. Porphyrins Phthalocyanines 14 (2010) 759-792.
43. P. Borker, A. V. Salker, Indian J. Chem. Technol. 13 (2006) 341-346.
44. Q. Zhang, T. P. Chou, B. Russo, S. A. Jenekhe, G. Cao, Angew. Chem. Int. Ed. 47 (2008) 2402–2406.
45. H. C. Van de Hulst, Light Scattering by Small PARTICLES, Wiley, New York, 1957.
46. Craig F. Bohren, Donald R. Huffman, Absorption and Scattering of Light by Small Particles, Wiley–Interscience, New York, 1983.
47. Z. S. Wang, H. Kawauchi, T. Kashima, H. Arakawa, Coord. Chem. Rev. 248 (2004) 1381–1389.
48. S. Hore, C. Vetter, R. Kern, H. Smit, A. Hinsch, Sol. Energy Mater. Sol. Cells 90 (2006) 1176–1188.
49. A. E. H. Machado, M. D. Franca, V. Velani, G. A. Magnino, H. M. M. Velani, F. S. Freitas, P. S. Muller Jr., C. Satter, M. Schmucker, Int. J. Photoenergy 2008 (2008) Article ID 482373 1–12.
50. D. S. Kim, S. J. Han, S.-Y. Kwak, J. Colloid Interface Sci. 316 (2007) 85–91.

51. H. –J. Kim, J. –D. Jeon, J. W. Chung, S. –Y. Kwak, Microporous Mesoporous Mater. 227 (2016) 169–175.
52. W. E. Vargas, J. Appl. Phys. 88 (2000) 4079–4084.

Chapter 4

Dual-Functional TiO_2 Working Electrode with TiO_2 Sphere for Dye-Sensitized Solar Cells

4.1 Introduction

Dye-sensitized solar cells (DSSCs) is an interesting alternative solar cell technology that have recently been intensively studied due to their attractive properties: low fabrication cost, less toxic manufacture, relatively high energy conversion efficiency, and substrates that are more flexible than those of silicon-based solar cells [1–11]. Typical DSSCs are comprised of a fluorine-doped SnO_2 substrate, a titanium dioxide film, a sensitizing dye, an electrolyte, and a counter electrode. A simple introduction to the mechanism involved in DSSCs is described as below: The electrons generated from the excited dye molecules upon irradiation with visible light are injected into the conduction band of the TiO_2 electrode. The oxidized dye molecules are regenerated by I^- ions in the electrolyte, and the I^- ions are oxidized to I_3^- ions. The I_3^- ions are reduced to I^- ions by accepting electrons at the counter electrode, and the process is repeated [12–14]. A TiO_2 electrode with a high surface area is essential for the loading of large numbers of sensitizing dye molecules that engender photoelectrons upon the absorption of the incident light [15–17].

Typical photoelectrodes are thus composed of porous TiO_2 nanocrystallites (~20 nm), which maximize the uptake of dye molecules. However, small nanocrystallites with large surface areas do not always produce the best performance due to the increased number of grain boundaries and defects on their surfaces, which can delay the electron transport; such TiO_2 nanocrystal electrodes can cause the exhibition of high transparency and insufficient light scattering in the visible light region due to the small particle size, which results in poor light-harvesting efficiency.

Many studies have been carried out in the attempt to enhance the light harvesting efficiency of DSSCs. One approach is to improve light harvesting by adding a scattering layer to the TiO_2 nanocrystal electrode [18]. It has been demonstrated that scattering layers improve light harvesting and thus enhance the light conversion efficiency of solar cells. According to Mie theory, the particles utilized to scatter visible light should be large; and it has been verified that sub-micron-sized particles result in the effective light scattering [19]. When incident light collides with the sub-micron-sized particles, the light will be scattered violently, which increases the light path length in the nanocrystalline TiO_2 films. However, the small surface-to-volume ratio of sub-micron-sized TiO_2 particles limits the adsorption of dye molecules. The incorporation of a light scattering over-layer results in an increase in film thickness and the loss of photons traveling through the electrolyte-filled TiO_2

electrodes, as well as increases in the recombination rate and the path length of the injected photo-electrons [20,21]. To address these issues, submicron-sized TiO_2 beads that enhance the light-harvesting capability of the TiO_2 electrode, without reducing the area of the surface accessible to dye loading, have been reported recently. Lee et al. [7], Kim et al. [22], and Murayama et al. [23] prepared hollow submicron-sized TiO_2 spheres, consisting of primary nanocrystallites, via a sol-gel reaction with polystyrene beads as the template. They found that a DSSC with the TiO_2 hollow spheres exhibits enhanced light harvesting efficiency. This improvement results from the multiple reflecting and scattering of incident light by the hollow spheres. However, the introduction of hollow spheres as scattering centers reduces the dye-loading capacity of the electrodes due to the large voids in the hollow spheres.

Chen et al. designed a working electrode containing spherical TiO_2 beads consisting of TiO_2 nanocrystallites, which was found to be able to enhance the light-harvesting efficiency of the associated DSSC, and therefore improves the energy-conversion efficiency [3]. Shao et al. synthesized porous spherical TiO_2 aggregates via an interfacial con- fined formation, which were found to enhance electron transfer and light scattering in DSSCs. However, the voids between the aggregated TiO_2 particles in the TiO_2 electrodes are larger than those in the TiO_2 nanocrystallite electrodes. The comparably large sizes of the voids result in poor connectivity and ineffective charge transfer between the aggregated

TiO_2. Such poor connectivity between aggregated TiO_2 often limits the effectiveness of charge transfer, which leads to reduced DSSC performance [24, 25]. In this paper, we reported the preparation of mesoporous TiO_2 spheres with various aggregated sizes. These spheres were synthesized by using surfactants with ethylene oxide groups of various lengths. To achieve satisfactory dispersion of the TiO_2 spheres in suspensions, treatment with nitric acid was performed. We fabricated composite-type photoelectrodes consisting of TiO_2 spheres mixed with small TiO_2 particles as the binder. In order to further improve the connectivity between the TiO_2 spheres, we used the hot-pressing compression technique to prepare TiO_2 electrodes on fluorine doped tin oxide (FTO) substrates. This hot-press technique was found to improve the connectivity between the TiO_2 spheres, as well as the mechanical adhesion of the TiO_2 electrode to the FTO substrate. These composite-type electrodes were used as scattering layers and working electrodes in DSSC devices and their effects on the conversion efficiency of the devices were investigated.

4.2 Experiments

4.2.1 Materials

Titanium (IV) isopropoxide (TTIP, $Ti(OPr^i)_4$), Pluronic P123 (P123, $EO_{20}PO_{70}EO_{20}$), Pluronic F127 (F127, $EO_{108}PO_{70}EO_{108}$), 2,4-pentanedione (acetylacetone, AcAc), sulfuric acid, nitric acid poly(ethylene glycol) (PEG, average MW = 10,000) and poly(ethylene oxide) (PEO, average MW = 100,000) were all purchased from Sigma-Aldrich and used as received without further purification. cis-Diisothiocyanato-bis(2,2-bipyridyl-4,4-dicarboxylato) ruthenium(II) bis (tetrabutylammonium) (D719), fluorine doped tin oxide (FTO) substrates and Ti-nanoxide T pastes were purchased from Solaronix. The water used in all syntheses was distilled and deionized.

4.2.2 Fabrication of TiO_2 nanoparticle/mesoporous shpere composite films

The weight content of the nitric acid treated spheres in the suspension is 40 wt.%. The pastes were prepared by admixing the 10 g of suspension with 0.12 g of PEG, and 0.12 g of PEO, and then TiO_2 nanoparticle incorporated mesoporous sphere (S1 and S2) composite pastes were prepared by mixing with 2 g of Ti-nanoxide-T paste, and the resulting pastes were doctor-bladed onto the FTO substrates (N-S1 and N-S2, respectively). In order to further improve

connectivity between the TiO_2 spheres, the coated composite TiO_2 films (N-S1 and N-S2) were then pressed (N-S1-P and N-S2-P, respectively). Typical pressures were 12 MPa with plates preheated to 120 °C for 10 min. Teflon plates were inserted between the composite TiO_2 films and the plate to prevent the films sticking to the plate. The films were then calcined at 450 °C for 30 min in air.

4.2.3 Assembly of the DSSCs

Before adsorbing the dye, the composite TiO_2 electrode was treated with heat for 30 min at 200 °C and dried in a vacuum oven for 2 h at 90 °C in order to remove any excess water and organic residues. The composite TiO_2 electrodes were immersed in an ethanolic solution containing a ruthenium sensitizer dye, $3 \times 10{-}4$ M D719 for 12 h. The platinized counter electrode was placed on top of the dye-coated TiO2 photo-electrode sealed with a Surlyn film (25 μm thick, DuPont), and the electrolyte, which was composed of 1-butyl-3-methyl-imidazolium iodide (BMII, 0.7 M, Merck), I_2 (0.03 M), guanidinium thiocyanate (GSCN, 0.1 M, Aldrich), and 4-tert-butylpyridine (TBP, 0.5 M, Aldrich) in acetonitrile and valeronitrile (85:15 v/v), was injected through a hole in the counter electrode.

4.2.4 Charaterization

The surface features and morphologies of the TiO_2 spheres were investigated by using field-emission scanning electron microscopy (FE-SEM, JEOL JSM-6330 F) and high-resolution transmission electron microscopy (HR-TEM, JEOL JEM-2000 FX II). Photovoltaic measurements were conducted by illuminating the DSSCs with light from a 450 W Xe lamp that had been directed through an AM 1.5 solar simulator. The intensity of the simulated light was calibrated by using a Si reference solar cell equipped with a BK7 filter to approximate AM 1.5, 100 mW cm^{-2} global radiation. The photovoltaic characteristics of the DSSCs were obtained by applying an external potential bias to the cells and measuring the generated photocurrent with a Keithley 2400 source meter. IPCEs were measured as a function of wavelength from 350 to 800 nm using a specially designed IPCE system for dye-sensitized solar cells (PV Measurements, Inc.). A 75 W xenon lamp was used as the light source for generating a monochromatic beam. Calibration was performed using a NIST-calibrated silicon photodiode as a standard. IPCE values were collected at a low chopping speed of 5 Hz.

4.3 Results and Discussion

4.3.1 Morphology and optical properties of mesoporous TiO_2 sphere/nanocrystalline TiO_2 composite film

Fig. 4.1 (a), (b), and (c) shows FE-SEM images of film surfaces composed of S1, and of TiO_2 spheres/nanoparticles before and after compression, respectively [26]. Voids, larger than 1 μm, can be found in the film composed of TiO_2 spheres, whereas the voids in the film composed of TiO_2 spheres/nanoparticles are much smaller. The presence of these large voids between the TiO_2 spheres limits their connectivity and prevents effective charge transfer. Such a poor connectivity is likely to result in an increased electron diffusion distance and reduced energy conversion efficiency. FE-SEM cross-sectional images of TiO_2 films fabricated on FTO substrates are shown in Fig. 4.1 (d) and (e). The thicknesses of the mesoporous TiO_2 sphere film without hot-press treatment and of TiO_2 composite films with press treatment were approximately 20 μm and 10 μm, respectively. The magnitude of the reduction in film thickness as a result of the compression process is approximately 50%. The films consisting of TiO_2 nanoparticles appear semi-transparent, which indicates the partial transmittance of incident visible radiation. An increase in the light scattering ability of the film is important for enhancing the light-harvesting efficiency and thus the photon to current conversion efficiency of

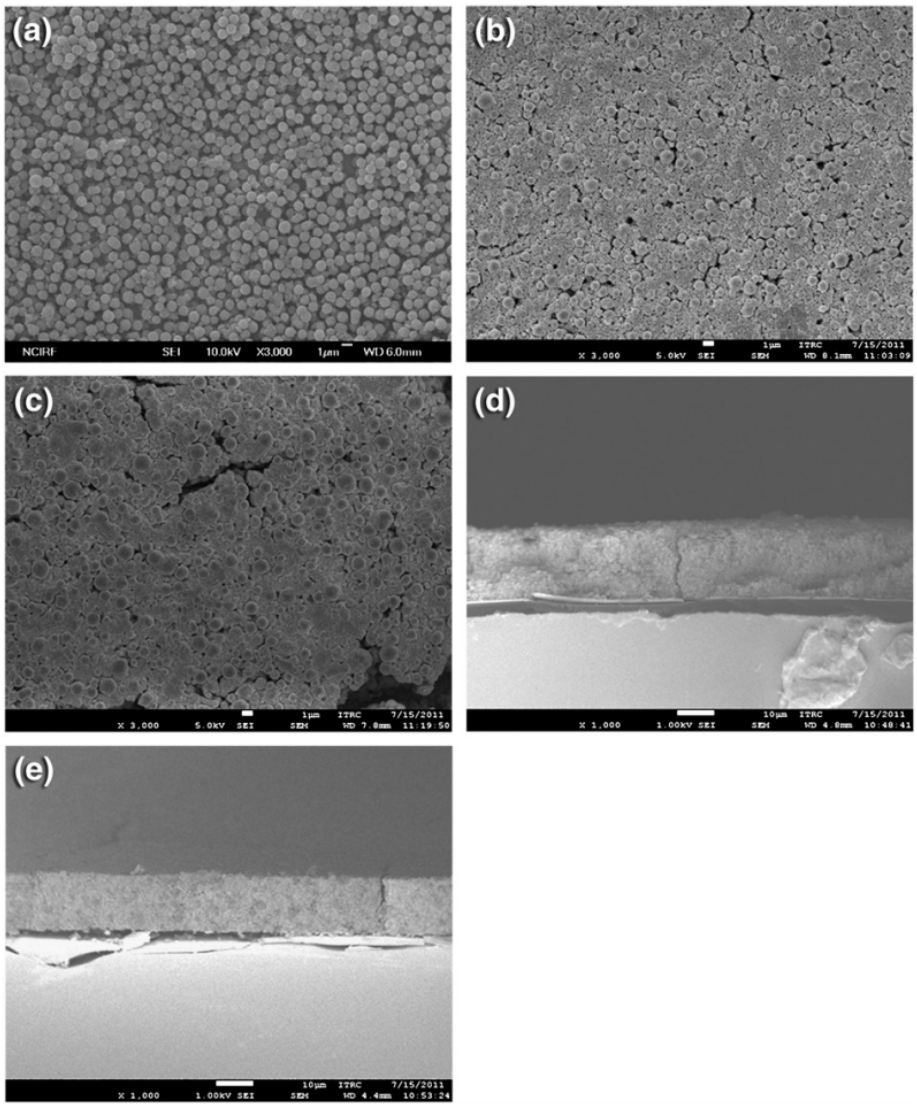

Fig. 4.1. Surface FE-SEM images for films prepared from (a) S1, (b) N-S1, (c) N-S1-P and cross-section FE-SEM images of films prepared (d) N-S1 and (e) N-S1-P.

the associated DSSC. As shown in the transmittance spectra of nanocrystalline TiO_2 (P25, labeled NC) and the as-prepared TiO_2 spheres (S1 and S2) (Fig. 4.2), NC is more transparent with respect to visible light than the films with TiO_2 spheres, which indicates that the TiO_2 spheres trap more light. This property means that the films composed of TiO_2 spheres can prevent visible light from escaping the devices. As discussed above, the scattering of light by the TiO_2 spheres enhances light trapping and hence light utilization in the film.

4.3.2 Photovoltaic performance of mesoporous TiO_2 sphere/nanocrystalline TiO_2 composite film

Fig. 4.3 shows that the performances of *J–V* curves of DSSCs based on photoelectrodes made of TiO_2 spheres (S1 and S2), TiO_2 spheres/TiO_2 nanoparticle composite (N-S1 and N-S2), TiO_2 spheres/TiO_2 nanoparticle composite with compression (N-S1-P and N-S2-P) and nanocrystalline TiO_2 (NC): D719 were used as a sensitizer without any chemical modification or anti-reflection coating. The open circuit voltage (V_{oc}), short circuit current (J_{sc}), fill factor (FF), and energy conversion efficiency (η) of the DSSCs are also summarized in Table 2. The DSSC with the photoelectrode consisting of TiO_2 spheres (S1 and S2) reached an energy conversion efficiency of 5.83 and 5.47%, respectively, whereas that of NC achieved an energy conversion efficiency of

4.50%. The admixing of TiO_2 spheres into TiO_2 nanoparticles results in an enhancement in DSSC performance. As shown in Table 4.1, all the values of the samples except J_{sc} are similar. Therefore, on the basis of the TiO_2 electrode characteristics, we suggest that the increase in energy conversion efficiency is ascribed to the improvement of J_{sc}. The improvement in the efficiency of the DSSCs with a photoelectrode consisting of TiO_2 spheres/nanoparticles can be explained as follows. Submicron sized TiO_2 spheres improve the light scattering efficiency and thus increase the probability of photon capture from the incident light [27], the cause of J_{sc} improvement could be due to the scattering effect of TiO_2 sphere, as well as the mesoporous structure of TiO_2 sphere. The amounts of adsorbed dye were determined by measuring the dye concentration eluted from the mesoporous TiO_2 spheres with UV–vis absorption spectroscopy. The result of dye adsorption experiment shown in Table 4.2, depicts that dye adsorption of S1 and S2 compared to that of NC, was by approximately 1.89 and 1.72 folds higher, respectively, which is in good agreement with the BET/BJH results. It is inferred that the improved DSSCs fabricated from TiO_2 spheres are closely related to larger amounts of anchored dye sensitizers. In order to compare the photovoltaic performance of S1, S2 and NC, incident photon to current conversion efficiency (IPCE) spectra of the TiO_2 electrodes were recorded. Fig. 4.4 displays the IPCE spectra of the DSSCs fabricated with electrodes consisting of S1, S2 and NC. The dye-loading

capacity of each photoelectrode is reflected on the corresponding IPCE in the shorter wavelength region (400–600 nm), while the light scattering efficiency can be explained by the IPCE value in the longer wavelength region (above 600 nm). As shown in Fig. 4.4, the TiO_2 films prepared from S1 and S2 possessed higher IPCE values over a wide range than films of NC of similar thickness. Compared to the NC electrodes, the increase in IPCE values for S1 and S2 at short wavelength region could be mainly attributed to their higher dye loading capacities [27]. In the long wavelength region, the higher IPCE values of S1 and S2 could be ascribed to the enhanced light scattering capacities, which promotes the light harvesting of the D719 dye in the region [18, 19, 28]. Therefore, the higher IPCE value above 600 nm can be attributed to the light scattering abilities of the photoelectrodes, which leads to increase the probability of interaction between the photons and the dye molecules that adsorb on the TiO_2 surface. In the case of N-S1 and N-S2, the dye-loading is slightly increased because the TiO_2 nanoparticles fill the voids between the TiO_2 spheres. However, no significant difference was found between the dye adsorption of the electrodes with TiO_2 spheres (S1 and S2) and of the composite-type electrodes (N-S1 and N-S2). It is deduced that the dye-loading capacity of the TiO_2 spheres is superior to that of the TiO_2 nanoparticle used as binder. The performance of the cells produced by the compression technique was evaluated in terms of their *J–V* characteristics under white light

illumination: Table 4.1 summarizes the results. The maximum energy conversion efficiency of the pressed electrodes (N-S1-P) was measured to be 7.66% with J_{sc} = 14.53 mA cm^{-2}, V_{oc} = 0.79 V, and FF = 0.66. After compression, V_{oc} of N-S1 and N-S2 (0.69 V and 0.96 V, respectively) improved compared to N-S1-P and N-S2-P (0.79 V and 0.72 V, respectively). It is known that V_{oc} depends on the back-reaction of the injected photo-electrons [29]. The improvement of V_{oc} may be explained due to the improved connectivity between spheres and the increased number of electron pathways and therefore less resistance to electron transfer to the sphere interface. The increased light scattering, dye-loading capacity of the electrode with TiO_2 spheres answers for the improved performance of DSSC. And the compression process improves the connectivity between TiO_2 spheres, which can decrease the serious resistance and enhance the V_{oc}.

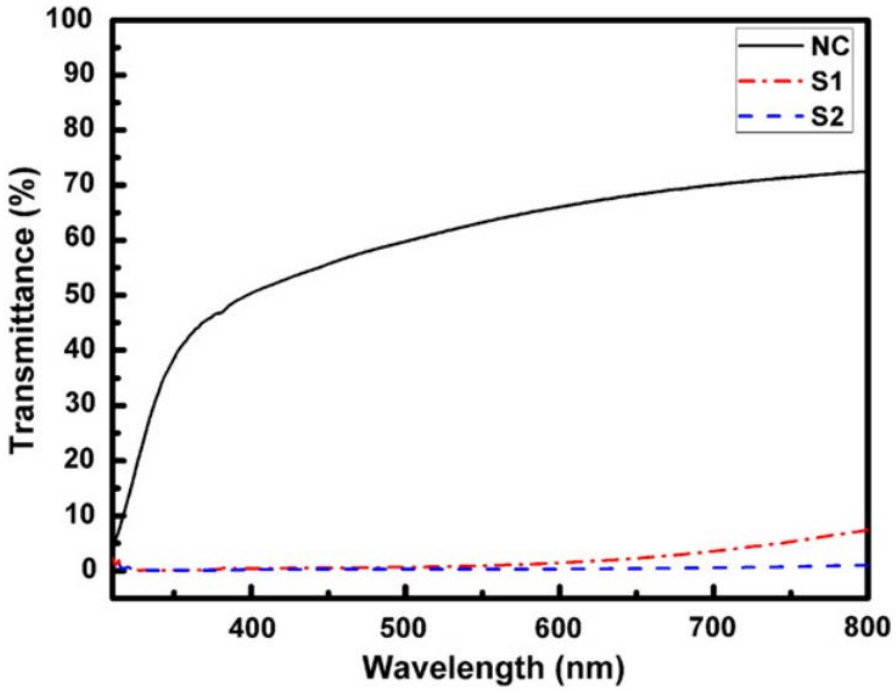

Fig. 4.2. UV-visible transmittance spectra of films prepared S1, S2, and NC.

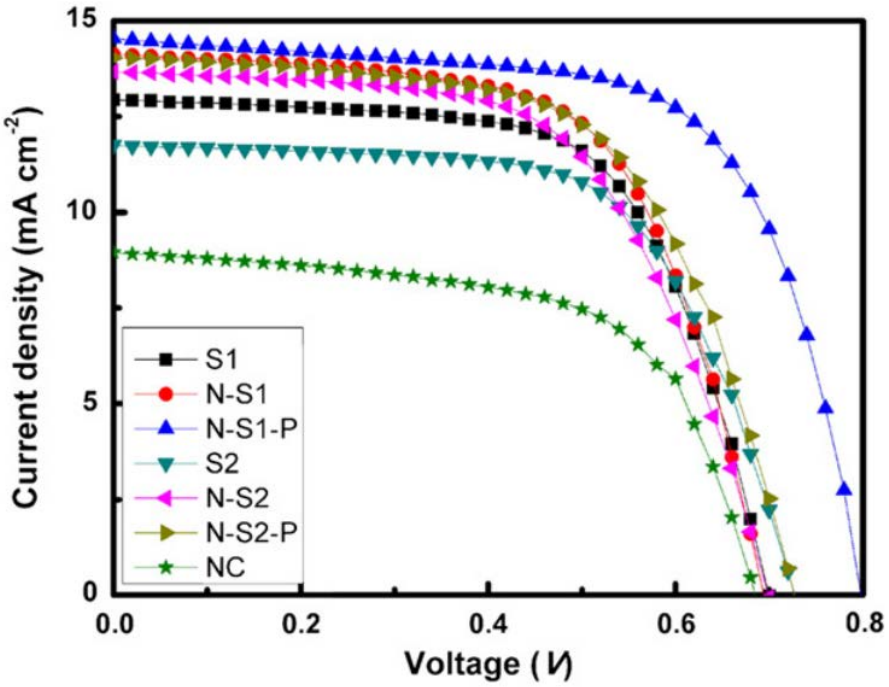

Fig. 4.3. *J-V* curves of DSSCs prepared from various TiO_2 photoelectrodes.

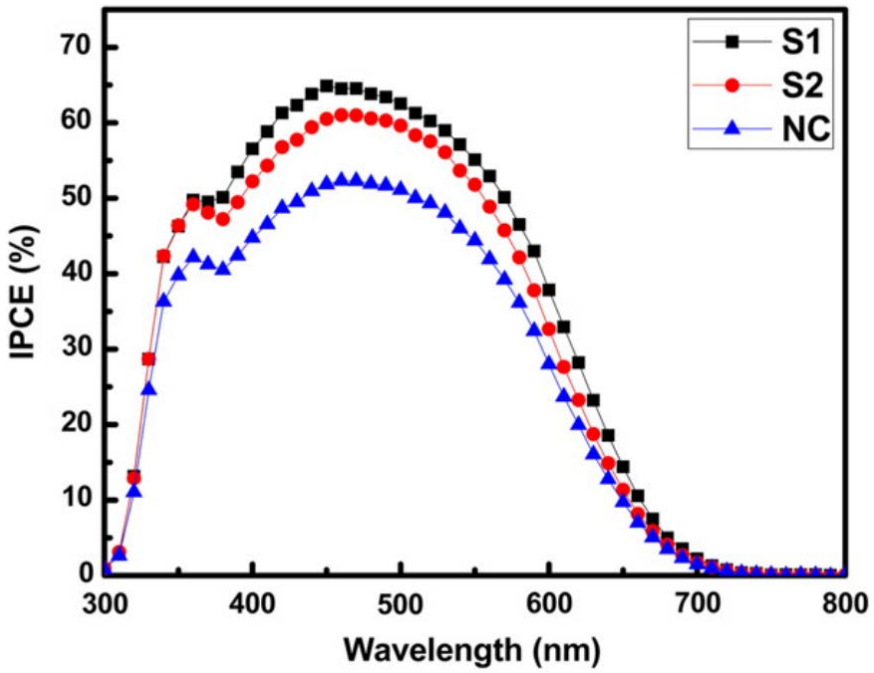

Fig. 4.4. IPCE spectra of DSSCs prepared from S1, S2, and NC.

Table 4.1. Characteristics of DSSCs prepared from various TiO_2 photoelectrodes.

	V_{oc} (V)	J_{sc} (mA/cm^2)	FF	η
S1	0.70 ± 0.2	12.93 ± 0.1	0.64 ± 0.3	5.83 ± 0.06
N-S1	0.69 ± 0.0	14.13 ± 0.2	0.62 ± 0.1	6.17 ± 0.07
N-S1-P	0.79 ± 0.1	14.53 ± 0.1	0.66 ± 0.3	7.66 ± 0.04
S2	0.72 ± 0.2	11.75 ± 0.1	0.64 ± 0.2	5.47 ± 0.07
N-S2	0.69 ± 0.1	13.67 ± 0.3	0.60 ± 0.3	5.72 ± 0.04
N-S2-P	0.72 ± 0.0	14.03 ± 0.1	0.61 ± 0.2	6.19 ± 0.06
NC	0.70 ± 0.1	10.05 ± 0.0	0.64 ± 0.2	4.50 ± 0.05

Table 4.2. Dye-loading capacity of the various photoelectrodes.

	Amount of adsorbed dye per unit area (μmol/cm^2)
S1	209.96
N-S1	255.34
N-S1-P	253.50
S2	191.48
N-S2	224.03
N-S2-P	218.91
NC	110.97

4.4 Summary

In this study, we fabricated TiO_2 electrodes based on mesoporous TiO_2 spheres, which have 2–3 times higher dye-loading capacity than nanocrystal electrode. The effects of filling the voids between the TiO_2 spheres with TiO_2 nanoparticles as the binder were investigated. The mesoporous TiO_2 spheres act as scattering centers that improved light scattering without damaging the dye-loading capacity of the internal surface area, and the TiO_2 nanoparticles successfully filled the large voids between the TiO_2 spheres and improved the connectivity for charge transport. The TiO_2 electrodes were compressed to improve the connectivity between the large TiO_2 spheres and the adhesion of the film with the FTO substrate. This compression was found to result in higher energy conversion efficiency than the one obtained with TiO_2 nanoparticles alone. The improved dye-loading capacity and light scattering efficiency, and better electrical connectivity of the film are important characteristics of the electrodes produced by these methods. An overall energy conversion efficiency of 7.66% has been achieved by using these TiO_2 sphere/nanoparticle composite electrodes in DSSCs, which is significantly higher than that one arose from TiO_2 nanoparticle electrodes of similar thickness (4.50%).

References

1. B. O'Regan, M. Grätzel, Nature 353 (1991) 737–740.
2. K.-M. Lee, V. Suryanarayanan, K.-C. Ho, Sol. Energ. Mat. Sol. Cells 91 (2007) 1416–1420.
3. D. Chen, F. Huang, Y.-B. Cheng, R.A. Caruso, Adv. Mater. 21 (2009) 2206–2210.
4. Q. Wang, S. Ito, M. Grätzel, F. Fabregat-Santiago, I. Mora-Seró, J. Bisquert, T. Bessho, H. Imai, J. Phys. Chem. B 110 (2006) 25210–25221.
5. Y. Chiba, A. Isalam, R. Komiya, N. Koide, L. Han, Appl. Phys. Lett. 88 (2006) 223505–1–223505–3.
6. M. Grätzel, J. Photochem. Photobiol. A 164 (2004) 3–14.
7. H.J. Koo, Y.J. Kim, Y.H. Lee, W.I. Lee, K. Kim, N.-G. Park, Adv. Mater. 20 (2008) 195–199.
8. M. Grätzel, Nature 414 (2001) 338–344.
9. M. Grätzel, Inorg. Chem. 44 (2005) 6841–6851.
10. C.-S. Chou, R.-Y. Yang, C.-K. Yeh, Y.-J. Lin, Powder Technol. 194 (2009) 31–42.
11. K. Vignesh, A. Suganthi, M. Rajarajan, S.A. Sara, Powder Technol. 224 (2012) 331–337.
12. J. Bisquert, D. Cahen, G. Hodes, S. Rűhle, A. Zaban, J. Phys. Chem. B 108 (2004) 8106–8118.
13. Y. Tachibana, J.E. Moser, M. Grätzel, D.R. Klug, J. Durrant, J. Phys. Chem. 100 (1996) 20056–20062.
14. M. Grätzel, Coord. Chem. Rev. 111 (1991) 167–174.
15. M. Grätzel, Curr. Opin. Colloid Interface Sci. 4 (1999) 314–321.
16. M. Adachi, Y. Murata, M. Harada, S. Yoshikawa, Chem. Lett. (2000) 942–943.
17. S. Ngamsinlapasathian, S. Pavasupree, Y. Suzuki, S. Yoshikawa, Sol. Energ. Mat. Sol. Cells 90 (2006) 3187–3192.
18. S. Hore, P. Nitz, C. Vetter, C. Prahl, M. Niggemann, R. Kern, Chem. Commun. (2005) 2011–2013.
19. H.-J. Koo, J. Park, B. Yoo, K. Yoo, K. Kim, N.-G. Park, Inorg. Chim. Acta 361 (2008) 677–683.
20. C.J. Barbé, F. Arendse, P. Comte, M. Jirousek, F. Lenzmann, V. Shklover, M. Grätzel, J. Am. Ceram. Soc. 80 (1997) 3157–3171.
21. N.-G. Park, J. van de Lagemaat, A.J. Frank, J. Phys. Chem. B 104 (2000) 8989–8994.
22. S.-C. Yang, D.-J. Yang, J. Kim, J.-M. Hong, H.-G. Kim, I.-D. Kim, H. Lee, Adv. Mater. 20 (2008) 1059–1064.
23. Y. Kondo, H. Yoshikawa, K. Awaga, M. Murayama, T. Mori, K. Sunada,

S. Bandow, S. Iijima, Preparation, Langmuir 24 (2008) 547–550.
24. W. Shao, F. Gu, C. Li, M. Lu, Inorg. Chem. 49 (2010) 5453–5459.
25. Y. J. Kim, M. H. Lee, H. J. Kim, G. Lim, Y. S. Choi, N.-G. Park, K. Kim, W. I. Lee, Adv. Mater. 21 (2009) 1–6.
26. H.-J. Kim, J.-D. Jeon, S.-Y. Kwak, Powder Technol. 243 (2013) 130–138.
27. D. Cahen, G. Hodes, M. Grätzel, J.F. Guillemoles, I. Riess, J. Phys. Chem. B 104 (2000) 2053–2059.
28. H.J. Koo, J. Park, B. Yoo, K. Kim, N.G. Park, Inorg. Chim. Acta 361 (2008) 166–683.
29. H. Yu, S. Zhang, H. Zhao, G. Will, P. Liu, Electrochim. Acta 54 (2009) 1319–1324.

Chapter 5

Highly Efficient Dye-Sensitized Solar Cells Containing Bowl-Shaped TiO_2 Nanorod Clusters with Multiple Light Scattering Ability

5.1 Introduction

Since the first report of dye-sensitized solar cells (DSSCs) by Grätzel *et al.* [1] in 1991, DSSCs have been regarded as next generation solar cells because of their high efficiency, low cost, and facile fabrication process [2-5]. In the last decade, there have been numerous attempts with diverse methods to enhance the performance of DSSCs [6-14]. The energy conversion efficiency of DSSCs has reached greater than 12% using mesoporous TiO_2 as photoelectrode materials [15]. Generally, a TiO_2 photoelectrode is one of the most important prerequisites for efficient DSSCs [16, 17]. Based on photovoltaic mechanism, to improve the conversion efficiency of a DSSC, on one hand, once can increase the internal surface of the TiO_2 photoelectrode for more dye adsorption to improve optical absorption of the photoelectrode [18]. On the other hand, one can employ 1-D nanostructures to provide a direct path for electron diffusion and thus promote excellent charge separation, fast charge injection, and transport in DSSCs [19, 20]. In addition to the aforementioned ways of

enhancing DSC performance, light scattering is another important method that has been adopted to improve the conversion efficiency of DSCs [21]. The basic idea of a light scattering method is to confine the light propagation and extend the traveling distance of light within the photoelectrode film so as to increase the opportunity of the photons to be absorbed by the dye molecules, and in this way, to enhance the light harvesting efficiency of the photoelectrode as well as the conversion efficiency of the DSSCs.

Among these improvements, the light-scattering effect has drawn much attention since it is a simple method for enhancing the light absorption. As TiO_2 electrode is normally made up of nanoparticles of 10-25 nm size, it remains transparent to the visible region of solar spectrum. In this scenario, solar energy is only partially harvested by the active layer. Inclusion of large particles of size comparable to the wavelength of incident light encourages better light scattering in DSCs especially from the red part of the solar spectrum. The basic concept of light-scattering effect was introduced by Usami in 1997 [22]. He suggested a new photoelectrode structure, which uses an overlayer made up of a large particle semiconductor electrode on top of a layer made up of a small particle semiconductor electrode; the light scattered by the over-layer caused an increase in the light absorption. In early days, many studies have been focused on the evaluation of the light-scattering effect in the DSC by using various simulation methods based on the Mie theory [23]. Recently, there have

been attempts to improve light-harvesting capability of the electrode film by utilizing optical enhancement effects i.e. additionally admixing submicrometer-sized TiO_2 particles as the light-scattering centers and/or directly introducing a light-scattering layer in the photoelectrode. However, the introduction of larger scattering particles inevitably lowers the internal surface area of the film, increasing the electron diffusion length, and thus resulting in the lower cell performance. To overcome this weakness, the bifunctional TiO_2 structures such as mesoporous microspheres [24], hollow microspheres [25], and mirror-like structures [26] have been explored as they can increase the dye loading and harvest the incident light within the electrode as well. Although lots of such attempts have been made, it is still difficult to satisfy all the criteria given earlier for that single scattering layer of TiO_2 particles. For this reason, it is necessary to design novel structures which will be used in scattering layers. The new structures not only possess a high surface area for the efficient dye adsorption and the fast electron transport, but also provide a superior light-scattering effect for the high light harvesting.

To fully accommodate all these favorable characteristics, we were motivated to develop a novel bowl-shaped scattering layer with TiO_2 nanorod clusters as an over-layer for DSSC photoelectrodes. In the electrode we made, the cluster had mesoporous structures with a relatively larger surface area compared to the conventional one, hence this unique shape

of the TiO_2 nanorods-based cluster provided a direct pathway for the electron transport as well as an enhanced aggregation-induced light scattering for the range of visible-light wavelength. The DSC based on bowl TiO_2 scattering layer exhibits remarkably enhanced photovoltaic properties compared with that based on spherical TiO_2 scattering layer. It is shown that these TiO_2 materials have a good energy conversion properties for the DSSCs due to the multi-light scattering inside. Overall, we have provided a particular method to prepare hierarchical TiO_2 nanomaterials hat can integrate morphologies of spheres and bowls with high specific surface area and high pore volume. The enhanced light scattering ability of bowl-shaped TiO_2 cluster by multiple scattering makes it tremendously attractive for applications ranging from water purification to hydrogen generation. In addition, the simplicity of the current process to produce bowl-shaped cluster makes it attractive for large-scale production. To the best of our knowledge, this is the first demonstration of such bowl scattering layer based on TiO_2 nanorods for coordinately promoting charge-collection efficiency and light harvesting capability.

5.2 Experiments

5.2.1 Materials

Titanium (IV) butoxide (TTBu, $Ti(OBu)_4$), lauric acid (LA), cyclohexane, ethanol were all purchased from Sigma-Aldrich and used as received without further purification. *cis*-diisothiocyanato-bis(2,2-bipyridyl-4,4-dicarboxylato) ruthenium(II) bis (tetrabutylammonium) (D719), fluorine doped tin oxide (FTO) substrate, Ti-Nanoxide D pastes was purchased from Solaronix. The water used in all syntheses was distilled and deionized.

5.2.2 Synthesis of LA@TiO_2 complexes

The synthesis of LA@TiO_2 complexes was accomplished by solvothermal treatment. TiO_2 nanorod was synthesized by the following procedure. A cyclohexane containing lauric acid was heated at 200 ^oC followed by addition of TTBu under vigorous stirring. For the low titanium precursor concentration experiments, 1.0 mmol of TTBu were used. In the high titanium precursor concentration experiment, 4.0 mmol of TTBu was used.

5.2.3 Preparation of TiO_2 clusters using electrospray process

The film consisting of TiO_2 nanocrystallites (NC) were coated on top of fluorine doped tin oxide (FTO) glass by the doctor-blade printing method, using

a Ti-Nanoxide D, followed by a sintering procedure at 500 ^{o}C for 30 min under air. The NC film were coated on the FTO glass with an identical thickness for all samples. The various solutions containing the 20 wt% TiO_2 nanorods were loaded into a plastic syringe which was connected to a high voltage power supply (ESP200RD, NanoNC). Then, the dispersed TiO_2 nanorods solutions were electrosprayed directly onto the NC coated FTO glasses. To prepare the electrosprayed clusters, the electric field of 20 kV was applied between the metal orifice and the substrate. The feed rate was controlled by a syringe pump at 5 ml/hr. In order to form a uniform thickness in an area, the nozzle and the substrate were placed on the motion control system with a microprocessor. The resultant film was heated in air at 500 ^{o}C for 30 min.

5.2.4 Assembly of the DSSCs

The as-prepared TiO_2 electrodes were immersed in an ethanolic solution containing a ruthenium sensitizer dye, 3×10^{-4} M D719 for 12 h. The platinized counter electrode was placed on top of the dye-coated TiO_2 photo-electrode sealed with a Surlyn film (25 μm thick, DuPont), and the electrolyte, which was composed of 1-butyl-3-methyl-imidazolium iodide (BMII, 0.7 M, Merck), I_2 (0.03 M), guanidinium thiocyanate (GSCN, 0.1 M, Aldrich), and 4-tert-

butylpyridine (TBP, 0.5 M, Aldrich) in acetonitrile and valeronitrile (85:15 v/v), was injected through a hole in the counter electrode.

5.2.5 Characterization

The structural development of the various nanocrystals were checked using high-resolution transmission electron microscopy (HR-TEM, JEOL JEM-2000 FX II). The surface features and morphologies of the electrosprayed clusters were investigated by using field-emission scanning electron microscopy (FE-SEM, JEOL JSM-6330F). The specific surface areas and pore size distributions of the clusters were characterized by analyzing the N_2 adsorption and desorption isotherms obtained at 77 K with a Micrometrics ASAP 2000 equipment. All the samples were degassed at 200 °C and 10^{-6} Torr for 10 h prior to these measurements. The surface areas were calculated with the Brunauer-Emmett-Teller (BET) equation, and pore-size distributions were determined from the adsorption and desorption branches by using the Barrett-Joyner-Halenda (BJH) formula. Diffused reflectance spectroscopy was performed with a Lamba 25 instrument manufactured by Perkin Elmer.

Photovoltaic measurements were conducted by illuminating the DSSCs with light from a 450 W Xe lamp that had been directed through an AM 1.5 solar simulator. The intensity of the simulated light was calibrated by using a Si

reference solar cell equipped with a BK7 filter to approximate AM 1.5, 100 mW cm^{-2} global radiation. The photovoltaic characteristics of the DSSCs were obtained by applying an external potential bias to the cells and measuring the generated photocurrent with a Keithley 2400 source meter. IPCEs were measured as a function of wavelength from 350 to 800 nm using a specially designed IPCE system for dye-sensitized solar cells (PV Measurements, Inc.). A 75 W xenon lamp was used as the light source for generating a monochromatic beam. Calibration was performed using a NIST-calibrated silicon photodiode as a standard. IPCE values were collected at a low chopping speed of 5 Hz. The electron transport time and electron recombination lifetimes were measured by intensity-modulated photocurrent spectroscopy (IMPS) and intensity-modulated photovoltage spectroscopy (IMVS). A diode laser with variable power and modulation control (Coherent Lab-laser, 10 mW, 635 nm) was used as the light source for these studies. Illumination was always incident on the photoelectrode side of the cells. The intensity was measured using a calibrated Si-photodiode. IMVS was performed under open-circuit conditions. The output of the cell was connected directly to a frequency response analyzers (FRA) Solatron 1260 Impedance (Gain-Phase Analyzer). IMPS was performed by connecting the cell via a potentiostat amplifier (EG&G PAR 273) to the FRA. During the IMVS and IMPS measurements, the cell was illustrated with sinusoidally modulated light having a small ac component (10% or less of the

dc component). Diffused reflectance spectras of the clusters were collected from a Cary 5000 UV-Vis-NIR spectrophotometer with an integrating sphere accessory (Internal DRA-2500).

5.3 Results and Discussion

5.3.1 Synthesis of LA@TiO_2 complexes

The structural development of the various nanocrystals was monitored by high-resolution transmission electron microscopy (HR-TEM), and the images are presented in Fig. 5.1 [27]. At low TTBu concentrations, diamond shaped nanocrystals were obtained (Fig. 5.1(a)). Increasing the amount of TTBu concentration gave nanorods with a diameter of about 3 nm and length of about 25 nm, as shown in Fig. 5.1(b). The HR-TEM analysis indicates that the rods obtained by increasing the TTBu concentration are elongated along the <001> direction. As shown in Fig. 5.1(c), the rods exhibit a zigzag pattern of {101} faces. Rod formation is realized through anisotropic crystal growth, which is achieved when the surface free energies of the various crystallographic planes differ markedly. The use of different surface ligands that bind selectively to the respective surface planes has been already been demonstrated as a suitable approach to induce rod formation in a controlled manner [28]. In our system, the unidirectional growth of TiO_2 nanorods is attributed to the selective adsorption of LA through its carboxylate groups onto under-coordinated Ti surface atoms, resulting in the formation of bidentate surface complexes that play an imprtant role in controlling the growth direction. The observed anisotropic growth patterns indicate that the injection of the TTBu precursor into the reaction solution induces the formation of TiO_2 seeds terminated by

{001} faces with high surface energy and {101} faces with relatively low surface energy [29, 30]. The shape of the TiO_2 nanoparticles is governed by the competition between the surface free energies of the {101} and {001} faces and thus the ratio of the growth rates of the <001> and <101> directions. By selectively chelating to the {101} faces, the effect of carboxylate group of LA is to slow the growth rate of this face. As a result, because growth of the <001> direction is promoted without simultaneously facilitating that in the <101> direction, anisotropic growth is observed instead of isotropic growth, as shown in Fig. 5.1(d).

X-ray diffraction (XRD) was used to further investigate the crystal structure and growth of TiO_2 nanorods. Fig. 5.2 shows the XRD patterns of the TiO_2 nanorods. The TiO_2 nanorods produce several relatively well-defined reflection peaks in the 2θ region of 20–70^o, that are quite similar to those for pure-phase anatase TiO_2 particles reported by other groups, which indicates that the prepared TiO_2 nanorods have an anatase crystal structure (JCPDS card No. 73-1764). No peaks corresponding to any other phases were observed. Comparing the intensity of the (004) peak of this sample to that of the standard sample shown in JCPDS card, it was found that the relative intensity of (004) had increased [30]. This implied that crystal growth of the TiO_2 nanorod occurs along the [001] direction, consistent with the HR-TEM images in Fig. 5.1. The TiO_2 nanorods were characterized by means of IR spectroscopy. In Fig. 5.3 the

typical IR spectra in the region between 4000 and 500 cm^{-1} of lauric acid-functionalized TiO_2 nanorod ($LA@TiO_2$) sample before and after calcination at 500 ^oC for 30 min are presented. The spectrum of pure lauric acid is shown for a comparison. Above 2000 cm^{-1} , in spectra of lauric acid, the broad absorption band at around 3400–2400 cm^{-1} displayed by the lauric acid corresponds to the stretching vibration of the terminal hydroxyl (–OH) group. Superimposed are antisymmetric and symmetric C–H stretching vibrations (2917 and 2850 cm^{-1}, respectively) of the $–CH_2–$ groups in the hydrocarbon moiety. Below 2000 cm^{-1}, absorption bands at 1739 and 1280 cm^{-1} are due to C=O stretching motion and coupled C–(OH) stretching and C–O–H bending motions, respectively [32]. Many intense bands are observed in the range 100–1500 cm^{-1}, which are associated with methylene ($–CH_2–$) and methyl ($–CH_3$) group bending. FT-IR spectrum of the $LA@TiO_2$ before calcination confirms the presence of lauric acid on the surface of the TiO_2 nanorods. Above 2000 cm^{-1}, TiO_2 nanorods before calcination exhibits the intense antisymmetric and symmetric C–H stretching vibrations (2919 and 2850 cm^{-1}, respectively) of the $–CH_2–$ groups in the hydrocarbon moiety. Below 2000 cm^{-1}, the COO– antisymmetric and symmetric stretching motions (two characteristic bans at 1517 and 1436 cm1 , respectively) of carboxylate anions complexed with surface Ti centered dominate in the spectra of the $LA@TiO_2$. The peak at 1648 cm^{-1} can be assigned to C=O stretching vibration. The band is no longer the

most intense band in the spectrum. The shift toward a lower intensity arises most likely as a result of the weakened C=O bond resulting from the interaction with the surface Ti atoms. The characteristic vibrations of the inorganic Ti–O–Ti network in titanium dioxide can be seen in the spectra below 950 cm^{-1}. These results indicate that the surfaces of the TiO_2 nanorods are modified by lauric acids. It is known that carboxylic acids bind very strongly to TiO_2 (001) facets, and thus acts as a surface selective surfactant [33]. It was deduced that carboxylic acid interacts with the intrinsic anisotropic features of TiO_2 and induces variation in the shapes of TiO_2 nanoparticles. In addition, carboxylic acid acts as a stabilizer of TiO_2 nanoparticles in organic solvents. Our conclusion about the coordination effects of lauric acid is supported by the dispersibility of the TiO_2 sample, in which lauric acid caps the surfaces of the TiO_2 nanoparticles; the as-synthesized TiO_2 was found to be redispersible in the solvent and did not aggregate. Thus, these LA@TiO_2 can be prepared in an electrospray process without further physical or chemical dispersion techniques, such as bead mill or hydrothermal treatment. After calcination of the TiO_2 nanorods at 500 ^oC, the peaks from lauric acid are absent which demonstrates the complete removal of lauric acid from the surfaces of the TiO_2 nanorods. When we sintered the product at a high temperature to remove the surface-coordinated lauric acid, the TiO_2 nanorods were no longer dispersible.

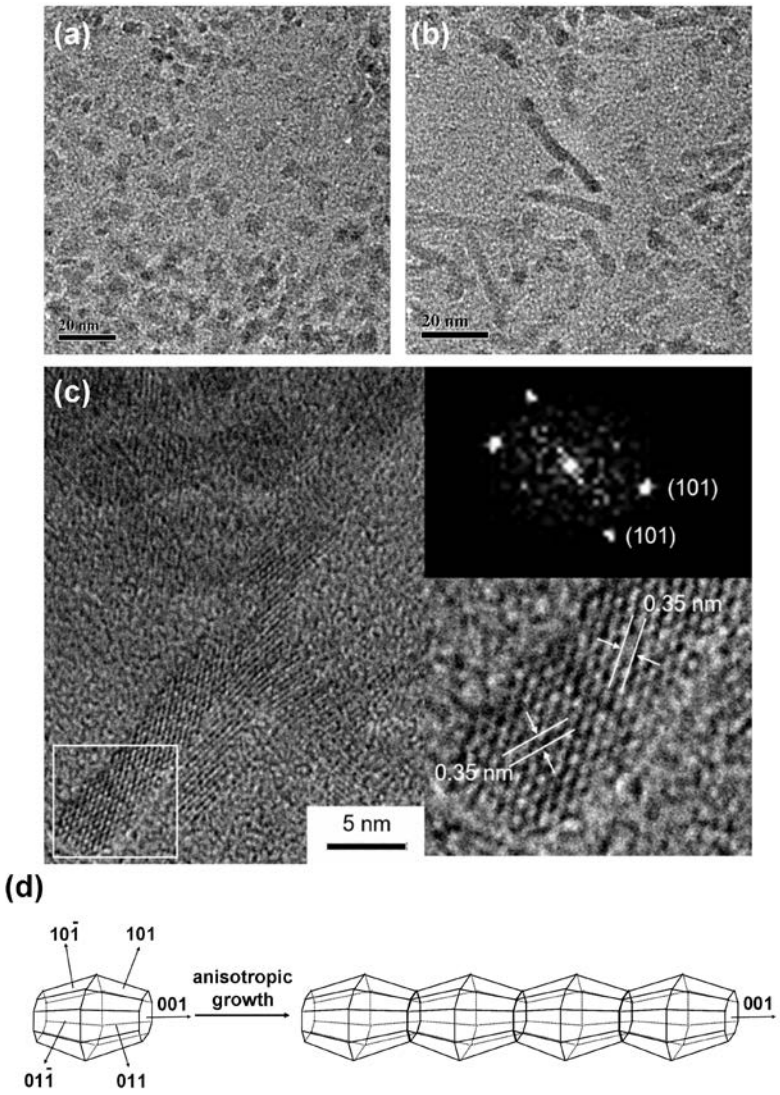

Fig. 5.1. TEM images of LA@TiO_2 obtained with different amounts of TTBU: (a) 1 and (b) 4 mmol. (c) HR-TEM image of LA@TiO_2 nanorods, with corresponding fast Fourier transform (FFT) diffractogram and individual LA@TiO_2 nanorod. (d) Schematic representation showing the anisotropic growth of LA@TiO_2.

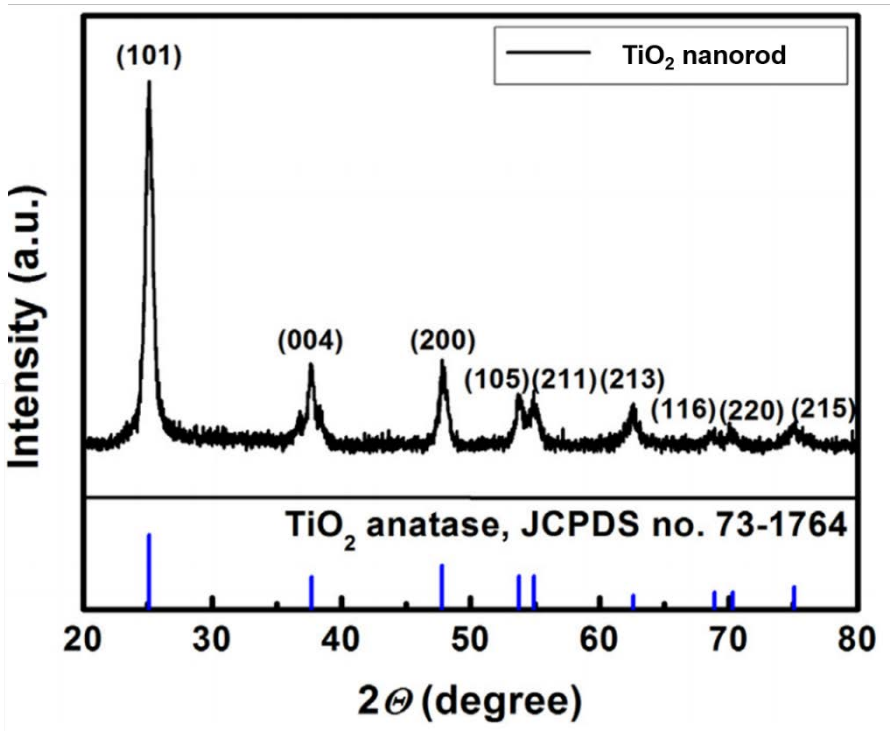

Fig. 5.2. X-ray diffraction patterns of TiO_2 nanorods.

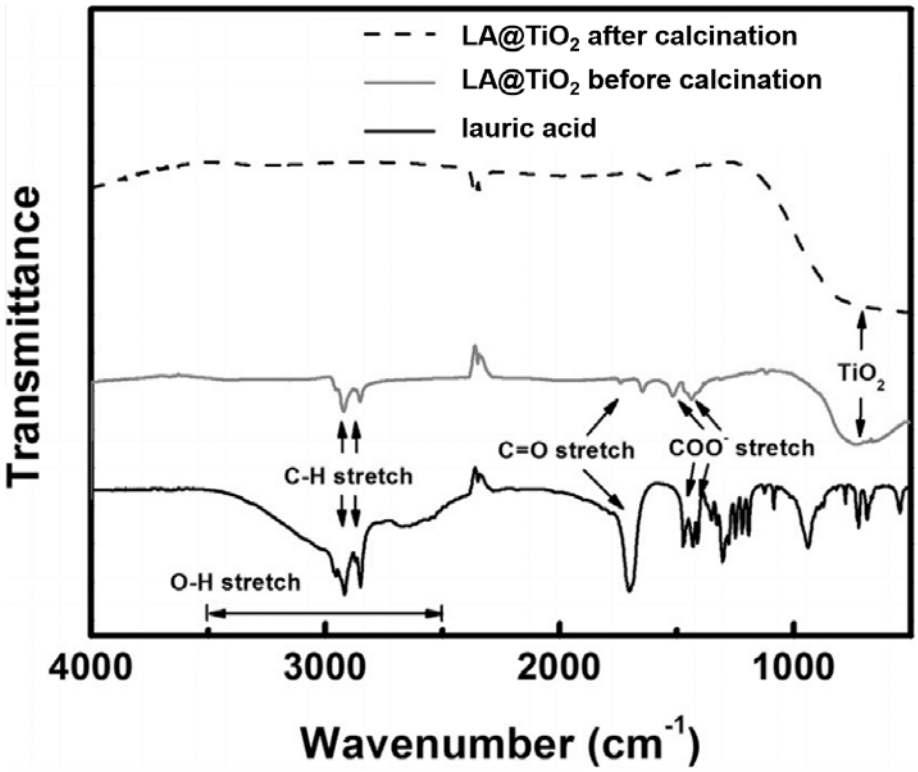

Fig. 5.3. FT-IR spectra of lauric acid and LA@TiO_2 before and after calcination.

5.3.2 TiO_2 clusters using electrospray process

The effect of the vapor pressure of the solvent on the morphologies of the electrosprayed in the LA@TiO_2 complexes was studied. Fig. 5.4 shows the scanning electron microscopy (SEM) images of electrosprayed materials with different morphologies [27]. As illustrated in Fig. 5.4 (a) and (b), when the solvent had a low vapor pressure, like pure water (24.00 mmHg), the solvent did not evaporate fully before the droplet reached the substrate, resulting in the deposition of tiny dispersed TiO_2 particles. A solvent with moderate vapor pressure, like ethanol (58.71 mmHg), evaporated when it sat on the substrate, producing spherical TiO_2 clusters (S-TiO_2) with diameters from 300 to 600 nm (Fig. 5.4 (c) and (d)). A solvent with relatively high vapor pressure, cyclohexane (97.83 mmHg) in the case, gave bowl-shaped clusters (B-TiO_2) with the diameters ranging from 300 to 700 nm (Fig. 5.4 (e) and (f)). It is interesting that structures with a bowl shape formed because this morphology has seldom been reported to date. When a solvent with a very high vapor pressure was used, the solvent droplet tended to evaporate before the droplet was fully sprayed, which finally incurred blockage of the nozzle tip of the spraying machine, so no particles were deposited on the substrate.

In accordance with these results, a proposed mechanism for the change of the cluster morphology depending on the solvent vapor pressure during the

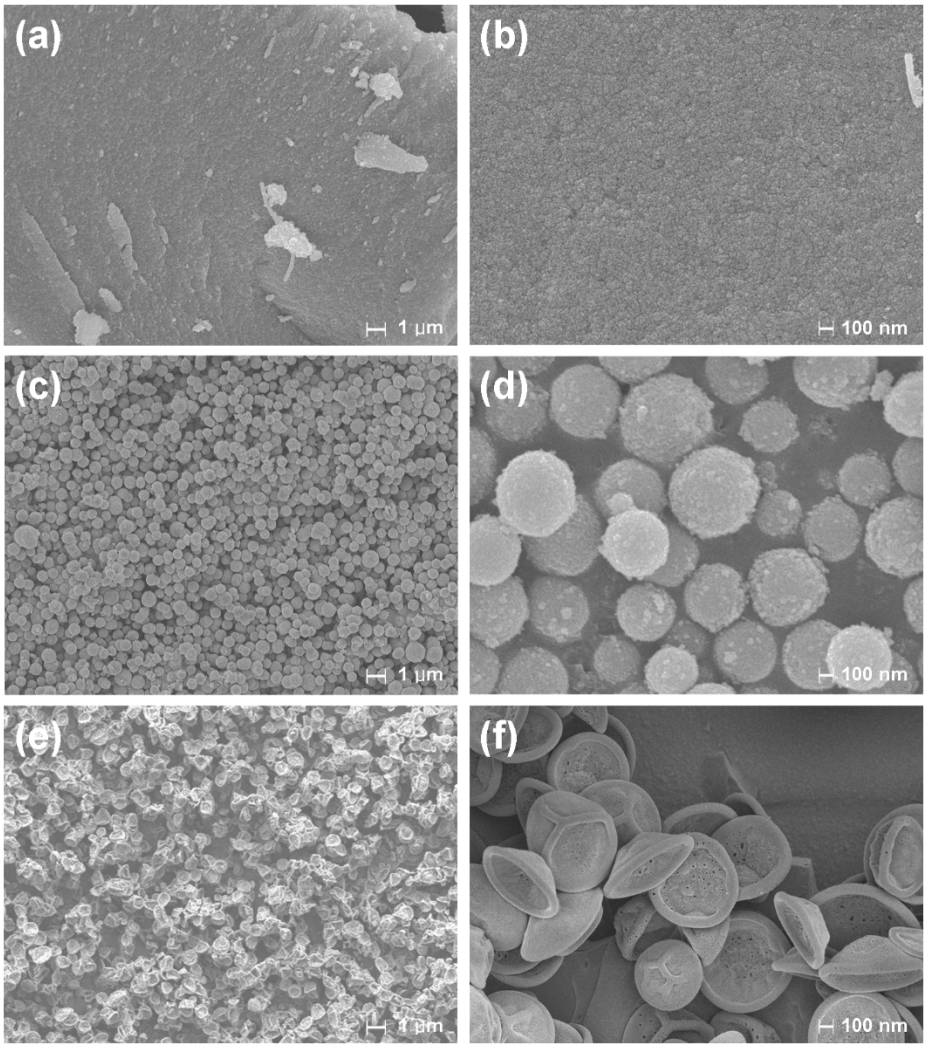

Fig. 5.4. FE-SEM images of electrosprayed TiO_2 with different solvents of (a and b) water, (c and d) ethanol, and (d and e) cyclohexane.

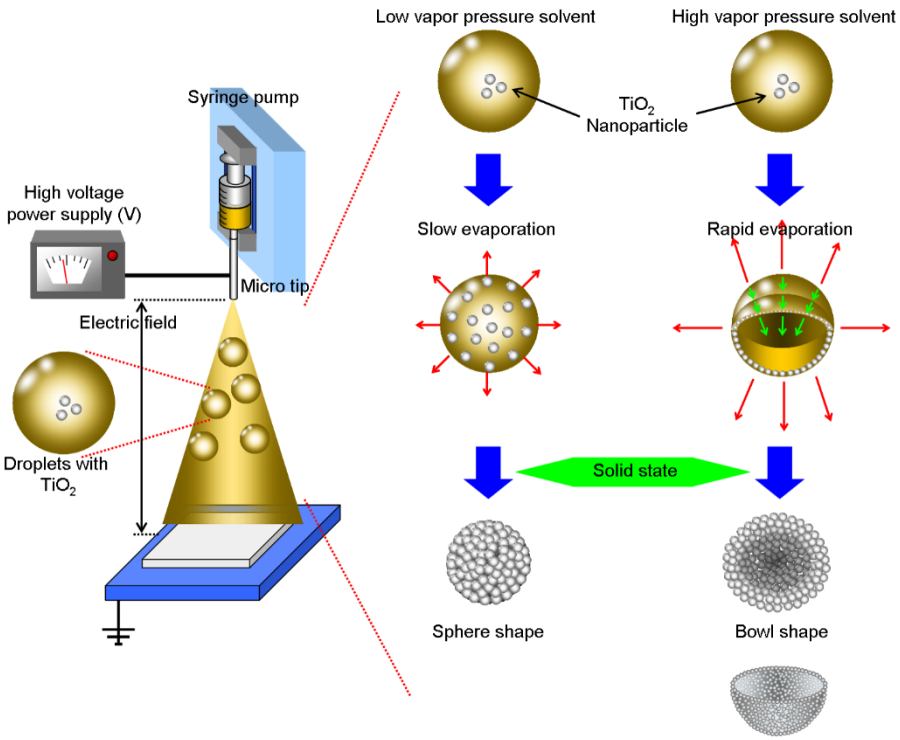

Fig. 5.5. Proposed mechanism for the formation of sphere- and bowl-shaped TiO_2 clusters via electrospray process.

electrospray process is schematically illustrated in Fig. 5.5. In the case of a solvent with low vapor pressure, the solvent in the electrosprayed droplet does not fully evaporated when the droplets land on the substrate. As a result, the particles in the droplet are deposited without controlled aggregation. For a solvent with moderate vapor pressure, the solvent can evaporate fully, which leads to the formation of spherical clusters as the spherical droplets slowly shrink during solvent evaporation. In contrast, when a solvent with a relatively high vapor pressure is used, the droplet does not retain its spherical shape during the electrospraying process because the solvent rapidly evaporates. This situation gives rise to the bowl-shaped clusters.

The Brunauer-Emmett-Teller (BET) specific surface areas and pore size distributions of the S-TiO_2, B-TiO_2, and NC obtained from the electrospray process were evaluated from their respective nitrogen adsorption − desorption isotherms (Fig. 5.6 and Table 5.1). In contrast to the NCs, the clusters displayed specific hysteresis loops between the adsorption and desorption isotherms over a P/P_0 range of approximately 0.5-0.8, which can be classified as type-IV isotherms with H2-type hysteresis [34]. This reveals that these materials have a mesoporous structure. The BET specific surface areas of the S-TiO_2, B-TiO_2, and NC were 113.57 m^2/g, 93.10 m^2/g, 48.02 and m^2/g, respectively. Although the B-TiO_2 had a smaller specific surface area than the S-TiO_2, both samples exhibited surface areas at least twice that of the NC. The pore size distributions

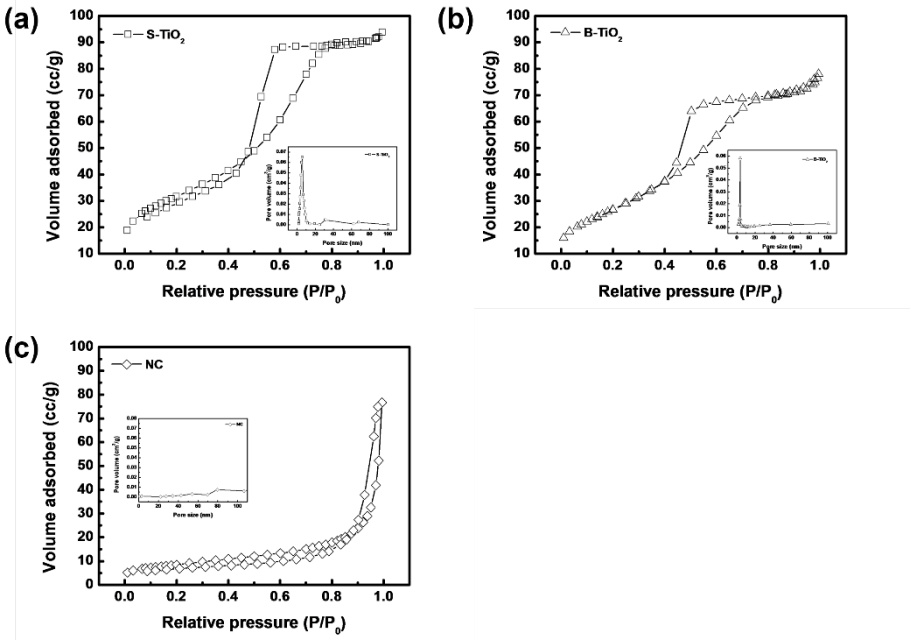

Fig. 5.6. N_2 adsorption-desorption isotherms for (a) S-TIO_2, (b) B-TiO_2, and (c) NC, and the corresponding pore-size distributions (inset).

Table 5.1. Specific surface area and average pore size of the samples.

Samples	Specific surface area (m^2/g)	Average pore size (nm)
S-TiO_2	113.57	4.04
B-TiO_2	93.10	3.68
NC	48.02	4.31

of the samples were evaluated by the Barrett-Joyner-Halenda (BJH) method (insets of Fig. 4). The average pore size of the S-TiO_2 and B-TiO_2 were 4.04 nm and 4.68 nm, respectively, with narrow pore size distributions. The area of an N719 dye molecule on the surface of TiO_2 is calculated to be 1.6 nm^2/molecule. Accordingly, these results suggest that the clusters can be readily accessed by dye molecules. Conversely, the NC did not show a clear pore structure. These SEM and N_2 adsorption-desorption results indicate that the clusters can not only act as light scattering centers, but also provide a large number of dye adsorption sites.

5.3.3 Photovoltaic performance

Fig. 5.7 (a) shows typical photocurrent density-photovoltage (*J*-*V*) curves for the resulting DSSCs containing the nanomaterials, and the related photovoltaic parameters of the three kinds of DSSCs with S-TiO_2 (S-TiO_2 cell), B-TiO_2 (B-TiO_2 cell), and NC (NC cell) are summarized in Table 5.2. Because the NC is too small to sufficiently scatter visible light, the NC cell showed the lowest energy conversion efficiency (η) of 5.32% with a short-circuit current density (J_{sc}) of 13.32 mA/cm^2 and the open-circuit voltage (V_{oc}) of 0.68 V. Introducing the electrosprayed clusters as the light scattering layer caused both J_{sc} and V_{oc} to increase considerably, while the fill factor (FF) of the cells was not appreciably changed. The increase of V_{oc} may be caused by charge

recombination being suppressed by the scattering layer, as explained later. The higher J_{sc} is probably related to the amount of adsorbed dye and/or light scattering. Using the B-TiO_2 as a scattering layer, a high η of 9.13% was achieved without any other post-treatment. This value is 1.7 times that of the NC cell (5.32%) and 1.2 times that of the S-TiO_2 cell (7.14%). To analyze in more detail the improved performance of the cell with B-TiO_2, incident photon-to-current efficiency (IPCE) measurements were carried out. Fig. 5.7 (b) displays the IPCE spectra for the cells as a function of wavelength measured under short circuit conditions. IPCE spectra are determined by the incident light absorption efficiency of the dye molecules, the quantum yield of electron injection, and the efficiency of the collection of injected electrons at the substrate, which is strongly affected by the surface area and morphology of the photoelectrode. The IPCE values of the cells with the clusters were higher than that of the NC cell over the whole spectral range of 300-700 nm, which is in good accordance with the relatively high J_{sc} of the cells with the clusters, as shown in Fig. 5.7 (a). The higher IPCE values of the cells with S-TiO_2 and B-TiO_2 at short wavelength region than that for the cell with NC was mainly attributed to their higher dye-loading capacities [35]. Meanwhile, in the long wavelength region, the higher IPCE values of the cells with the clusters than that of the one with NC could be ascribed to their enhanced light scattering capacities, which promoted the light harvesting of the dye molecules in this

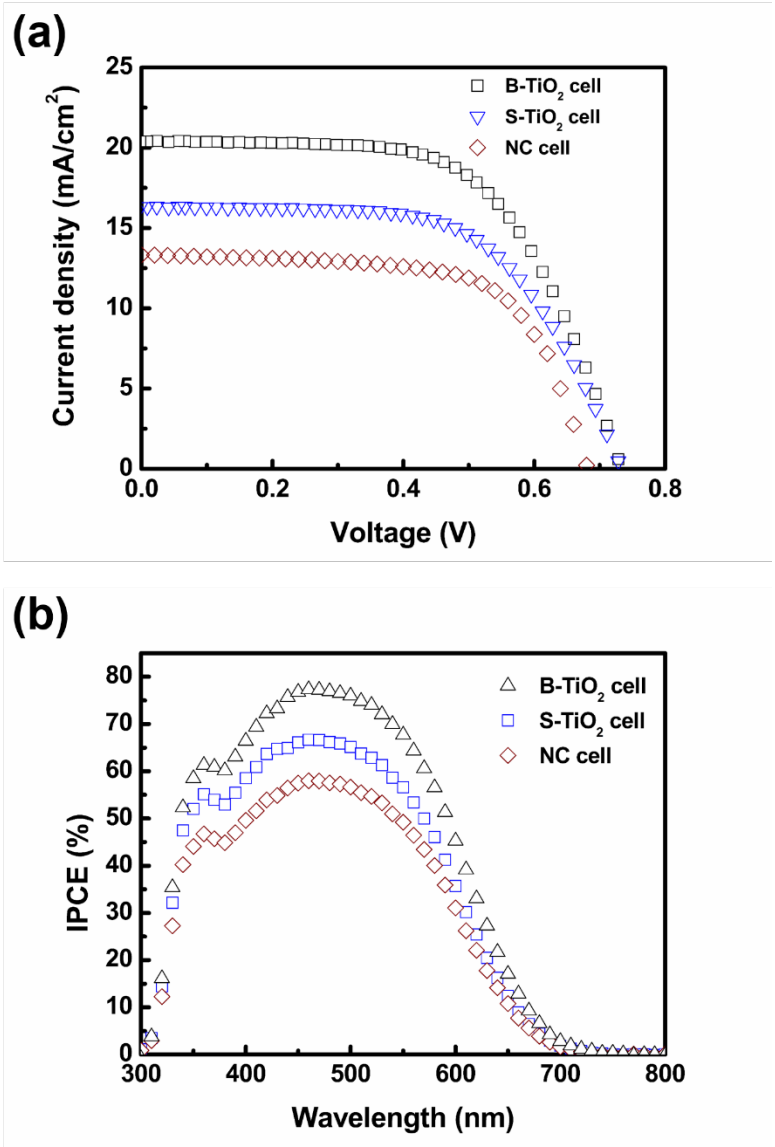

Fig. 5.7. *J-V* curves for the resulting DSSCs containing the nanomaterials and (b) IPCE spectra for the cells (S-TiO_2 cell, B-TiO_2 cell, and NC cell).

Table 5.2. J-V parameters of S-TiO_2 cell, B-TiO_2 cell, and NC cell.

	V_{oc} (V)	J_{sc} (mA/cm^2)	FF	η
S-TiO_2 cell	0.73	16.31	0.60	7.14
B-TiO_2 cell	0.73	20.39	0.61	9.13
NC cell	0.68	13.92	0.58	5.32

region [36, 37]. The B-TiO_2 cell exhibited the highest IPCE, indicating that B-TiO_2 is a more efficient structure than the S-TiO_2 for scattering light. We note that the crystallinities of the electrosprayed clusters were similar to each other because they contained identical TiO_2 nanorods. The specific surface area and pore size of the clusters were also comparable. In addition, we found that the amount of the adsorbed dye per unit area of the particles was similar as well (S-TiO_2 cell = 145.75 μmol/cm^{-2}, B-TiO_2 cell = 128.54 μmol/cm^{-2}). These results suggest that the different photovoltaic properties of the DSSCs with the clusters originated from a structural factor rather than crystallinity, pore size distribution, specific surface area, or dye-loading capacity.

To further shed light on the electron transport and electron lifetime in the cells, intensity-modulated photovoltage spectroscopy (IMVS) and intensity-modulated photocurrent spectroscopy (IMPS) were performed because they have been proven as powerful techniques to investigate the dynamics of inherent electron transport in DSSCs (Fig. 5.8). IMVS and IMPS measurements of the S-TiO_2 cell, the B-TiO_2 cell, and the NC cell were conducted at different light intensities. The electron transport time τ_d (or lifetime τ_r) for each cell was calculated from the expression $\tau_d = 1/2\pi f_{IMPS}$ ($\tau_r = 1/2\pi f_{IMVS}$), where f_{IMPS} (or f_{IMVS}) is an imaginary component. The diffusion coefficient D was calculated from the IMPS data according to the equation $D = d^2/(2.5\tau_d)$, where d and τ_d are the thickness of the TiO_2 layer, and electron transport time ($\tau_d = 1/2\pi f_{min,\ IMPS}$)

determined from IMPS, respectively [38]. As shown in Fig. 5.8 (a), τ_r of the cells with the clusters are longer than that of the NC cell. This may be because the 1D nanorods provide a direct electron pathway and the cluster structures of the cell with the clusters lead to good connectivity of the primary particles, thus decreasing the content of trap sites [39]. A longer τ_r will lead to a higher V_{oc}, consistent with the *J-V* data. Compared with the NC cell, those with the clusters exhibit higher D, as shown in Fig. 5.8 (b). This is because the clusters possess comparable dye adsorption and better light scattering capabilities than the NC. Interestingly, in contrast to τ_r, the S-TiO_2 cell and the B-TiO_2 cell exhibited different D [40, 41]. The higher D of the B-TiO_2 cell than that of the S-TiO_2 cell indicates that the particle morphology does affect photovoltaic performance. It is believed that the bowl-shaped morphology is more favorable than the spherical one for the light multiple light scattering inside the nanostructured materials, which leads to enhanced light absorption and thus the increase of η.

To elucidate the origin of the different η of the cells, we investigated the light-scattering effect of TiO_2 using diffused reflectance spectroscopy (DRS), which is generally accepted as an efficient tool to determine light-scattering ability. The DRS data for S-TiO_2, B-TiO_2 and NC are shown in Fig. 5.9. Both electrosprayed materials exhibited high reflectance over the whole wavelength region, whereas the NC showed small reflectance. Interestingly, B-TiO_2

displayed higher reflectance than S-TiO_2. It is well known that multiple scattering readily occurs in the void of a hollow sphere [42]. Multiple scattering can also occur in the void of the bowl structure, increasing the light utilization, and resulting in the enhancement of η of the DSSCs. Thus, the B-TiO_2 was thought to promote multiple light scattering, that is, the visible lighted scattered by the bowl structure would hit the bowl structure again. As a result, η of the B-TiO_2 cell is increased because of cascade scattering of the unabsorbed visible light to the dye molecules on the TiO_2 surface. In contrast, the size of NC was too small to act as a scattering centers under visible-light irradiation, resulting in a cell with low η. The S-TiO_2 cell which did not have multiple scattering ability also exhibited lower η than B-TiO_2 cell. Considering both the photovoltaic characteristics and DRS of the cells, the bowl structure of TiO_2, which facilitated multiple light scattering, was a crucial factor to improve the performance of DSSCs.

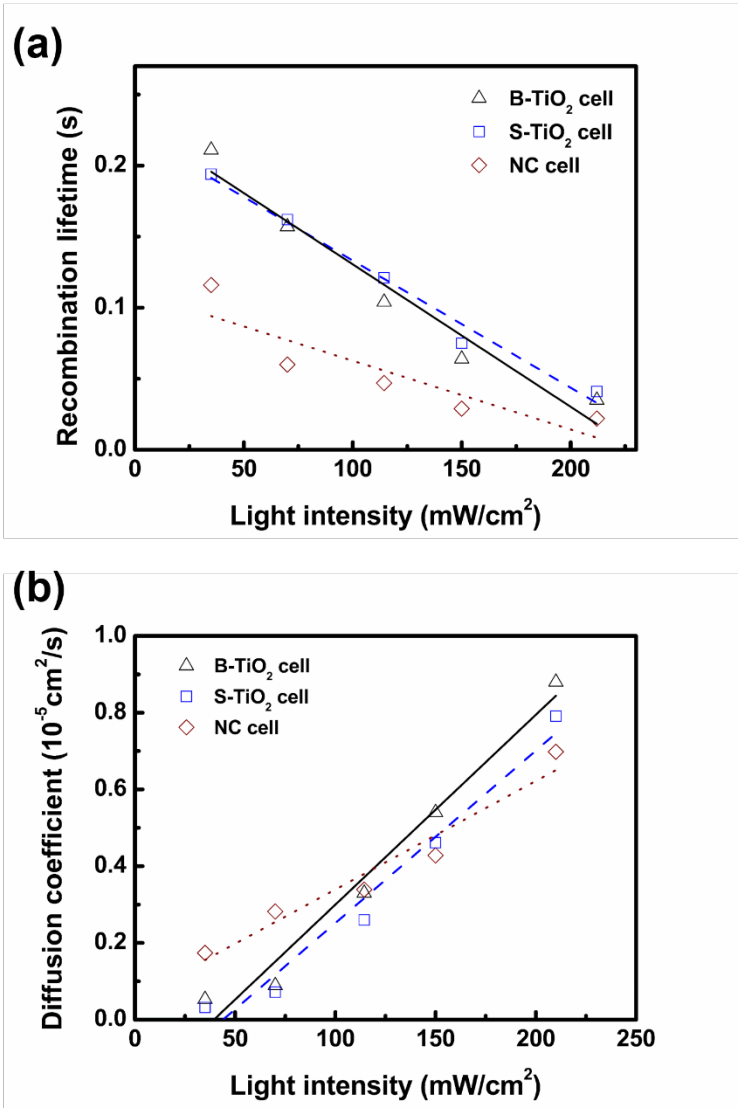

Fig. 5.8. (a) Electron lifetimes (τ_r) and (b) electron diffusion coefficients (D) of the DSSCs fabricated with the materials.

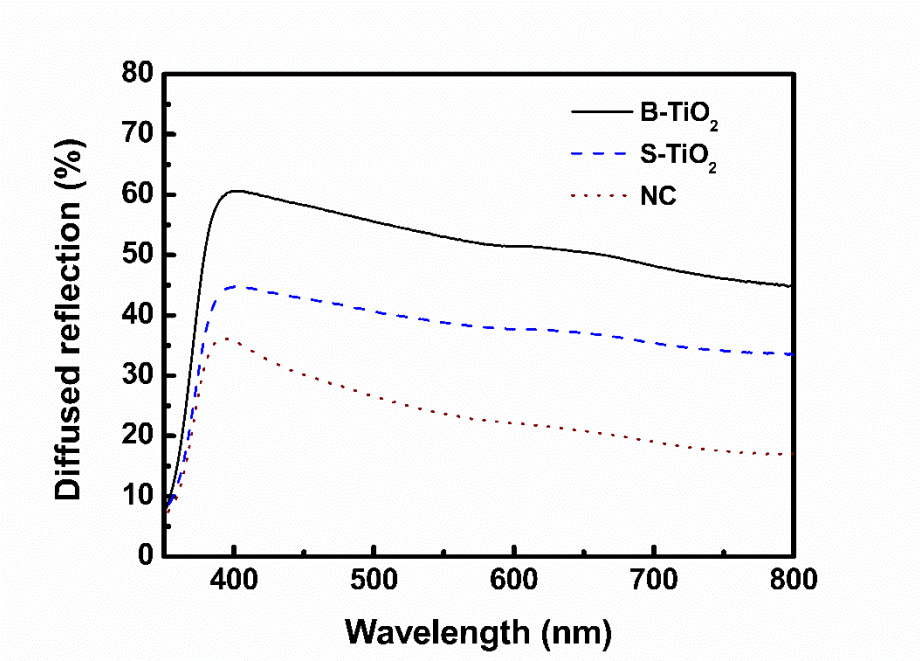

Fig. 5.9. DRS spectra of the clusters (S-TiO_2, and B-TiO_2) and NC.

5.4 Summary

In this study, we synthesized rod-shaped LA@TiO_2 complexes with a diameter of about 3 nm and length of about 25 nm. These materials were tuned from spherical TiO_2 clusters with diameters of 300 to 600 nm to bowl-shaped TiO_2 clusters with diameters of 300 to 700 nm by electrospraying using solvents with different vapor pressures. DSSCs containing with the clusters exhibited high η because of their high dye loading capacity and light scattering ability. In particular, the B-TiO_2 cells showed a higher η (9.13%) than that of the S-TiO_2 cell (7.14%). The unique bowl-shaped morphology facilitated multiple light scattering, which considerably enhanced solar cell performance. The bowl-shape TiO_2 cluster developed here represents a new design approach for high-performance solar cells using multiple light scattering and has tremendous potential for practical use in applications ranging from photocatalysis to hydrogen generation.

References

1. B. O'Regan, M. Grätzel, Nature 353 (1991) 737–740.
2. P. Wang, S. M. Zakeeruddin, J. E. Moser, M. K. Nazeeruddin, T. Sekiguchi, M. Grätzel, Nat. Mater. (2003) 402–407.
3. N. H. Damauer, G. Cerullo, A. Yeh, T. R. Boussie, C. V. Shank, J. K. McCusker, Femtosecond Dynamics of Excited-State Evolution in, Science 275 (1997) 54–57.
4. J. Xia, N. Masaki, M. Lira-Cantu, Y. Kim, K. Jiang, S. Yanagida, J. Am. Chem. Soc. 130 (2008) 1258–1263.
5. C. Y. Chen, J. G. Chen, S. Wu, J. Y. Li, C. G. Wu, K. C. Ho, Angew. Chem. Int. Ed. 47 (2008) 7342–7345.
6. G. Zhu, L. K. Pan, T. Lu, T. Xu, Z. Sun, J. Mater. Chem. 21 (2011) 14869–14875.
7. H. C. Sun, Y. H. Luo, Y. D. Zhang, D. M. Li, Z. X. Yu, K. X. Li, Q. B. Meng, J. Phys. Chem. C 114 (2010) 11673–11679.
8. J. Bisquert, F. Fabregat-Santiago, I. Mora-Seró, G. Garcia-Belmonte, S. Giménz, J. Phys. Chem. C 113 (2009) 17278–17290.
9. H. Im, S. Kim, C. Park, S. H. Jang, C. J. Kim, K. Kim, N. G. Park, C. Kim, Chem. Commun. 46 (2010) 1335–1337.
10. H. W. Chen, C. P. Liang, H. S. Huang, J. G. Chen, R. Vittal, C. Y. Lin, K. C. Wu, K.-C. Ho, Chem. Commun. 47 (2011) 8346–8348.
11. I. Mora-Seró, J. Bisquert, J. Phys. Chem. Lett. 1 (2010) 450–456.
12. S. C. Choi, S. H. Sohn, Powder Technol. 226 (2012) 157–164.
13. C.-S. Chou, F.-C. Chou, J.-Y. Kang, Powder Technol. 215–216 (2012) 38–45.
14. C.-S. Chou, R.-Y. Yang, C.-K. Yeh, Y.-J. Lin, Powder Technol. 194 (2009) 95–105.

15. A. Yella, H.-W. Lee, H. N. Tsao, C. Yi, A. K. Chandiran, M. K. Nazeeruddin, E. W.-G. Diau, C.-Y. Yeh, S. M. Zakeeruddin, M. Grätzel, Science 334 (2011) 629–634.
16. M. K. Nazeeruddin, A. Kay, I. Rodicicio, R. Humphry-Baker, E. Müller, P. Liska, N. Vlachopoulos, M. Grätzel, J. Am. Chem. Soc. 115 (1993) 6382–6390.
17. M. Grätzel, Acc. Chem. Res. 42 (2009) 1788–1798.
18. N. Martsinovich, A. Troisi, Energy Environ. Sci. 4 (2011) 4473–4495.
19. Q. F. Zhang, G. Z. Cao, Nano Today 6 (2011) 91–109.
20. Q. F. Zhang, S. Yodyingyong, J. T. Xi, D. Myers, G. Z. Cao, Nanoscale 4 (2012) 1436–1445.
21. Q. F. Zhang, C. S. Dandeneau, K. Park, D. W. Liu, X. Y. Zhou, Y. H. Jeong, G. Z. Cao, J. Nanophotonics 4 (2010) 041540.
22. A. Usami, Chem. Phys. Lett. 277 (1997) 105–108.
23. J. Ferber, J. Luther, Sol. Energ. Mat. Sol. Cells 54 (1998) 265–275.
24. W. F. Yang, F. R. Wan, Q. W. Chen, J. J. Li, D. S. Xu, J. Mater. Chem. 20 (2010) 2870–2876.
25. H. J. Koo, Y. J. Kim, Y. H. Lee, W. I. Lee, K. Kim, N. G. Park, Adv. Mater. 20 (2008) 195–199.
26. H. Yu, Y. Bai, X. Zong, F. Tang, G. Q. M. Lu, L. Wang, Chem. Commun. 48 (2012) 7386–7388.
27. H. –J. Kim, J. –D. Jeon, J. W. Chung, S. –Y. Kwak, Microporous Mesorposous Mat. 198 (2014) 170–174.
28. M. N. Thhir, P. Theato, P. Oberle, G. Melnyk, S. Faiss, U. Kolb, A. Janshoff, M. Stepputat, W. Tremel, Langmuir 22 (2006) 5209–5212.
29. R. L. Penn, J. F. Banfield, Geochim. Cosmichim. Acta 63 (1999) 1549–1557.
30. J. D. Donnay, D. Harker, Am. Mineral. 22 (1937) 446–451.

31. M. Adachi, Y. Murata, J. Takao, J. Jiu, M. Sakamoto, F. Wang, J. Am. Chem. Soc. 126 (2004) 14943–14949.
32. M.M. Nobrega, J.B. Olivato, C.M.O. M?ller, F. Yomashita, Polimeros 22 (2012) 475–480.
33. R.E. Tanner, Y. Liang, E.I. Altman, Surf. Sci. 506 (2002) 251.
34. Y. Terada, Y. Suzuki, S. Tohno, Mater. Res. Bull. 47 (2012) 889–895.
35. D. Cahen, G. Hodes, M. Grätzel, J.F. Guillemoles, I. Riess, J. Phys. Chem. B 104 (2000) 2053–2059.
36. S. Hore, P. Nitz, C. Vetter, C. Prahl, M. Niggemann, R. Kern, Chem. Commun. (2005) 2011–2013.
37. H.-J. Koo, J. Park, B. Yoo, K. Yoo, K. Kim, N.-G. Park, Inorg. Chim. Acta 361 (2008) 677–683.
38. J. Krüger, R. Plass, M. Grätzel, P. J. Cameron, L. M. Peter, J. Phys. Chem. B 107 (2003) 7536–7539.
39. A. B. F. Martinson, J. E. McGarrah, M. O. K. Parpia, J. T. Hupp, Chem. Commun. 8 (2006) 4655–4659.
40. C. Wu, L. Qi, Y. Chen, Q. Ouyang, C. Li, Res. Chem. Intermed. 42 (2016) 5653–5664.
41. Y. Duan, N. Fu, Y. Fang, X. Li, Q. Liu, X. Zhou, Y. Lin, Electrochim. Acta 113 (2013) 109–116.
42. Y. Liu, J. Zhang, W. Sun, S. Gao, J. K. Shang, Chem. Eng. J. 249 (2014) 63–71.

Conclusion

In this study, we reported spherical- and bowl-shaped TiO_2 clusters as light scattering centers. A series of characterizations unambiguously confirmed that all materials possessed a high degree of crystallinity, mesoporous structure, spherical- and bowl-shape, wormhole-like pore structure, and excellent light scattering ability. We also proposed reasonable model for the mechanisms of formation of spherical- and bowl-like clusters. A direct triblock-copolymer templating approach is demonstrated for the successful synthesis of size-controlled spherical mesoporous TiO_2. The triblock copolymer is the determining factor in the morphology and the size of the resulting materials. The spherical mesoporous TiO_2/ZnPc hybrids have potential to be used in visible light-active photocatalysis and light scattering centers. Submicron- and micron-sized mesorporous TiO_2/ZnPc hybrids exhibited high photocatalytic activity due to a cascade Mie light scattering. In particular, P123-TiO_2/ZnPc hybrid, which size is comparable with the wavelength of incident light, strongly generated the Mie scattering, followed by a considerable enhancement of the photocatalytic activity. We fabricated TiO_2 electrodes based on mesoporous TiO_2 spheres for dye-sensitized solar cells, which have superior dye-loading capacity. The mesoporous TiO_2 spheres act as scattering centers that improved light scattering without damaging the dye-loading capacity of the internal

surface area. In addition, we synthesized rod-shaped LA@TiO_2 complexes. These materials were tuned from spherical TiO_2 clusters to bowl-shaped TiO_2 clusters by electrospraying using solvents with different vapor pressures. DSSCs containing with the clusters exhibited high energy conversion efficiency because of their high dye loading capacity and light scattering ability. The unique bowl-shaped morphology facilitated multiple light scattering, which considerably enhanced solar cell performance. The spherical- and bowl-shape TiO_2 cluster developed here represents a new design approach for high-performance solar cells and photocatalysis using light scattering and has tremendous potential for practical use in applications ranging from photocatalysis to hydrogen generation.

Korean Abstract

빛은 다양한 방향으로 산란되고 진행 방향이 바뀔 수 있다. 특히, 입자의 크기가 조사된 빛의 파장과 비슷할 때, 미 (Mie) 산란이 발생한다. 대기에서, 구름은 미 산란 효과에 의해 흰색을 띄게 되는데, 이것은 다양한 크기의 미립자들에 의해 모든 파장 영역의 가시광이 산란되기 때문이다. 만약 구형의 이산화티탄에 미 산란 현상을 도입하면, 조사된 빛이 파장과 비슷한 크기를 갖는 구형의 이산화티탄에 부딪혀 전방으로 강하게 산란이 된다. 그러므로, 이웃한 구체들에 의해 조사된 빛의 이동거리가 증가하게 되고, 이에 따라 구체들에 의해 빛의 활용도가 증가하게 된다.

이러한 광산란체에 대한 배경과 기술적, 과학적 가치에 의거하여, 특정한 특성을 갖는 광산란체로서 이산화티탄 입자체를 제조하는 것이 필요하고 기술적으로도 중요하다. 본 연구에서는, 구형과 보울형의 미세다공성 이산화티탄 광산란체를 제조하고, 이를 태양전지와 광촉매 분야에 응용하였다.

크기가 제어된 구형의 미세다공성 이산화티탄 입자체를 티타늄 전구체와 다양한 양친성 삼중 블록 공중합체를 지지체로 사용하여 성공적으로 제조하였다. 삼중 블록 공중합체는 구조 제어와 기공 형성 유도 물질로 사용되었고, 티타늄 전구체와 삼중 블록 공중합체가 용매 내에서 자기조립하여 이산화티탄 나노입자가 웜홀(wormhole) 구조의 기공을 갖는 구형의 응집체가 조립되었다. 삼중 블록 공중합체 마이셀 (micelle)은

중심부의 PO 사슬과 주변의 EO 사슬로 구성된다. 마이셀 중심부는 물의 침투가 어려운 반면, 주변부는 수화되어 있을 것으로 여겨진다. 열역학적 조건 하에서 삼중 블록 공중합체의 응집 거동은 이사화티탄 응집체의 크기와 형태에 영향을 주게 된다.

이러한 크기 제어 합성법에 기반하여, 다양한 크기를 갖는 (245－1188 nm) 아나타제 상의 이산화티탄/아연-프탈로시아닌 (ZnPc) 복합체를 제조하고, 이들의 광촉매 특성과 미 산란 능력을 분석하였다. ZnPc 분자들은 이산화티탄 표면에 응집되지 않고 잘 분산되어 도입이 되었다. 다양한 크기 (직경 245, 548, 798, 1188 nm)를 갖는 구형의 TiO_2/ZnPc 복합체들은 모두 높은 비표면적 (최고 223.76 m^2/g)을 가지며, 미세다공성 구조를 가지고 있음을 확인하였다. 미세다공성 TiO_2/ZnPc 복합체는 가시광 조사 하에서 메틸렌 블루 분해 실험을 통해 우수한 광촉매 효율 (90분 후 최고 89.93%)을 보였고, 이것은 나노입자로 구성된 P25/ZnPc 복합체에 비해 약 2배 높은 분해 성능이었다. 다양한 크기의 미세다공성 TiO_2/ZnPc 복합체들 중에서, 548 nm 크기의 복합체 (P123-TiO_2/ZnPc)가 가장 높은 광촉매 성능을 나타내었다. 이것은 P123-TiO_2/ZnPc 복합체에서 가장 효과적으로 연속적인 미 산란이 발생하였기 때문이라고 할 수 있다.

다음으로, 구형의 미세다공성 이산화티탄이 광산란체로, 그리고 이산화티탄 나노입자가 바인더로 사용되어 구성된 광전극을 제조하고, 이 전극을 이용하여 염료감응형 태양전지의 에너지 변환 효율을 평가하였다. 구형의

이산화티탄과 나노입자로 구성된 전극은 이산화티탄 구체에 의한 광산란과 높은 염료 흡착능 때문에, 태양전지의 성능을 향상시킬 수 있었다. 복합체 형태로 구성된 광전극의 에너지 변환 효율은 7.66%로 이는 나노입자로 구성된 전극의 효율 (4.50%)에 비해 크게 향상되었다.

마지막으로, 전기분무 기술을 사용하여 구형과 보울형의 이산화티탄 나노로드 (nanorod) 응집체를 제조하고, 응집체의 광산란능과 광전특성을 분석하였다. 약 3 nm의 직경과 25 nm의 길이를 갖는 나노로드는 다양한 증기압을 갖는 용매에 의해 다른 응집 형태로 형성되었다. 응집체는 최고 113.57 m^2/g의 높은 비표면적과 미세다공성 구조를 보였다. 응집체가 광산란층으로 도입된 염료감응형 태양전지는 높은 성능을 보였다. 그 중 보울형태의 이산화티탄 응집체가 도입된 소자는 9.13%의 가장 높은 에너지 변환 효율을 나타내었다. 이런 높은 성능은 우수한 염료 흡착능과 보울형태의 응집체의 다중 광산란능에 의해 기인되었다고 할 수 있다.

주요어: 광산란체, 이산화티탄, 삼중 블록 공중합체, 졸-겔 화학, 미세다공, 전기분무, 구형, 보울형, 염료감응형 태양전지, 광촉매, 가시광, 광산란층, 미 산란

학번: 2008-30177

List of papers, patents and symposiums

PAPERS

1. Hyun-Joong Kim, Jae-Deok Jeon, Dong Young Kim and Seung-Yeop Kwak, Improved Performance of Dye-Sensitized Solar Cells with Compact TiO_2 Blocking Layer Prepared Using Low-Temperature Reactive ICP-Assisted DC Magnetron Sputtering, Journal of Industrial and Engineering Chemistry 18 (2012) 1807–1812.

2. Hyun-Joong Kim, Jae-Deok Jeon and Seung-Yeop Kwak, Highly Deispersed Mesoporous TiO_2 Spheres via Acid Treatment and Its Application for Dye-Sensitized Solar Cells, Powder Technology 243 (2013) 130–138.

3. Hyun-Joong Kim, Jae-Deok Jeon, Jae Woo Chung and Seung-Yeop Kwak, A New Architecture of Bowl-Type Mesoporous TiO_2 via Facile Electrospray Method, Microporous and Mesoporous Materials 198 (2014) 170–174.

4. Hyun-Joong Kim, Jae-Deok Jeon, Jae Woo Chung and Seung-Yeop Kwak, Amplified Visible Light Photocatalytic Activity of Mesoporous TiO_2/ZnPc Hybrid by Cascade Mie Light Scattering, Microporous and Mesoporous Materials 227 (2016) 169–175.

5. Hyun-Joong Kim, Jae Woo Chung and Seung-Yeop Kwak, Highly Efficient Dye-Sensitized Solar Cells Containing Bowl-Shaped Titania Nanorod Clusters with Multiple Light Scattering Ability, Powder Technology, under review.

PATENTS

1. 곽승엽, 김현중, 김동석, 염료감응형 태양전지용 복층구조 이산화티탄 전극 및 그 제조방법과 이를 사용하여 제조된 염료 감응형 태양전지, 대한민국 특허등록번호 10-0937799 (2010. 1. 12)
2. 곽승엽, 김현중, 광산란 효율이 높은 미다공성 산화티타늄 입자체 및 이를 제조하는 방법, 대한민국 특허등록번호 10-1662647 (2016. 9. 28)
3. 곽승엽, 김현중, 광산란 효율이 높은 미세 다공성 산화티타늄 입자체를 포함하는 염료감응형 태양전지, 대한민국 특허등록번호 10-1728501 (2017. 4. 13)

SYMPOSIUMS

1. 춘계 재료학회 (2008), 다층구조형 TiO_2 전극 염료감응 태양전지의 제조 및 특성 분석.
2. International Conference on Intelligent Textiles (2008), Preparation and Characterization of Hydrothermally Treated Mesoporous TiO_2 Layer with TiO_2 Blocking Layer for Dye-Sensitized Solar Cells (DSSCs).
3. 춘계 고분자학회 (2009), Preparation and Characterization of Dye-Sensitized Solar Cells with Spherical Mesoporous TiO_2 as a Scattering Layer.
4. International Symposium on the Photochemistry and Photophysics of Coordination Compounds (2009), The Effect of Double Layered Electrode Composed of Compact and Mesoporous TiO_2 Layers on the Performance of Dye-Sensitized Solar Cells (DSSCs).
5. 추계 고분자학회 (2009), Photovoltaic Performance of Dye-Sensitization Solar Cells with Spherical Mesoporous TiO_2 as a Scattering Layer.
6. 춘계 고분자학회 (2010), Development of Dye-Sensitization Solar Cells with Various Sized Spherical Mesoporous TiO_2 as a Scattering Layer.
7. International Conference on Biology, Environmental and Chemistry 2010 (2010), Photovoltaic Performance of a Novel TiO_2 Electrode Consisting of a Mesoporous TiO_2 Layer and a Compact TiO_2 Blocking Layer for Dye-Sensitized Solar Cells.

8. 춘계 고분자학회 (2011), The Effect of Modified Electrode with Reactive Sputtered TiO_2 Blocking Layer on the Performance of Dye-Sensitized Solar Cells.

9. 춘계 고분자학회 (2012), Novel Scattering Layer Using Highly Dispersed TiO_2 Aggregates for Dye-Sensitized Solar Cells.

10. 추계 재료학회 (2016), Zinc Phthalocyanine Embedded with Mesoporous TiO_2 as Efficient Visible Light Active Photocatalysts.